DD

STOCKHOLM UNIVERSITY

DEPARTMENT OF PHYSICS

ELECTRONICS EVALUATION, JET RECONSTRUCTION AND A STUDY OF GMSB IN ATLAS

JÖRGEN SJÖLIN

USIP Report 2000-03

August 2000

Electronics Evaluation, Jet Reconstruction and a Study of GMSB in ATLAS

Jörgen Sjölin

June, 2000

Akademisk avhandling
för avläggande av
teknologie licentiatexamen
vid Stockholms Universitet.

Electronics Evaluation, Jet Reconstruction and a Study of GMSB in ATLAS

Jörgen Sjölin

Akademisk avhandling för avläggande av
teknologie licentiatexamen vid Fysikum, Stockholm universitet.
Försvaras den 14 Juni 2000, kl 11.00,
Rum 4809, Vanadisvägen 9, Stockholm.

Abstract

The ATLAS detector is described. Emphasis is put on the Tile calorimeter and its fast readout electronics. An overview of the charge calibration of the electronics tested during the test-beam periods in 1996-98 is given. The evaluation guided a decision concerning methods of signal compression and dynamical range of the Analog to Digital Converter for the final version. An introduction to the topic of jet reconstruction in the ATLAS barrel calorimeter is given. Also included is a study of the sensitivity to model parameters for Gauge Mediated Supersymmetry Breaking with $\tilde{\tau}_1$ as the NLSP using fast simulations of the ATLAS detector.

Thesis description

This thesis reflects part of the work that I have been involved in within the ATLAS detector community during the past three years. During 1997 and 1998 the activity was focused on the test-beam for the Tile calorimeter. Our Stockholm group provided the fast readout and had the responsibility for the charge calibration. The R&D was very intense and different configurations were tested and evaluated each year. One aspect of this is discussed in Publication I. During the end of 1998 and the beginning of 1999 I provided an update of the performance of the jet reconstruction in the barrel calorimeter. This work is detailed in Publication II and also included in the jet chapter of the ATLAS Detector and Physics Performance Technical Design Report[1]. During the end of 1999 a Monte Carlo study of the sensitivity to GMSB model parameters in ATLAS was done at Lawrence Berkeley National Laboratories. This work is described in Publication III.

Publications

Publication I

Sven-Olof Holmgren and J. Sjölin
Studies of internal resolution for 12 bit and 10 bit ADCs in the Tilecal readout electronics.
ATL-TILECAL-98-135

Publication II

J. Sjölin
Jet reconstruction in the ATLAS barrel calorimeter.
ATL-TILECAL-2000-009

Publication III

J. Sjölin
A study of Gauge Mediated Supersymmetry Breaking with $\tilde{\tau}_1$ as the NLSP in the ATLAS detector.
ATLAS note in preparation

Contents

1

Theoretical motivation

1.1 Why probing energies beyond the EW scale?

Since its appearance during the 1970s, the effective renormalizable gauge theory known as the Standard Model (SM) [2] in particle physics has been overwhelmingly successful in predicting all high energy processes within the experimental error. This predictive power has become even more impressive as the LEP2 era is coming to an end with its 200+ GeV in e^+e^- center-of-mass energy and a recorded total integrated luminosity of 500 pb^{-1} [3, 4].

The basic building blocks of the SM are the left-handed fermionic weak isospin doublets

$$\begin{pmatrix} u \\ d \end{pmatrix}_L, \begin{pmatrix} c \\ s \end{pmatrix}_L, \begin{pmatrix} t \\ b \end{pmatrix}_L, \begin{pmatrix} \nu_e \\ e^- \end{pmatrix}_L, \begin{pmatrix} \nu_\mu \\ \mu^- \end{pmatrix}_L, \begin{pmatrix} \nu_\tau \\ \tau^- \end{pmatrix}_L$$

There is also a right-handed weak isospin singlet for each fermion except for the neutrinos. The gauge interactions among the fermions are determined by the symmetry $SU(3)_c \otimes SU(2)_L \otimes U(1)_Y$. In order to generate mass, the $SU(2)_L \otimes U(1)_Y$ group is spontaneously broken by a scalar doublet into $U(1)_{em}$. This is the famous Higgs mechanism. Counting the SM free parameters: fermion couplings(9), gauge couplings(3), the CKM matrix(4), the QCD phase θ associated with the strong CP problem(1), the vacuum expectation value(1) and the Higgs coupling(1), one finds 19 free parameters in the model.

Since the SM has been so successful, a valid question is to ask why there is any need or motivation at all to continue to challenge it by building yet larger and larger colliders. The costs and amount of manpower required are enormous. Probably the main motivation is that not all parameters in the SM are known. The self coupling of the scalar Higgs-field added to the model to keep it gauge invariant is undetermined. Hence, finding Higgs and determine its mass would make the SM a more complete theory. However, looking at the divergence of the solution to the renormalisation group equation (RGE) for the Higgs self coupling, it is clear that something new must happen at higher energies. What exactly higher energies means depends on the value of the lightest Higgs mass, and if the SM is the whole story.

1.1.1 A low mass Higgs

If the SM Higgs mass is in the range of 130-190 GeV [5], the self coupling divergence will happen beyond the Planck scale and would be purely academic. There is a triviality upper bound due to the RGE, and a lower bound due to the stability of vacuum. One can in this case imagine a desert scenario of no new physics up the Planck scale. There is however a very interesting experimental fact concerning the unification of the gauge couplings [6]. By using the measured gauge couplings and running them according to their SM RGE, they fail to unify at any scale. If on the other hand the Minimal Supersymmetric extension of the Standard Model (MSSM) [7] is assumed, unification happens at the proton decay valid Grand Unification Theory (GUT) scale 10^{16} GeV. Unification is expected from a more complete theory that contains the SM symmetries as a sub group. The unification properties together with an equal predictive power [8] makes the MSSM to a hot potential successor to the SM. Another very practical property of MSSM is that it can be ruled out if the Higgs mass is larger than 130 GeV [9].

1.1.2 The MSSM and SUSY breaking

The presence of quadratic divergences in the SM one-loop corrections introduces a fine tuning or hierarchy problem. In order for the model to be stable the loop correction should be logarithmic. The only known consistent way to achieve this is to impose a symmetry that has intrigued physicists for almost 30 years by now: supersymmetry. Supersymmetry was first shown in four dimensions by Golfand and Likhtman in 1970 [10]. Likhtman seems to be the first one to notice [11] that supersymmetric models are free of quadratic divergences.

On a more fundamental level supersymmetry has the remarkable property to be the only external symmetry that can extend the Lorentz group. This has been proven rigorously [12]. One can really wonder why nature would reject such an opportunity.

In MSSM the SM is extended to include the basic features of a so called $N = 1$ supersymmetry* together with the ideas of GUT. Supersymmetry requires that every bosonic degree of freedom has a fermionic counterpart, thus the field content of the model has to be doubled. A practical way to organize things turns out to be in terms of chiral supermultiplets, e.g. $((\tilde{u}_L\ \tilde{d}_L)(u_L\ d_L))$. Note that the Higgs sector for several reasons is required to have two chiral supermultiplets, $((H_u^+\ H_u^0)(\tilde{H}_u^+\ \tilde{H}_u^0))$, and $((H_d^0\ H_d^-)(\tilde{H}_d^0\ \tilde{H}_d^-))$. There are of course also three gauge supermultiplets. A general SUSY Lagrangian unfortunately contains unacceptable terms that violates baryon and lepton conservation. To make the model experimentally acceptable a symmetry called R-parity is imposed. Standard particles have R-parity +1, and the supersymmetric partners have -1. Thus the lightest SUSY particle (LSP) is stable, and the SUSY particles must be produced in pairs. There is however no direct reason to expect R-parity to be conserved. It is possible to construct stable proton SUSY models with R-parity violating terms in the Lagrangian. Therefore it is highly relevant to put limits on the R-parity violating couplings. If R-parity is violated the LSP will decay and the experimental SUSY signatures will change drastically.

There is one very important piece missing in order to make the low energy supersymmetric hypothesis consistent. The conserved charges that follow from the supersymmetry, which also are the generators of the supersymmetry transformations, commute with the momentum operator. This implies that the supersymmetric partners must have the same mass if the supersymmetry is exact. Not a very promising model prediction at first sight since not a single SUSY particle has been found yet. The key to construct a phenomenologically viable supersymmetric Lagrangian is to break the supersymmetry in such a way

*N is the number of supersymmetries. $N = 1$ is the only case that is relevant at low energies.

that the loop divergences remain logarithmic. This is called soft SUSY breaking (SSB) and simply consists of a limited set of allowed terms that are added to the SUSY Lagrangian.

Now when all the ingredients of a useful SUSY model are in place, what are the predictions? The first thing one can do is to count the number of free parameters. They turn out to be 124, a ridiculous number! Most of this enormous freedom comes from the SSB. The number of parameters can be reduced taking into account experimental constraints on flavor changing neutral currents (FCNC), which imply flavor blind mass matrices and CP violation that requires absence of extra complex phases. This is called constrained MSSM and it has a predictive power at least as good as the SM [8].

1.1.3 SUGRA and GMSB

The most important topic in SUSY is actually the origin of the SSB, both theoretically and experimentally. To spontaneously trigger SSB within MSSM itself turns out to be very difficult. A successful approach is instead to assume that the SSB origin is communicated from a hidden sector into MSSM by flavor blind interactions. Gravity is just such a flavor blind interaction that appears naturally once SUSY is required to be a local symmetry [13]. The scenario with gravity mediated SSB is called SUGRA. Assuming that SSB takes place at $\sqrt{F} \sim 10^{11}$ GeV one finds by dimensional analysis the mass scale for soft SUSY beaking (m_{soft}) to be of the order

$$m_{soft} \sim \frac{F}{M_P} \sim 100 \text{ GeV}.$$

SUGRA is a very beautiful effective theory where all the non renormalizable soft terms can be described with only five parameters: $m_{1/2}, m_0^2, A_0, \tan\beta, \text{sgn}\mu$. The first three are fermionic and scalar masses and a trilinear coupling. The last two stem from the requirement of EW-symmetry breaking, $\tan\beta$ is the ratio of the vacuum expectation value of the two Higgs-fields, and μ is the Higgs coupling originating from the superpotential. Consequently the complete particle spectrum is predicted and the lightest neutral† supersymmetric particle (LSP) turns out to be a neutralino (χ_1^0), a mixture of $\tilde{B}$, $\tilde{W}^0$, $\tilde{H}_u^0$, and $\tilde{H}_d^0$.

In minimal SUGRA universal masses and couplings are imposed at the GUT scale to assure GUT and small FCNC. These assumptions are very strong. Another way to suppress FCNC is to assume that pure gauge interactions communicate the SSB. A layer with messengers at the mass scale M_m is put in between MSSM and the true and somewhat unspecified source of SSB. Now the boundary conditions are closer in energy to the SM and the gauge fields automatically suppress FCNC. This scenario is referred to as gauge mediated SSB (GMSB)[14]. Now we have for e.g. $M_m \sim \sqrt{F_m} \sim 10^5$ GeV

$$m_{soft} \sim \frac{\alpha_i}{4\pi}\frac{F_m}{M_m} \sim 100 \text{ GeV},$$

where the α_i's are the usual gauge couplings. Realistic GMSB is quite complicated and a practical model was first proposed by Dine et al[15] inspired by a suggestion from Ed Witten. The messengers are chiral superfields in a representation of $SU(5)$ in the minimal case. Different field configurations can be parameterized by a parameter called N_5. Depending on M_m the maximum of N_5 ranges from 5 to 10 in order to preserve perturbativity[16].

†Since it is stable due to R-parity it must for cosmological reasons be neutral.

GMSB can be made very predictive and the minimal model is fixed by only six parameters: $M_m, F_m, F, N_5, \tan\beta, \text{sgn}\mu$. F is the fundamental SSB scale while F_m is what the messengers see. F determines the gravitino ($\tilde{G}$) mass

$$m_{3/2} \sim \frac{F}{M_P} < 1 \text{ keV}$$

and hence $\tilde{G}$ is the LSP in GMSB models. The phenomenology is mainly determined by the next lightest sparticle (NLSP).

If neither gravity nor gauge fields dominates SSB, it can be generated by anomalies that usually are suppressed in the other scenarios. Realistic models with small FCNC have quite recently been proposed [17]. These are called anomaly mediated SSB (AMSB).

2

Experimental overview

2.1 The LHC

To really challenge the SM and reach physics at energies 10 times higher than the current limits, a new 14 TeV center-of-mass energy proton-proton collider is being built at CERN (European Organization for Nuclear Research) in Geneva. It will be ready for operation in 2005. Today our current state-of-the-art knowledge comes from LEP, the 200+ GeV electron-positron collider which will be replaced by the Large Hadron Collider (LHC), and the Tevatron, the 1.8 TeV proton-antiproton collider at FermiLab. With LHC particles with masses in the TeV range can be produced. Hence LHC will be able to either falsify or confirm supersymmetry or the existence of any SM model Higgs particle. LHC will also be able to accelerate heavy ions instead of protons to study quark-gluon transitions at high energy densities.

LHC will replace LEP and use the same 27 km long tunnel, see Figure 2.1. The 7 TeV

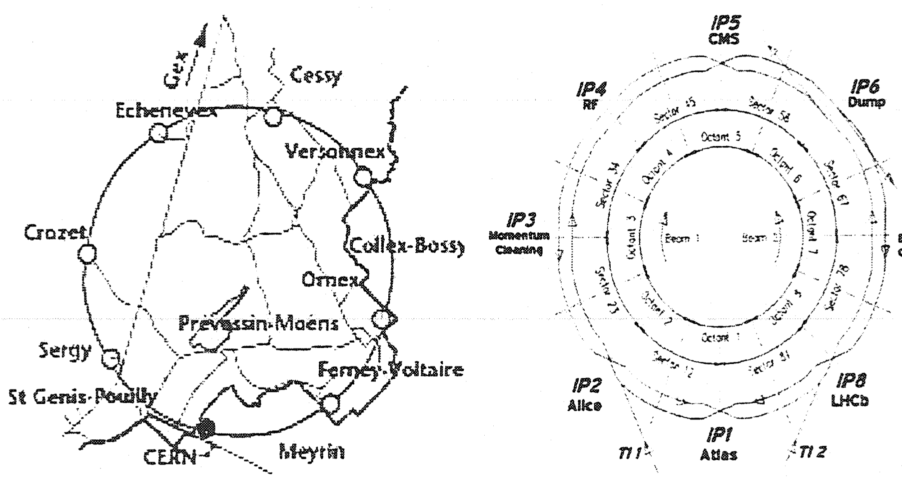

Figure 2.1: The geographical location of the LHC tunnel (left), the different experiments are also shown (right).

beam and the fixed radius define a peak magnetic dipole field of 8.3 T. A lot of technical development was required to enable the superconducting magnets needed for this large field to operate reliably at 1.9K. The amount of material that has to be cooled is 31,000 tons. The inner diameter of the magnet is 56 mm, and the two beams are separated by 194 mm. After filling, the protons are accelerated from 450 GeV to 7 TeV and the luminosity $\mathcal{L} = 10^{34}$ cm^{2}s^{-1} is maintained for 10 hours before a new filling is needed.

In order to study the particles created in the collisions, detectors will be placed around the four interaction points. Under construction are two general purpose detectors ATLAS and CMS, one heavy ion detector ALICE and one detector for B-physics LHC-B, see Figure 2.1.

For the first three years LHC is expected to run at low luminosity $\mathcal{L} = 10^{33}$ cm^{2}s^{-1}, accumulating 10 fb^{-1} per year per experiment, then continue to run at full luminosity $\mathcal{L} = 10^{34}$ cm^{2}s^{-1}, accumulating 100 fb^{-1} per year per experiment.

2.2 The ATLAS detector

ATLAS [24] is one of two general purpose detectors utilizing the LHC. It is designed to cover as much as possible of the physics that can be generated in the 14 TeV proton-proton collisions, see Figure 2.2. Most of the particle detectors in colliding experiments

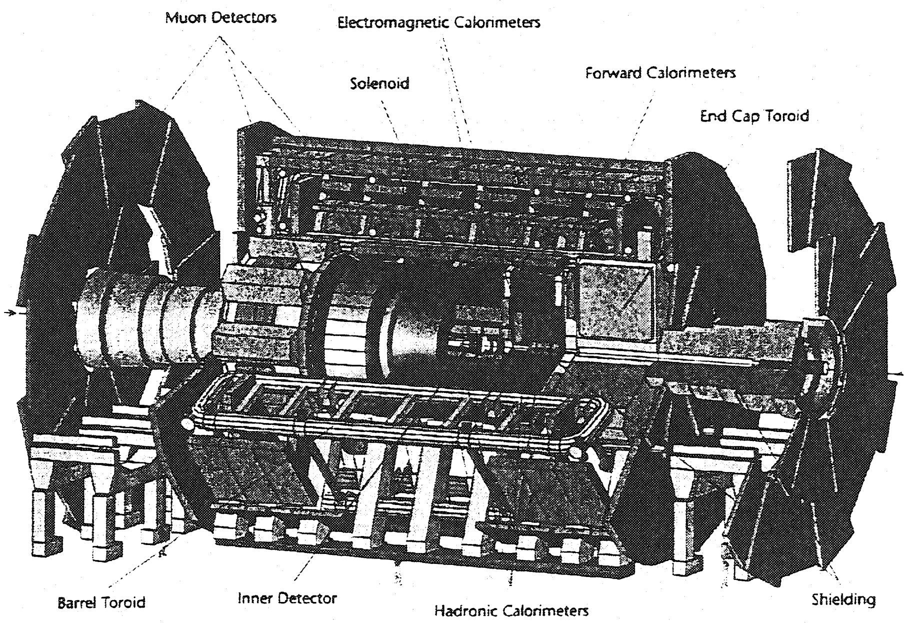

Figure 2.2: Overview of the ATLAS detector.

have the same overall cylindrical configuration. Starting from the interaction point there are the following detectors: a tracker to reconstruct charged tracks in a magnetic field, an electromagnetic calorimeter, a hadron calorimeter and a muon spectrometer. The general design is aiming for:

- Good solid angle coverage. This is measured in the boost invariant parameters $|\eta| < 4.9$ and $\phi \simeq [0, 2\pi]$. The pseudorapidity, η, is defined as $-\ln \tan \theta/2$, where θ is the polar angle from the beam axis, and ϕ is the azimuthal angle. A hermetic coverage is needed among other things for good missing energy resolution, which is heavily used e.g. in SUSY searches.

- Excellent electromagnetic calorimetry for electron/photon separation and accurate electron, photon and jet measurements to very high energies. Accurate jet measurements also require a thick and hermetic hadron calorimeter to avoid false missing energy.

- Powerful tracker that in a robust way can handle high track multiplicities, resolve charged particles with high transverse momentum (p_T) and tag τ and heavy flavor quarks.

- High energy resolution of muons at high rates. This is solved by a large independent external muon system.
- Fast and sensitive trigger to enable effective filtering of interesting physics in a tremendous background of 23 interactions per bunch crossing at a rate of 40 MHz.

2.2.1 The inner detector

The inner detector tracker of ATLAS covers $|\eta| < 2.5$. It is 7 m long and 1.2 m in radius. A 2 T magnetic field enables the momentum measurements. The tracker uses three different techniques to minimize the material and cost and to maximize the performance. Close to the interaction point are silicon pixels with a resolution of $\sigma_{\phi r} = 12\mu$m. There are 140 million readout channels in total. Outside the pixels are the silicon strips with a resolution of $\sigma_{\phi r} = 16\mu$m. The strips have 6 million channels and the astonishing area of 61 m^2 of silicon. The outer volume is covered with straw tubes providing drift time information combined with transition radiation to identify electrons. The resolution is $\sigma_{\phi r} = 170\mu$m.

The tracker performance can be approximated [1] (in units of TeV^{-1} and mrad) by the parameterizations

$$\sigma(\frac{1}{p_T}) = 0.36 \oplus \frac{13}{p_T\sqrt{\sin\theta}}$$

$$\sigma(\phi) = 0.075 \oplus \frac{1.8}{p_T\sqrt{\sin\theta}}$$

2.2.2 Calorimetry

The calorimetry plays a central role in hadron colliders since it gives access to the rich physics of jets. The technique is robust, fast and has the nice property that the resolution in principle scales like $1/\sqrt{E}$. ATLAS has adopted the sampling calorimetry concept in different configurations, see Figure 2.3.

The electromagnetic (EM) calorimeter is LAr/Pb in an accordion structure to avoid cracks in azimuth and to enable efficient readout with small time constants. The requirements for the EM calorimeters are set extremely high. e.g. a dynamic range of 50 MeV to 3 TeV, linearity better then 0.5%, energy resolution better than $1\% \oplus 10\%/\sqrt{E(GeV)}$, high granularity of the order $\Delta\phi \times \Delta\eta = 0.03 \times 0.03$ and a good containment given by at least 24 radiation lengths of sampled material. The information is read out by 200,000 channels.

The hadronic calorimetry is LAr/Cu in the endcap region and in part of the forward. The forward region also has LAr/W for better resolution due to higher densities. The barrel and extended barrel regions consist of an Fe/Scintillator calorimeter with radial tiles staggered in depth. The main task for the hadronic calorimeter is to improve the jet resolution, make sure that the energy is contained and to protect the muon system. Ten interaction lengths (λ) of sampled material and 1.5 λ of support fulfill this requirement. The resolution for jets should be better than $3\% \oplus 50\%/\sqrt{E(GeV)}$ for $|\eta| < 3$, and $10\% \oplus 50\%/\sqrt{E(GeV)}$ for $|\eta| < 5$.

2.2.3 The muon system

The large muon spectrometer covers the region $|\eta| < 2.7$ with a trigger capability within $|\eta| < 2.4$. Superconducting air core toroid magnets provide the magnetic field. Monitored

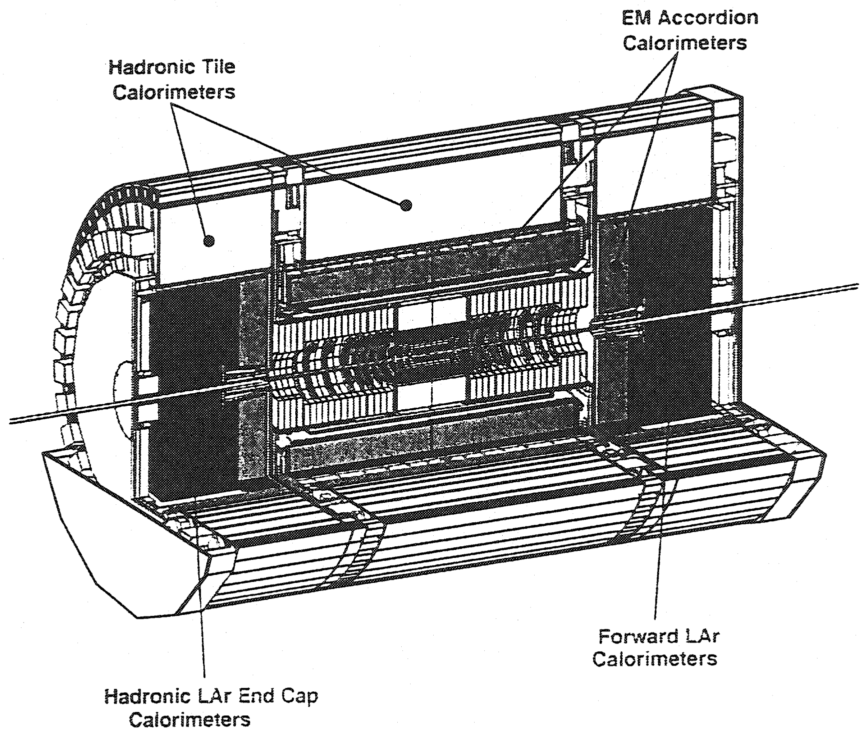

Figure 2.3: Overview of the different sampling calorimeters in ATLAS.

drift tubes provide most of the track measurements. The drift time is 700 ns and the wire resolution is 80 μm. Where the rates are higher cathode strip chambers with a drift time of 30 ns are used. The system is monitored optically for a mechanical accuracy of 30 μm. The trigger consists of resistive plate chambers in the barrel and thin gap chambers in the end-cap. The trigger chambers provide bunch crossing information and a second coordinate orthogonal to the precision measurement.

2.2.4 The trigger

In contrast to the low rate experiments at LEP, one would be blind in the LHC high rate environment without a sophisticated trigger. The bunches will collide at a rate of 40 MHz and generate on average 23 inelastic scatterings each time. The filtering of interesting events that are stored for final analysis is organized in three levels, see Figure 2.4. The first level identifies the bunch crossings and finds regions of interest (RoI) using p_T thresholds in the calorimeters and the muon system. The RoIs contain muons, EM-clusters, hadrons, and jets. Global information on missing transverse energy and scalar transverse energy is also reported. A decision of accept is taken within 2μs and the information is passed on to level 2. Level 2 refines the RoIs selected by level 1 into physical objects that can be selected from a trigger menu. Depending on the luminosity option the thresholds are set as low as possible without saturating the readout chain and to allow different object mixtures during data taking. The final level 3 event filter (EF) decides whether or not the event should be stored. The EF uses offline software and the refinements are of such high quality that many of the rates are almost the same as the true signal.

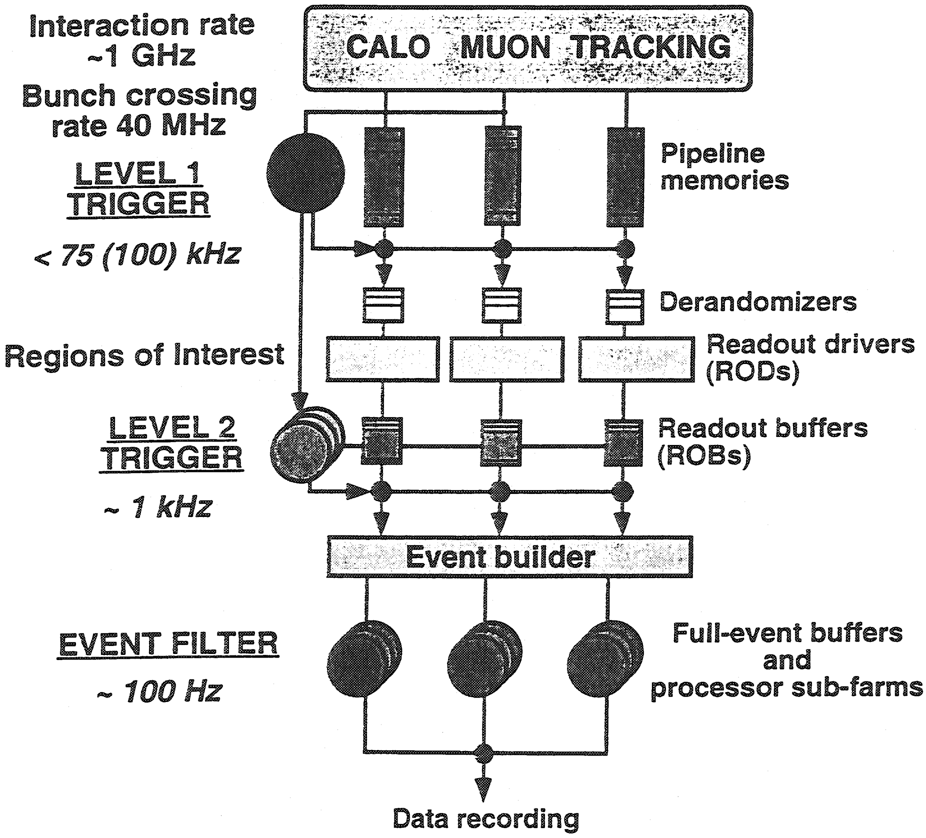

Figure 2.4: Overview of the trigger levels and the associated rates.

3

Introduction to the Tile calorimeter

3.1 Hadronic calorimetry

Electromagnetic cascades are governed by bremsstrahlung and pair production, hence they are characterized by the material constant called the radiation length (X_0), where X_0 is defined as the energy loss due to bremsstrahlung, i.e. $dE/dx = -E/X_0$. For iron X_0 is 1.76 cm. The radial spread is dominated by multiple scattering and contained within approximately $2R_M$, where R_M is the Moliere radius. For iron $R_M = 1.65$ cm. Hadronic cascades on the other hand are characterized by the nuclear interaction length (λ) which for iron is 16.8 cm. The radial spread is caused by nuclear reactions with an average p_T of 350 MeV. Consequently both the longitudinal and radial spread are much larger for hadronic than for electromagnetic cascades and also the fluctuations are larger due to the large variety of different possible processes.

The generic behavior and performance of sampling calorimeters for hadrons has been summarized in great detail by Wigmans [18, 19]. His main conclusion is that for an optimal performance, the response of the calorimeter to hadronic (h) and electromagnetic (e) components of the shower should be the same, i.e. $e/h = 1$. The calorimeter is then said to be compensating. That this is plausible is easily seen from the response in the calorimeter for a charged pion (π)

$$\pi = h(1-f) + ef$$

where f is the electromagnetic fraction which can be parameterized [20] by $f \simeq 0.1 \ln E(GeV)$. After error propagation we have

$$(\sigma_\pi)^2 = (1-f)^2{\sigma_h}^2 + f^2{\sigma_e}^2 + (e-h)^2{\sigma_f}^2$$

and it is clear that the fluctuations in f will not affect the total resolution if e/h=1, assuming that the e/h tuning affects on σ_h and σ_e are small. For charged pions σ_f can be quite large due to the possible production of e.g. neutral pions in the initial interaction.

Any deviation from $e/h = 1$ will result in a resolution scaling that deviates from the $1/\sqrt{E}$ scaling which is expected from the sampling nature. According to Wigmans this deviation can be parameterized as a constant term

$$\frac{\sigma}{E} = \frac{a}{\sqrt{E}} + b.$$

The presence of a constant term will limit the intrinsic performance at high energies. However not only does the resolution deteriorate for $e/h \neq 1$, but the response will also no longer be linear in energy which is obvious from the ratio

$$\frac{e}{\pi} = \frac{e/h}{1 - f(1 - e/h)} \simeq A + B \ln E.$$

For small deviations from $e/h = 1$ one can make a Taylor expansion giving the last expression where A and B are constants. It has been shown [22] that it is possible under very specific conditions, to construct a compensating calorimeter using only passive elements like Pb/Scintillator. Since there exists no simulation tool that in a reliable way can predict the hadronic behavior much of the development is by trial and error. This is very much in contrast with electromagnetic simulation which is very predictive.

3.2 The Tile calorimeter

The Tile calorimeter [25, 26] covers the barrel ($|\eta| < 1.0$) and extended barrel region ($0.8 < |\eta| < 1.7$). The inner radius is 228 cm and the outer radius is 423 cm. The absorbing material consists of steel plates with 4 mm or 5 mm thickness. The sampling material is 3 mm thick polystyrene tiles doped with PTP and POPOP for optimal light yield and wavelength. The scintillator is wrapped in order to enhance the light yield and to provide a mask for uniform response. The light is collected and read out by wavelength shifting (WLS) fibers, one fiber on each side of the tiles. Due to the EM-calorimeter in front, only the hadronic response is optimized. This enables an unorthodox design with the tiles in the longitudinal direction. Good homogeneity is achieved by staggering in depth, and the fiber readout is made much simpler, see Figure 3.1.

The light from the WLS fibers is summed into an optimized segmented cell structure and detected by a photo multiplier tube (PMT), see Figure 3.2 for an example of the cell to PMT mapping in the extended barrel. The cell structure for the barrel module 0 is shown in Figure 3.3. The output from the PMT is a 20 ns FWHM wide current pulse with a rise time of 5 ns. The total charge is proportional to the incoming light. The fast pulse puts strong requirements on the electronic readout. This is discussed in detail in the later sections. There are 64 azimuthal calorimeters containing 45 cells in the barrel and 14 cells in each of the two extended barrels. Each extended barrel also includes 3 PMTs for extra scintillators. There are in total about 10000 channels since there are two PMTs per cell.

One important parameter for the overall performance of the calorimeter is the light yield. The light yield is measured in number of photoelectrons N_{pe}, created in the PMT. According to Poisson statistics the statistical contribution to the resolution due to N_{pe} is expected to be of the order $\sigma/E = 1/\sqrt{N_{pe}}$. There are several ways to estimate N_{pe}. One can e.g. introduce known filters in the light path [21] or study the quantities $\sigma_{LR} = L - R$ and $E_{LR} = L + R$ [22], where L represents the left PMT and R the right PMT. In order not to severely affect the intrinsic resolution N_{pe} should be kept higher than 20 pe/GeV. This was achieved already in the 1993 test-beam of the first prototype with a $N_{pe} = 24$ pe/GeV. Next year it was improved to 48 pe/GeV, and finally the last prototype in 95 excelled with 64 pe/GeV. It is mainly the muons that are sensitive to N_{pe} and above 48 pe/GeV no measurable improvement was found except for an improved safety margin of course. In the 1997 test-beam of the extended module 0 the muon signal in the last compartment was separated from the noise by five standard deviations.

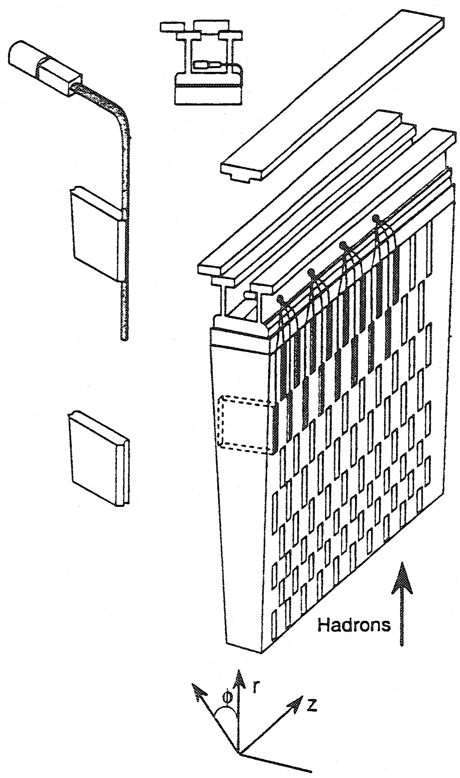

Figure 3.1: Schematic drawing of the Tile calorimeter.

Since the e/h ratio is dependent on the sampling fraction the value will vary for different angles. In the prototypes e/h was measured to 1.23 at a 10 degree angle, and 1.36 at 20 degree angle. For the 1998 test-beam of the barrel module 0 e/h was found to be 1.36 at $\eta = -0.55$ and 1.45 at $\eta = -0.25$. The intrinsic resolution for the Tile calorimeter with respect to charged pions was measured in the 1996 barrel module 0 to be $\sigma/E = 44\%/\sqrt{E(\text{GeV})} + 2.4\%$. One might worry about the linearity but it has been shown in the 1996 test-beam with the combined EM and hadronic calorimeters that a weighting technique can reduce the nonlinearity to less than 2% with improved resolution. The weighting technique used was the so called H1 technique originally used at HERA [23]. The energy dependence of each cell is parameterized and the response for small energies is equalized upwards to the EM scale. The result for the combined setup using the H1 method was $\sigma/E = (42\%/\sqrt{E} + 1.8\%) \oplus 1.8\%/E$. The energy independent contribution to the spread is due to the high noise in the LAr accordion. The results for individual hadrons give confidence that the requirement on the jet resolution can be fulfilled since the individual hadron performance must be better than for jets.

3.3 Detector calibration and monitoring

No instrument is of any use unless it is stable and well calibrated. The Tile calorimeter is no exception. A lot of development has gone into providing fast and reliable methods to monitor the stability and recalibrate the complete detector chain, from an incoming particle

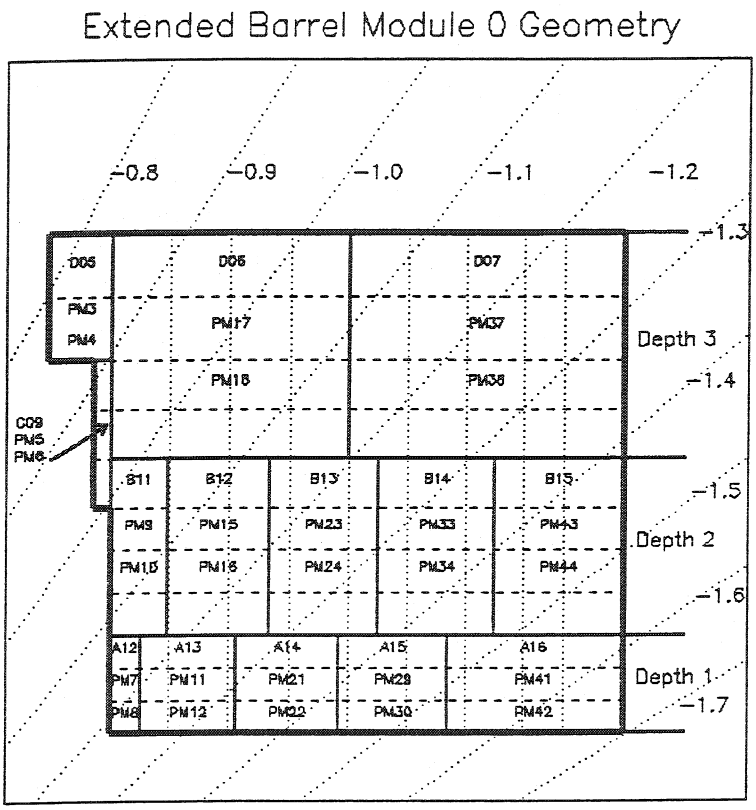

Figure 3.2: Mapping of cells and PMTs in the extended barrel module 0.

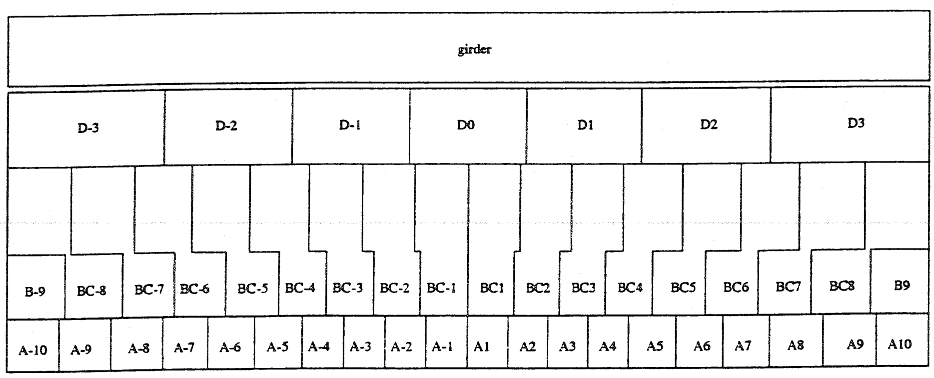

Figure 3.3: Cells in the barrel module 0.

to a digitized value in the analog to digital converter (ADC). These systems are described in the following subsections.

3.3.1 Detector and PMT response via cesium 137

The ^{137}Cs system is capable of monitoring the response from each tile and intercalibrate all PMT channels. It consists of a capsule of approximately 10 mCi ^{137}Cs movable orthogonal through the iron and scintillating tiles, see Figure 3.4. The 30.2 y half life of the source is enough to provide monitoring over long periods of time. The 0.66 MeV γ radiation is

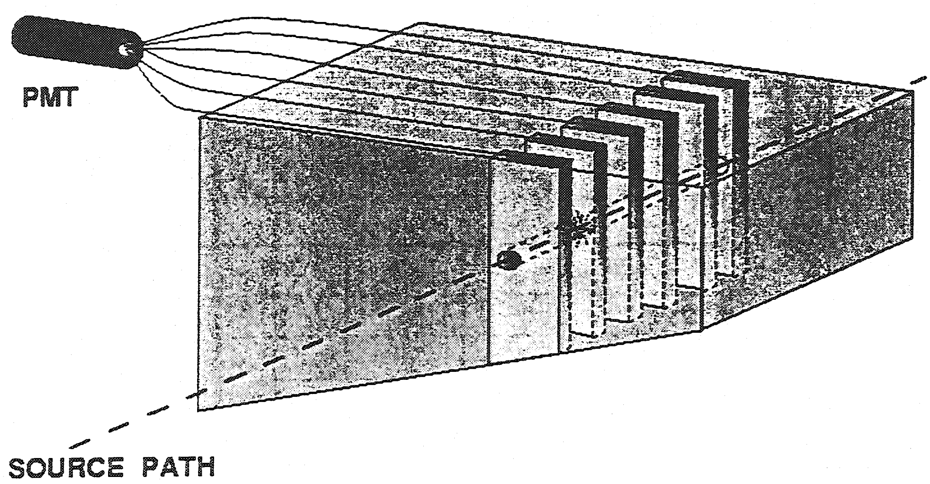

Figure 3.4: Conceptual picture of the Cs source as it moves through the detector during calibration.

also well tuned to resolve each tile. The PMT current is measured by an integrating ADC system, see Figure 3.5. By integrating the response cell to cell the PMT output can be equalized to give an overall intercalibration of the order of 2%. The PMT gain is controlled by adjusting the high voltage.

3.3.2 Laser surveillance of the PMT stability

Each PMT is connected to a pulsed laser via fibers. The pulse width is 15 ns. The laser output is monitored by three photodiods which in turn are calibrated by a ^{241}Am α source. Intensity modulation and filters enable linearity checks over the full dynamic coverage of the PMT readout chain. The laser can do drift checks in matter of seconds and linearity scans in 10 to 15 minutes, e.g. between LHC fills.

3.3.3 Electronics calibration via charge injection

The fast readout that measures the PMT current must have an absolute calibration that is even better than the ^{137}Cs system, that is below 1%. This is achieved by injecting charge(Q) stored in a known precision capacitor(C) at a well defined reference voltage(U), i.e. $Q = CU$. A conceptual diagram of the front-end input stage or "3-in-1 card" used in the final configuration that was tested 1998 is shown in Figure 3.6. The 3-in-1 card is integrated in the PMT block. It includes all the analog fast readout functionality except the ADC, see Figure 3.7. In the 1998 design U is set by a 10 bit DAC and two different C can be selected, either 100 pF or 5.1 pF. Only the 100 pF is reliable for absolute calibration

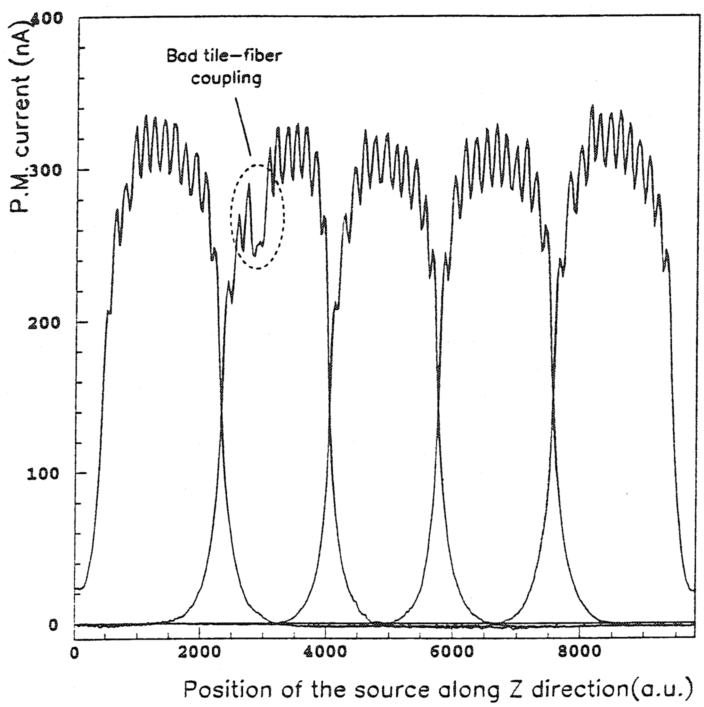

Figure 3.5: The response from the Cs system as the source is moved orthogonal through the iron and scintillating tiles.

since it is less affected by parasitic capacitance, ~ 0.1 pF. During 1998 Q is given by

$$Q = 2 * 4.092 * C * DAC/1023 \quad \text{(pC)} \tag{3.1}$$

The first version of the integrated charge injector used during 1996-1997 had only one capacitor but two 8 bit DACs. In 1996 $CU = 500$ pC, and in 1997 $CU = 640$ pC. The charge Q during 1996-1997 was

$$Q = CU * DAC1 * DAC2/(255 * 255) \quad \text{(pC)} \tag{3.2}$$

Since the sampling rate is 25 ns and the FWHM of the pulse from the shaper is 50 ns there is no guarantee to sample the true peak during calibration. In order to resolve the pulse, a programmable delay is integrated in the 3-in-1 that enables a scan of the pulse by shifting the phase between the sample-and-hold and the charge injection. In most of the analysis the time step is set to $\sim$0.4 ns.

3.4 Fast readout electronics requirements

The lower bounds of constraints for the readout electronics performance are set by the physics requirements [24]. The low electronic noise needed to resolve minimum ionizing particles is incompatible on a fundamental level with the demand for accurate pulse timing and the rejection of the pile-up noise generated by the high bunch crossing rate, hence a delicate trade-off is necessary [27]. This trade-off is implemented in the shaper stage in the

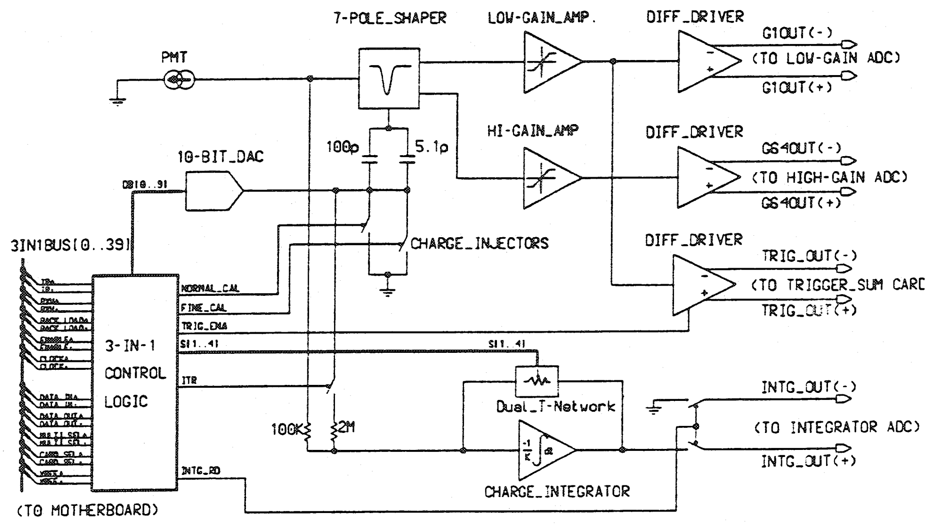

Figure 3.6: Conceptual diagram of the 1998 front-end analog electronics, physically realized in the 3-in-1 card.

very beginning of the readout chain. It is important to keep in mind that it is the output from the shaper that defines the requirements for the back-end of the system. The purpose of the shaper is to interface the fast photo-multiplier tube PMT pulse to the rest of the readout. The overall signal chain can be summarized as follows: the physics processes in the iron is sampled by scintillator tiles, the scintillator light is detected by the PMT generating 20 ns wide current pulses that are fed into the shaper input stage. This translates into a set of Tile specific readout requirements:

- Shaping 20 ns FWHM wide PMT signals into 50 ns FWHM wide and shape invariant pulses. The choice of 50 ns [28] was governed by the studies done for the LAr calorimeter. The more hostile environment in LAr required a pulse width between 47 ns and 80 ns. Due to low electronic noise figures and a completely passive and reactive shaper design the electronic noise is not an issue in Tile, e.g. the channel noise is 27 MeV and the muon deposition in the thinnest layer is 350 MeV. That 50 ns is quite safe from pile-up is clear from the pile-up factor of 1.18; that is, it is just 1.18 times more noisy than a measurement from one single bunch crossing, i.e. no pile-up present.

- A 30 MeV to 2 TeV (0.012 pC to 800 pC per channel) dynamic range equivalent to 16 bit on a linear scale. This is due to the physics requirement to resolve minimum ionizing particles (11 counts), while at the same time the system must not saturate when 2 TeV of energy is deposited in one cell.

- The readout must not affect the intrinsic calorimeter performance whose requirements is set in terms of the jet resolution:

$$\frac{\sigma}{E} = \frac{50\%}{\sqrt{E}} \oplus 3\%$$

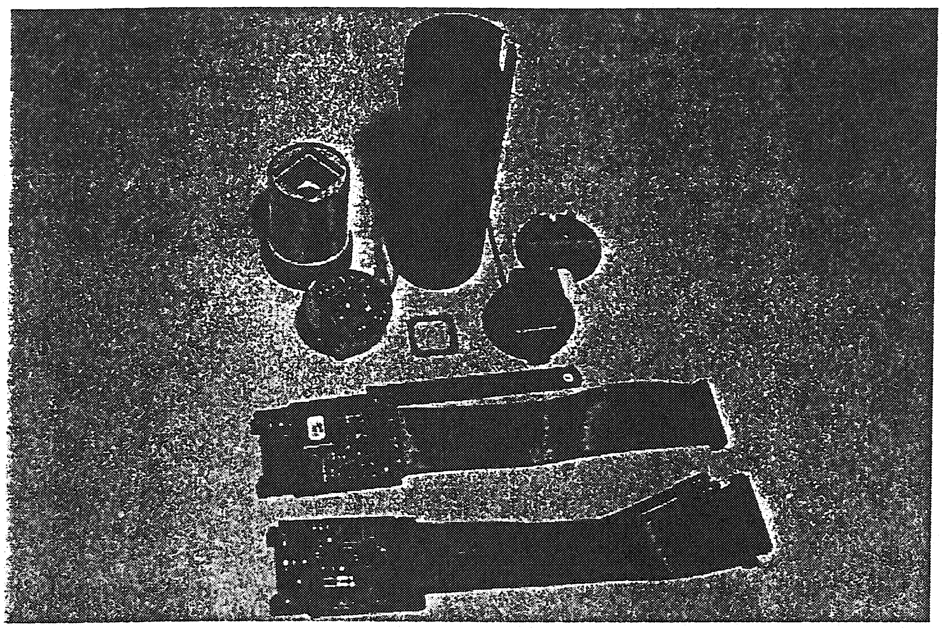

Figure 3.7: Picture of the PMT block with the integrated 3-in-1 card. The two black coaxial analog cables identifies the 3-in-1.

- Dynamic distortions below 1%, in order to make use of robust digital filtering techniques.
- The channel to channel intercalibration spread must not exceed 1%.
- A sampling rate of 40 MHz given by the LHC[24] bunch crossing.
- For each event the complete readout chain must be able to deliver at least 5 signal samples and 2 pedestal samples at a rate of 75 kHz to the level 2 filter without dead time and withstand a radiation dose of 10 to 50 krad. These requirements are not covered in this paper, however the tests for the final digitizer system began already during the end of the 1998 test-beam[34].

3.5 Signal processing of the fast readout

3.5.1 Charge reconstruction

The output from the 3-in-1 card is sampled by an ADC every 25 ns. During ATLAS operation a frame of at least 5 samples of the pulse will be available. A few samples before each frame will also be available to estimate the average bias or "pedestal". One must be aware of the fact that the actual procedure used for reconstruction of the charge from the ADC samples will affect both the absolute calibration and the resolution for real data. What the optimal procedure is depends crucially on the transfer function of the system.

If the analog system is linear in Q and has a bandwidth much larger than the signal in the entire dynamical range, then there exists a well known optimal method to estimate the charge. This method is called the optimal filter and is anticipated to be the method used in ATLAS. Another and more explicit way to state the conditions is to say that the system response $S(t,Q)$ to a charge Q must be shape invariant, i.e. there exists a function $S(t,Q)$ such that $S(t,Q) = Qs(t)$. The function $s(t)$ is the output pulse shape normalized to 1. All contributions to the charge resolution are optimally minimized by the optimal filter, i.e. pile-up noise, electrical noise, quantization noise and time jitter. Especially in test-beam time jitter is a problem since the sample-and-hold is uncorrelated with the trigger. The optimized quantities in the time domain to first order [27] are

$$Q^* = \sum_i a_i S_i, \tag{3.3}$$

$$Q^*\tau^* = \sum_i b_i S_i, \tag{3.4}$$

$$\tag{3.5}$$

where

$$S_i = LUT(ADC_i - P) = Qs(t_i - \tau) + n_i \simeq Qs_i - Q\tau\frac{ds_i}{dt_i} + n_i. \tag{3.6}$$

The constraints are

$$< Q^* >= Q, \tag{3.7}$$

$$< Q^*\tau^* >= Q\tau, \tag{3.8}$$

$$\min_{a_i} \sum_{ij} a_i a_j < n_i n_j >, \tag{3.9}$$

$$\min_{b_i} \sum_{ij} b_i b_j < n_i n_j > . \tag{3.10}$$

ADC_i is the ADC sample at time $t_i - \tau$ and P is the pedestal at the ADC input. The function $LUT()$ normalizes $S(t)$ such that $max_t S(t) = Q$. The function $LUT()$ can also be used to linearize the system response. This is described later in this chapter. The discrete version of the shaper function s_i, is defined in such a way that there exists an i such that $s_i = 1$, i.e. one of the time samples is the peak time sample. Please note that S_i and ADC_i are not required to exist at the same time as s_i, the allowed difference is the phase factor τ which represents the time between the true peak time and time of the maximal sample. The time step in i is in this case 25 ns. The stochastic process n_i models the noise on top of the average pedestal level. The correlation $< n_i n_j >$ can be estimated from pedestal runs, i.e. samples without signal. Note how much the power of the optimal filter is based on the condition that s_i is independent of Q. Hence this is a basic requirement on the fast readout electronics.

3.5.2 Pulse shape reconstruction

The pulse shape s_i is trivially estimated from the measured quantities S_i and the known injected charge Q. During charge injection it is possible to scan t in steps of 0.185 ns and hence i is a very good approximation of continuous time. Consequently $S_i = Qs_i$ and we have

$$\frac{\partial S_i}{\partial Q} = s_i \tag{3.11}$$

However due to imperfections in the injector system there are contributions from leakage in the capacitor switch which can be modeled as $l(t)$ and a compensating constant charge bias b. So if Q' is the charge set in the hardware, the true charge $Q = Q' + b$. We now have

$$S_i = (Q' + b)s_i + l_i = Qs_i + l_i \tag{3.12}$$

but equation (3.11) remains the same.

3.5.3 Readout linearization

Due to the advanced injector system, the intrinsic hardware is not required to be linear. By mapping each ADC count to the correct charge Q it is straightforward to linearize the response. The mapping is called a look-up-table (LUT). However, just as in the optimal filter case, the pulse must be shape invariant or equivalently $\partial s_i/\partial Q = 0$. Otherwise the mapping will not be unique and additional information beyond S_i is needed to lift the degeneracy. The mapping is then simply a modified version of equation (3.12)

$$S_i = LUT(ADC_i - P) = Qs_i + l_i = \{\text{at the pulse peak}\} = Q' - Q_0 \tag{3.13}$$

Q_0 is found by linear extrapolation to $S_i = 0$ assuming the system to be linear at small signals. The linearization can in principle be made at any instant of time as long as there is signal, but if it is not performed at the pulse peak the absolute Q will not be correct. The absolute scale can in that case be calibrated by an extra constant (C) included in the optimal filter, i.e.

$$Q^* = C\sum_i a_i S_i \tag{3.14}$$

Please note that the dominating noise must enter before the non linearities in order to fulfill the optimal filter conditions.

It is possible to map any arbitrary function $Q^* = f(S_1, S_2.., S_n) = Q' - Q_0$ for an arbitrary system as long as they are bijective, but then we have left the idea of linear optimal filtering. That this is not acceptable is probably one of the most important conclusions in this paper as we will see later on in the evaluations of the test-beam results. This is of course not true if one can prove that the new configuration is as effective and robust as the linear optimal filter, but that is extremely difficult. E.g. a priori, the true ATLAS noise correlations are unknown.

4

Test-beam results

4.1 Test-beam setup

The test-beam program at CERN for the Tile calorimeter started in 1993 as RD34. During the last years tests have been performed at the north area in Prevessin using protons extracted through the H8 beam line from the SPS. The proton beam is converted into muons, electrons and pions in the energy range 10 GeV to 400 GeV and focused on the calorimeter at different angles. The program covers all aspects of the calorimeter: mechanics, optics and electronics. The tests of modules with real ATLAS geometry started in 1996 with the barrel module 0. The 1996 and 1998 experimental setups are shown in Figure 4.1. The 1

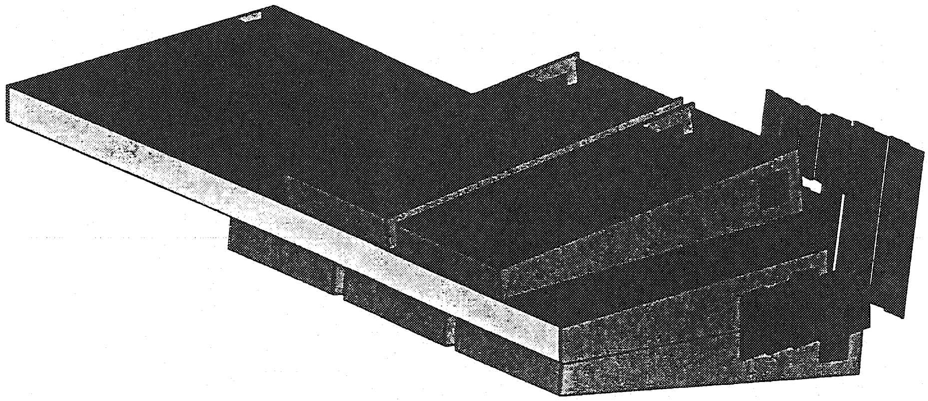

Figure 4.1: Setup of the barrel module 0 test-beam in 1996 and 1998.

m prototype modules from 1995 test-beam are used to measure the lateral leakage. Also visible are the scintillators used as "muon walls". The extended barrel module 0 was tested in 1997, see Figure 4.2.

The analysis of test-beam data is done from ntuples produced by an offline version of the online monitoring program TileMon [30]. During data taking raw data is stored on disk in the ZEBRA format [31]. After the run is finished data is transfered to tape for later retrieval. With TileMon many reconstruction features are controlled by data cards, but the user can also intercept the ntuple creating chain with C or fortran code.

Since the author's contribution concerns the calibration and evaluation of the 1996-

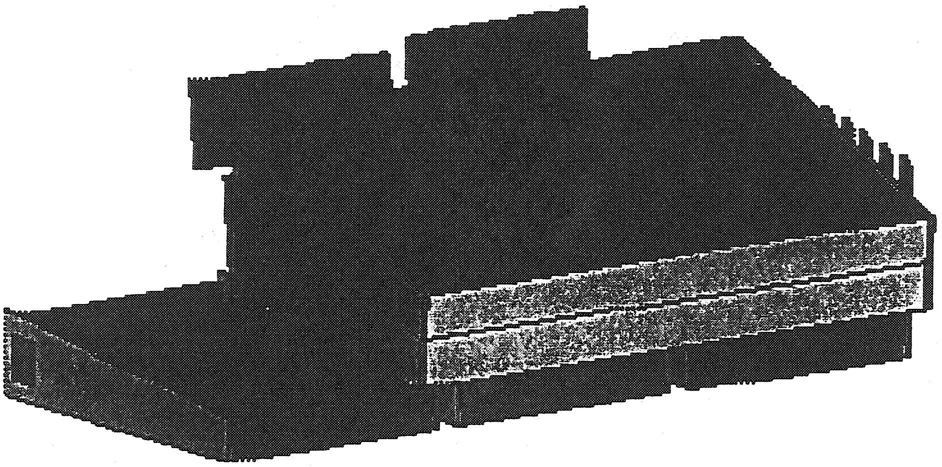

Figure 4.2: Setup of the extended barrel module 0 test-beam in 1997.

1998 fast readout electronics the following sections will give a historical overview of its development and performance.

4.2 The concept of non linear compression, test-beam 1994

A 16 bit Analog to Digital Converter (ADC) capable of a 40 MHz sampling rate was not available, especially not considering the constraints set by the economy and power consumption of the 10^4 readout channels. However, since the calorimeter resolution scales as $\sqrt{E}$ one is led to redistribute the ADC resolution, i.e. signal compression.

The FERMI-project[29] (CERN RD-16) had developed a complete concept to handle the readout from LHC-type calorimeters. Hence FERMI had available a compressor and a 10 bit ADC that could be matched exactly to the requirements of the hadronic and electromagnetic calorimeters. Test-beams during 1994 showed that this was a possible way to go, at least for Tilecal assuming modest bandwidth and slew-rate demands. With two working readout channels, a 0.66% resolution for large signals and stable pedestals were demonstrated with the 200 ns FWHM Tile shaper. For a detailed report see [32].

4.3 A comparative test of non linear compression , test-beam 1995

To demonstrate the operation of the compressor concept, 27 FERMI channels where compared with the standard readout during test-beam 1995 with the 1 m Tilecal prototype modules. The limited bandwidth of the compressor made it impossible to use the 50 ns shaper aimed for in the final design, see Figure 4.3. In order for the test-beam work to progress a temporary 200 ns shaper was implemented. However, even with such a wide pulse a tendency to slew-rate was detected during the critical look-up-table construction. Apart from the slew-rate, the compressor solution performed as expected, see [33] for details.

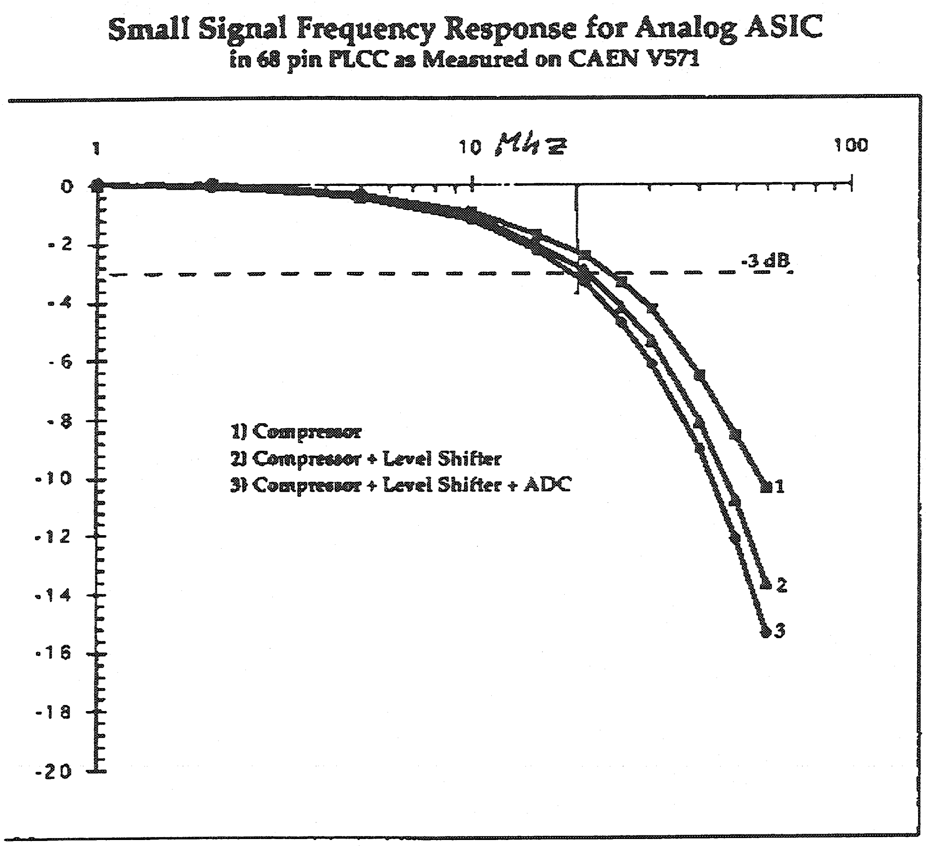

Figure 4.3: Measured bandwidth of the compressor located on the VME board during 1995.

4.4 Approaching realistic ATLAS requirements, test-beam 1996

During 1996 test-beam, 46 channels with FERMI modules were used for the readout of the Tile calorimeter barrel module 0. The most important changes of the fast electronics were a realistic shaper with a FWHM of 50 ns, a new integrated charge injector and a new and faster compressor, see Figure 4.4. All this functionality was located on the 3-in-1 card. The sampling 10 bit FERMI ADCs were mounted in VME crates with 3 ADC's per VME card.

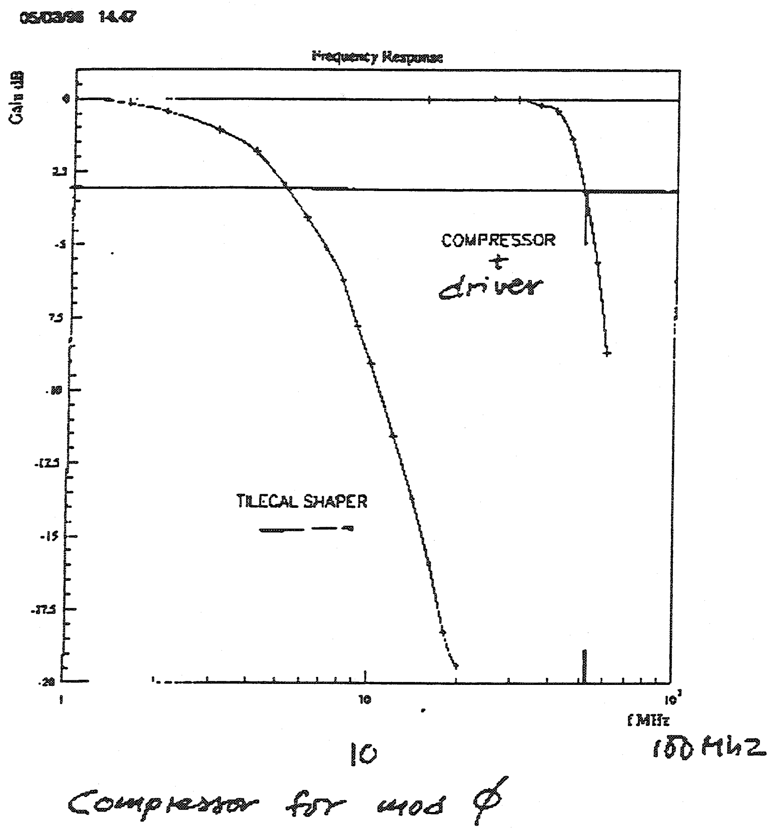

Figure 4.4: Measured bandwidth of the shaper and the compressor [35] implemented in the process Genum Ga 911 located on the 3-in-1 card during 1996.

4.4.1 Pedestal analysis

Measurements of the pedestal, that is the base line without signal, are extremely important. The pedestal contains information about the noise in the system. The noise can in most cases be approximated by a weak stationary process X_i and as such it is characterized by the mean $E(X_i) = P$ and the covariance* kernel $R(j) = \mathrm{Cov}(X(i), X(i+j))$. Both of these properties can easily be measured from a pedestal run. For a comparison with the variables in the optimal filter let $X_i = n_i + P$. The electronic noise is constrained by the requirement to resolve muons in the first and thinnest compartment where the Landau peak is at ~350 MeV and should be sampled at an ADC level of 11 counts for good resolution. The Landau tail stretches down to ~100 MeV. The compartment is seen by two PTMs, consequently the intrinsic noise from the electronics should be sufficiently lower than ~70 MeV/channel to separate the muon signal from the pedestal. During 1996 the charge calibration gave ~0.017 pC per ADC count and the electromagnetic scale from electrons gave 1.37 GeV/pC. Thus the pedestal noise should be much lower than 3 ADC counts. One notes that the gain is a little bit too low (7.5) for the requirement of 11 counts for mouns. The pedestal widths for 1996 are shown in Figure 4.5. We see that the mean of the distribution is ~2.5 ADC

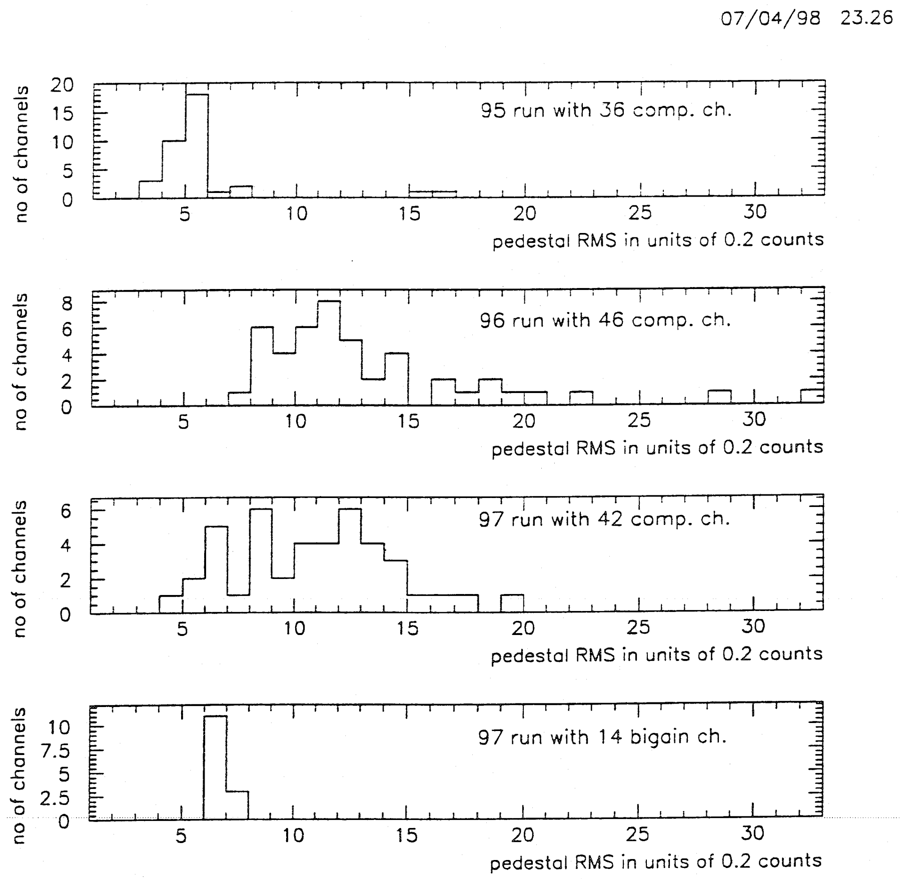

Figure 4.5: Distributions of the RMS pedestal widths for the test-beam periods 1995 to 1997.

counts and has an unpleasant upper tail. There is no real reason to expect the channels to be more noisy than the 1995 values of 1 ADC count. By inspecting the correlations

*The covariance between a and b is defined as $\mathrm{Cov}[a, b] = \langle (a - \bar{a})(b - \bar{b}) \rangle$, and the correlation coefficient ρ is defined as $\rho = \mathrm{Cov}[a, b]/\sqrt{\mathrm{Cov}[a, a]\mathrm{Cov}[b, b]}$.

of the pedestal it is clear that a large part of the noise is correlated, see Figure 4.6. The

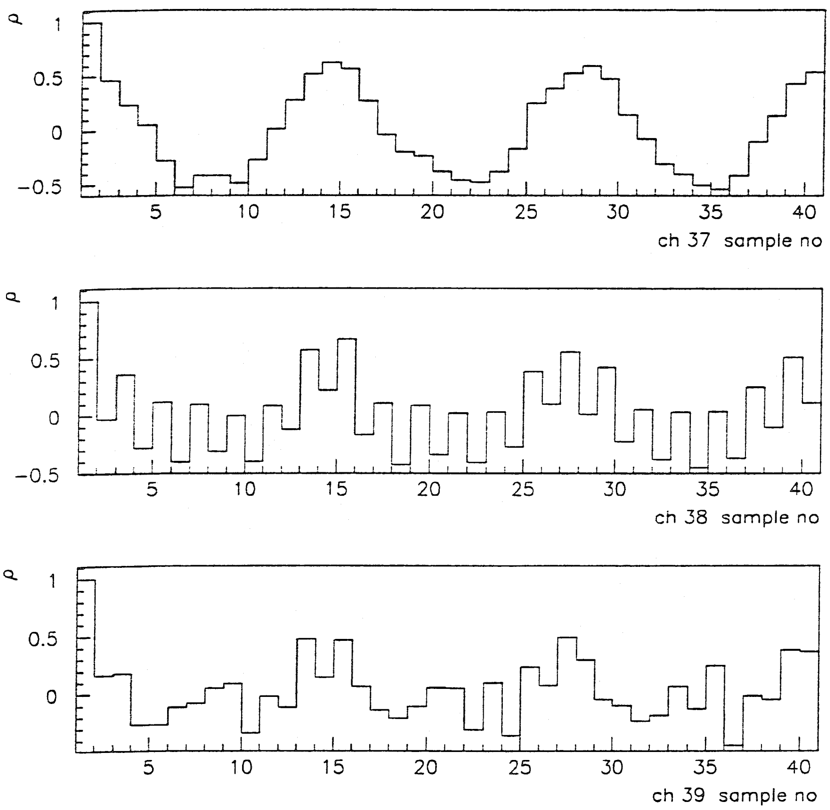

Figure 4.6: Large unexpected correlations seen between samples within the same frame taken from 1996 pedestals. The source was unknown at this point but later part of the correlation could be traced to the 10 bits FERMI ADC boards.

noise is clearly external and probably related to a digital clock. When using exactly the same 10 bits ADCs in a completely different configuration during 1998 large correlations were observed for the 10 bits ADC cards, hence the 10 bits ADC cards is one part of the contributions to the correlated noise, the exact origin of the remaining contributions was never established. Another aspect of the pedestal is related to the fact that the system is AC coupled. Due to the AC coupling the mean pedestal level will depend upon the integral of the signal per time interval. Since the pulse is unipolar, or positive, the net integral is positive. Hence the pedestal must be estimated on an event to event basis. An increased pedestal level was e.g. clearly seen during charge injection runs when the interval between injections was set very tight, see Figure 4.7.

4.4.2 Pulse shape invariance

The requirement of shape invariance, i.e. $S(t, Q) = Qs(t)$, is very strong. E.g. the requirement of linearity is just a sub requirement which is quite explicit at the pulse peak where

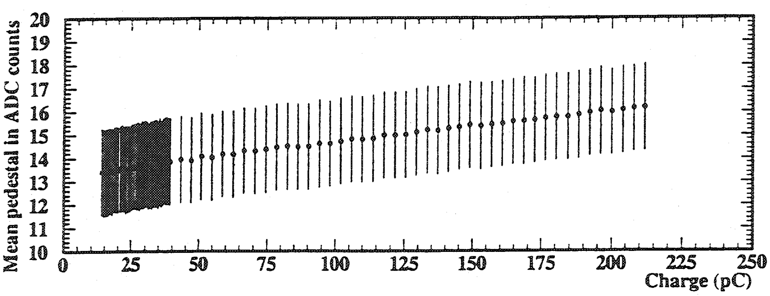

Figure 4.7: Pedestal drift during 1996 charge injection due to the unipolar shaping and AC-coupling. The error bars are the event to event spread for one pedestal sample and does not represent the error of the mean.

$S(t_{peak}, Q) = Q$. So the next property to check after evaluating the pedestals is the shape invariance. In order to reconstruct the pulse shape a handle on the phase between the pulse and the trigger is needed. Unfortunately the injector phase was not properly stored during data taking so some other method had to be used. There exists a time to digital converter in all test-beam setups, but it is not available during charge injection. One practical way to estimate the phase difference τ is to use the samples themselves. Since the pulse is smooth and nearly symmetric, the so called slope [36] is a good choice. The slope is defined as

$$\text{slope} = \frac{ADC'_{max+1} - ADC'_{max-1}}{ADC'_{max}} \tag{4.1}$$

where ADC'_{max+1} means the pedestal corrected ADC sample one sample after the maximum ADC sample. That this is reasonable is clear after Taylor expansion of the response function $f()$ (t equals the time of the true peak maximum)

$$\begin{aligned}
ADC'_{max+1} &= f(t + \Delta + \tau) \simeq f(t + \Delta) + \tau f'(t + \Delta) && (4.2)\\
ADC'_{max-1} &= f(t - \Delta + \tau) \simeq f(t - \Delta) + \tau f'(t - \Delta) && (4.3)\\
ADC'_{max} &= f(t + \tau) \simeq f(t) + \tau f'(t) && (4.4)
\end{aligned}$$

where Δ is the time between samples, i.e. in this case 25 ns. We finally get

$$\text{slope} \simeq \frac{f(t+\Delta) - f(t-\Delta) + \tau(f'(t+\Delta) - f'(t-\Delta))}{f(t) + \tau f'(t)}. \tag{4.5}$$

Assuming a smooth and symmetric pulse we get a sensitive estimator at $\max_\Delta |f'(t + \Delta)|$. Since $f'(t) = 0$ we have

$$\text{slope} \simeq \frac{2\tau f'(t+\Delta)}{f(t)}. \tag{4.6}$$

However, the mapping of slope to time is not required to be linear. It is enough if it is bijective. Since the random phase distribution in time is flat, a linear time is simply found by rebinning the slope distribution such that an equal number of events is found in each time bin, see Figure 4.8.

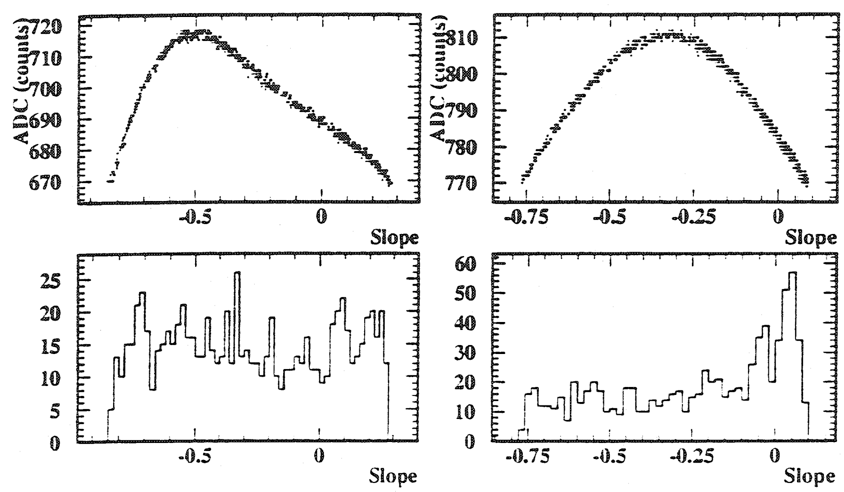

Figure 4.8: Examples of slope distributions from 1996 charge injection data. Since the phase distribution in linear time is flat, knowledge of slope distribution enables construction of a linear time estimator.

Given the phase estimator it is straightforward to reconstruct the pulse shape. For a one channel example of the 62 available amplitudes see the top plot in Figure 4.9. In order to study the shape invariance, the raw compressed pulses must be linearized. To get the absolute scale correct the charge offset Q_0 must be extracted by extrapolation to $S(t) = 0$, see Figure 4.10. Now the linearization and the construction of the LUT can be performed by applying equation 3.13. For an example of a LUT see the top plot in Figure 4.11. Given the LUT it is possible to check the intrinsic quantization resolution of the system given an ideal ADC. Propagation of error yields

$$\sigma_Q = \frac{\partial LUT(ADC)}{\partial ADC}\sigma_{ADC}. \tag{4.7}$$

For σ_{ADC} one can assume a flat distribution, hence $\sigma_{ADC} = 1/\sqrt{12}$ counts. For an example see the bottom plot in Figure 4.11. A comparison is also made to the intrinsic resolution of the calorimeter, and we see that by design we are on the safe side concerning the theoretical quantization noise†. After LUT expansion we see already by eye in the lower plot in Figure 4.9 that the shape invariance is far from conforming to the 1% requirement. We know by now that this means that the optimal filter will not work, and also, that the LUT(ADC) is not a valid linearization. This is of course very bad. The reason for the bad shape invariance is clearly insufficient slew-rate in the analog chain, the most striking feature being the timewalk of the peak position clearly visible by eye in the expanded pulse plot. One other important aspect concerning the requirements is seen in the example of the LUT in Figure 4.11. It saturates already at 200 pC, while the requirement says 800 pC! Due to

†It is in place here to notice that since the quantization noise enters after the compression it is not properly handled by the optimal filter.

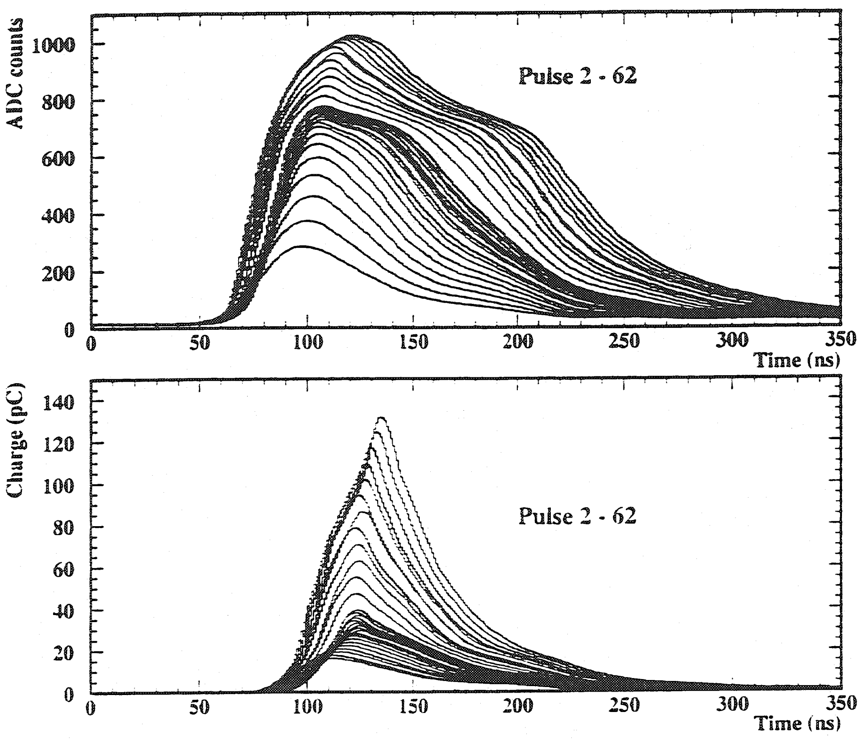

Figure 4.9: Examples of the compressed (top) and $LUT(ADC_i - P)$ decompressed pulses (bottom) reconstructed from one channel in charge injection runs during 1996.

the pedestal the real saturation is even lower than 200 pC and the spread of this saturation among the channels ranges from 100 to 190 pC. By design the charge injector in the 1996 version of the 3-in-1 handled only up to 400 pC, however due to an error in the matching to the ADC, saturation sets in far too early. Great care had to be taken during the analysis, e.g. for the investigation of 400 GeV pions.

4.4.3 Charge estimator resolution

It is impossible to speak about resolution without at the same time mentioning the method for charge reconstruction. Assume for a moment that we had a square pulse shape 5 samples long without time jitter and that the pedestal noise is orthogonal. Then the resolution of an unweighted sum of 5 signal samples‡ would be $\sqrt{5}/5$ times the one sample estimator. Now, first of all, the Tile shaper is not a square but tries to mimic a Gaussian. The Gaussian is the unique solution to the problem of finding a pulse that is as short as possible both in the time and in the frequency domain, this is highly desirable. Given the pulse shape we know how to construct the optimal filter estimator. Unfortunately we see in Figure 4.9 that the pulse is not invariant and the optimal filter is no longer an option. One would expect

‡This is actually the optimal filter for this configuration

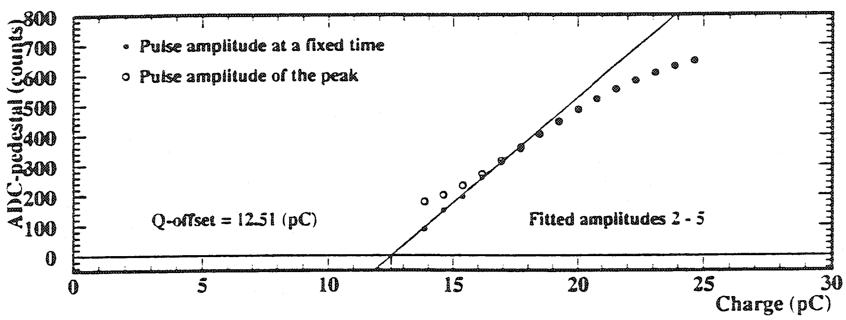

Figure 4.10: Extrapolation of the charge offset Q_0 at $S(t) = 0$.

that the unweighted sum is not so far from optimum, but we see in Figure 4.12 that the resolution and linearity is so bad that it is almost meaningless to perform basic test-beam physics analysis.

In order to save the test-beam analysis, some alternative method had to be invented with the only requirement to perform well enough under test-beam conditions. Many different configurations were tested. Finally the method that was most effective was to first add samples of the compressed pulse and then linearize. The optimal number of samples was 8. The compressed sum was still phase dependent but that could be remedied by a slope correction. So in the end, the new method had the structure of a nonlinear 2 dimensional (2D) mapping

$$Q = LUT(\max_{i_0} \sum_{i=i_0}^{i_0+7} ADC'_i, \text{slope}) \tag{4.8}$$

It was implemented as a grid with 127 bins in amplitude and 150 bins in phase. The amplitude used spline interpolation, while the slope used linear interpolation. As we can see in Figure 4.13, the resolution is below 0.5% and the linearity is by construction better than 1%.

In the normal case one would keep the frame of samples fixed in time. However, the peak position was not stable in the hardware. Since the LUT is critically dependent on the slope, the definition of slope was set at the center of the maximal sample sum which is easy to find independently of sample shifts. The problem associated with the maximization is that the estimator picks up a noise dependent bias. This was solved with a fixed sum for small signals where the slope parameter was useless anyway.

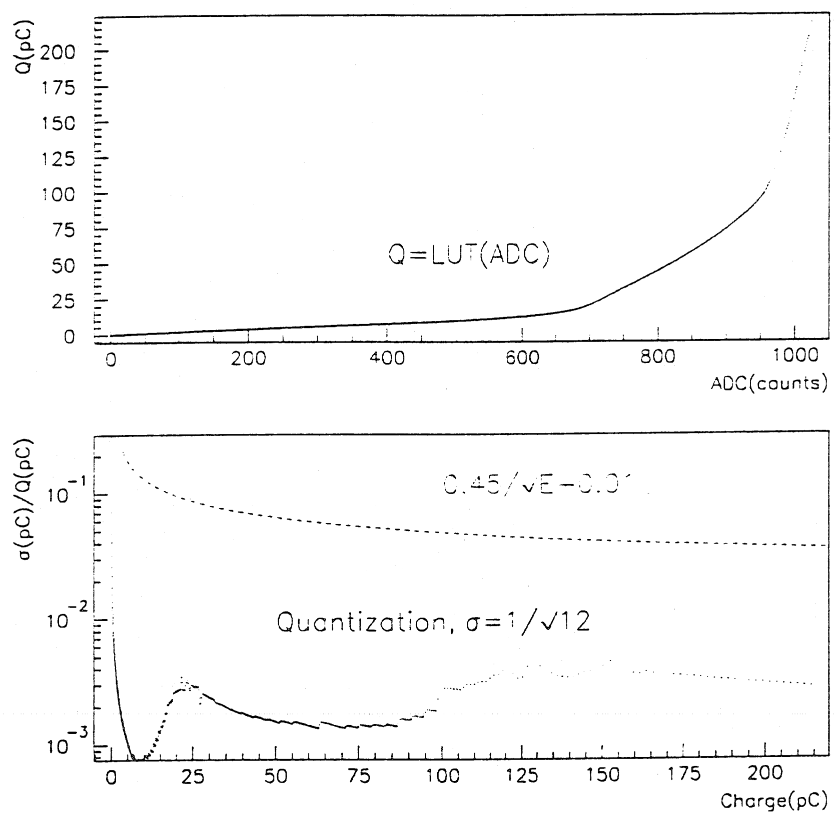

Figure 4.11: Example of a LUT from 1996 (top). Given the LUT (top) an estimation of the quantization noise assuming an ideal ADC is shown (bottom). Included is also a comparison to the intrinsic calorimeter resolution.

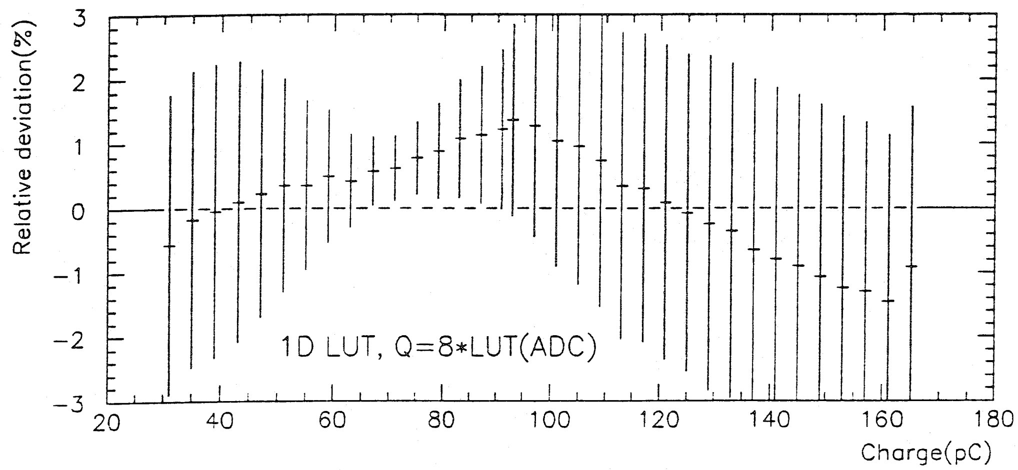

Figure 4.12: One channel example of the relative deviation with the 1D LUT in 1996. The estimator is an unweighted sum of 8 linearized ADC samples. Both the linearity and the resolution is visible in the plot. The resolution is the height of the error bars.

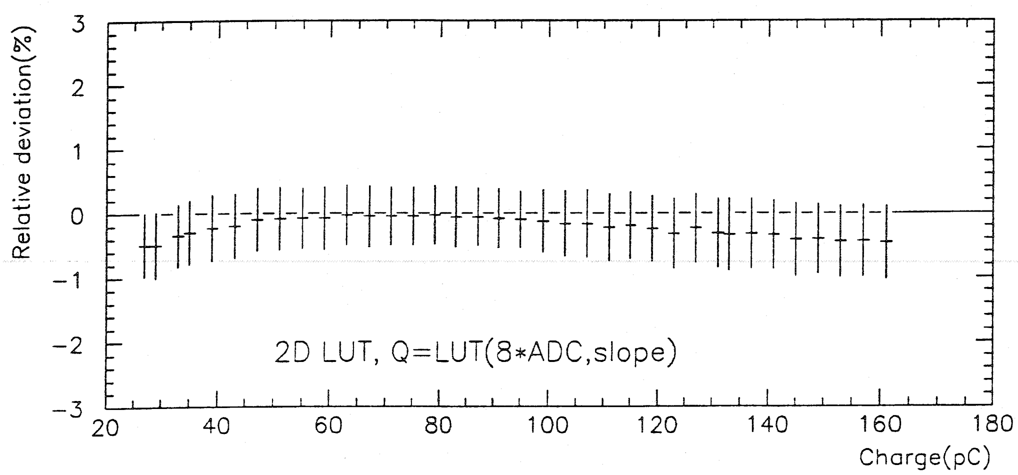

Figure 4.13: One channel example of the relative deviation with the 2D LUT in 1996.

4.5 Second iteration and the bigain backup solution, test-beam 1997

In the 1997 test-beam[§] setup, two extended barrels were under scrutiny. One module (ANL) was equipped with 28 channels using 10 bit ADCs with nonlinear compression. The other one (BNL) had 14 channels of 12 bit commercial ADCs with bigain compression (cells A14-A16, B13-B15 and D7), and 14 channels of the same type as in the ANL module. The 12 bit bigain was developed as a backup solution since clearly the nonlinear compressor design had problems both in performance and robustness. The bigain compression concept is very simple. There is one channel with high gain for small signals, and one channel with low gain for large signals. If the high gain channel saturates, only the low gain channels is used. During 1997 the gain difference between low and high was 16. The drawback with the bigain solution is that the matching to the calorimeter resolution is not optimal and it is more expensive since the number of readout channels has to be doubled. However, it is linear by design. The bigain 3-in-1 also had a new passive shaper. The 3-in-1 charge injector had an increased theoretical capacity of 640 pC but was only linear up to 400 pC.

The compressor was patched in order to improve the slew-rate. It used only the positive side of the differential output since this was observed to be faster than the negative side. Concerns were raised that this would influence the noise in a negative way. But we can see from Figure 4.5 and 4.14 that the noise in the compressor channels are dominated by the correlated noise in a very similar way as in 1996. Once the correlated noise is removed, e.g. in the 12 bits channels, we are back to the same noise level as in 1995. The small signal performance with the default implementation of the 2D LUT estimator is shown in Figure 4.15. The top plot shows the muon signal compared to the pedestal width in a compressor cell in the ANL module. The bottom plot shows the same thing but for a bigain cell in the BNL module. The algorithm for the fit of a Landau distribution convoluted with a Gaussian to the muon signal is due to [39]. In Figure 4.15, the Landau peak is a little bit too high to match the requirement, but we see a better muon separation in the 12 bits bigain system then in the 10 bits compressor system. During 1997 the conversion between charge and energy was 1.26 GeV/pC. We can also notice that for these two cells the inter-calibration was not very good.

4.5.1 Compressor: pulse shape invariance

The compressor had been modified since the 1997 test-beam in order to improve the shape invariance. The measurable results of the improvements are shown in Figure 4.16. Clearly it is a lot better than in 1996 but unfortunately the deviations are larger than 1% over the full dynamic range.

4.5.2 Compressor: charge estimator resolution

An attempt was made to apply optimal filters. The shape invariance was not good enough over the full dynamic range so the different filters were created in different regions where the shape appeared to be invariant. However, we see in Figure 4.17 that the performance once the LUT corrected non linearities set in ($\sim$ 27 pC) is not acceptable. Just as in 1996

[§]From analysis point of view the most memorable problem during this period concerned cross talk between the fibers within the same "transparent" profile.

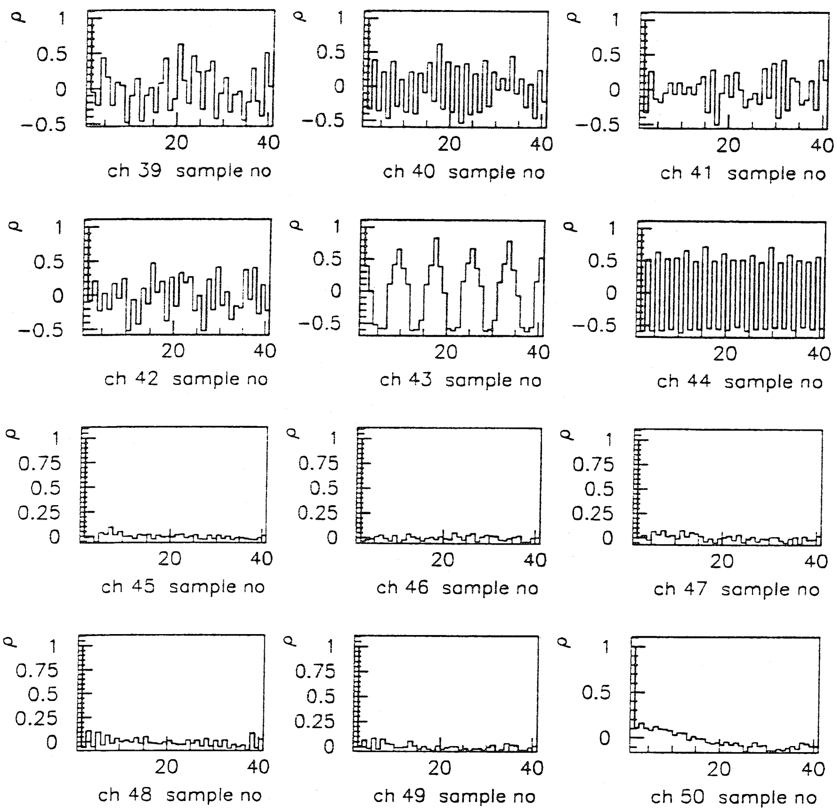

Figure 4.14: Correlations between samples within the same frame. Channels 39-44 are compressor 3-in-1s, and channels 45-50 are bigain 3-in-1s. In channels 45-49 the noise is very close to the definition of orthogonal noise. The presence of correlated noise only says something about the overall noise immunity of the system. Clearly in channels 45-49 the one sample pedestal spread is a good estimator of the internal noise.

the best performance was achieved with the 2D LUT technique, see Figure 4.18. Note that the dynamical range increased from $\sim$ 150pC in 1996 to 400 pC in 1997.

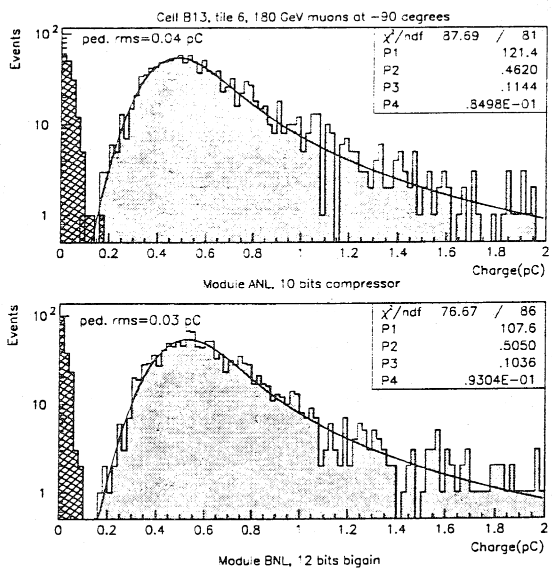

Figure 4.15: The 180 GeV muon signal in cell B13 is compared to the pedestal width for a cell read out with compressor electronics (top) in the ANL module. The bottom plot shows the same thing but for a bigain cell in the BNL module. The Landau peak is a little bit too high to match the requirement, but we see a better muon separation in the 12 bits bigain system then in the 10 bits compressor system. According to [39] the most probable value $MOP = P2 - 0.13P3$, and the Gaussian contribution is parameterized by $\sigma = P4$.

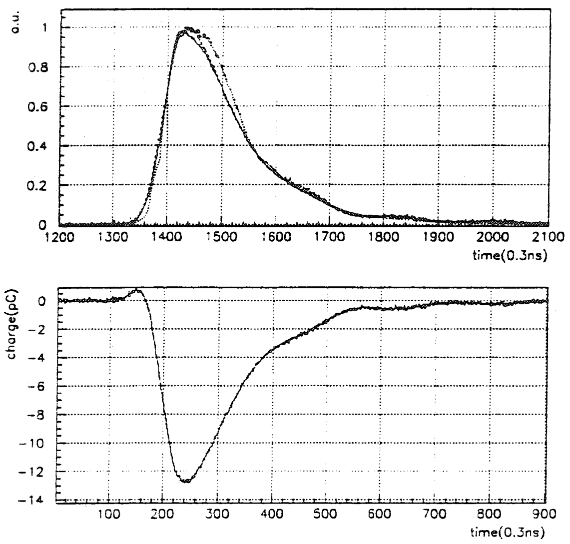

Figure 4.16: In the top plot the shape invariance of $s(t)$ is shown for small, medium and large signals for a typical compressed channel during 1997. The bottom plot shows the bias and leakage $(b + l_i)$ for the same channel which is nearly identical to the ones reconstructed in 1996.

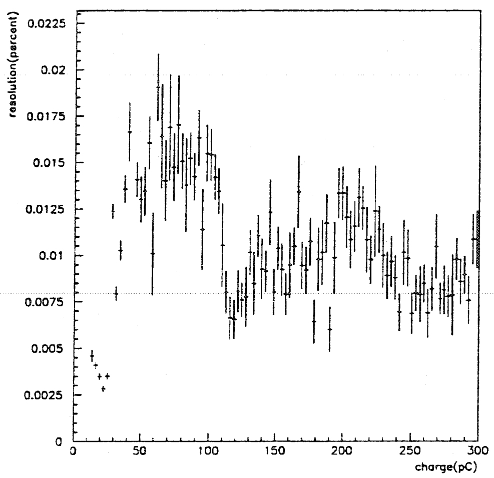

Figure 4.17: Charge resolution achieved with optimal filters using 1997 compressor data. Due to the pulse distortions different filters are applied in the regions [0,27], [27,55], [55,100] and [100,190] pC. Note how well the filter behaves in the undistorted and linear region below 27 pC.

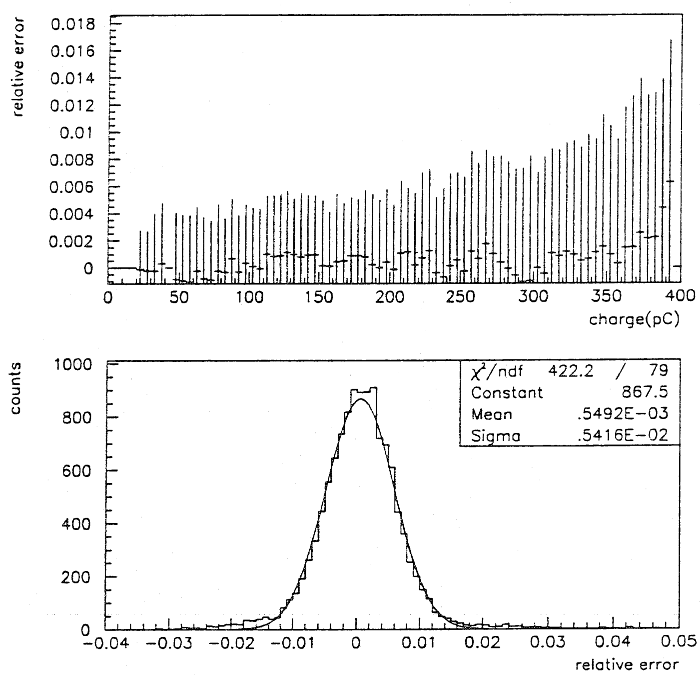

Figure 4.18: One channel example of the relative deviation for the 2D LUT estimator during 1997. From the RMS of the projection in the bottom plot we see the that resolution is of the order 0.54%.

4.5.3 Bigain: pulse shape invariance and resolution

The bigain system had a new passive shaper. Early studies as soon as charge injection data was available indicated superior shape invariance of the system, see Figure 4.19, and a resolution with an unweighted sample sum in the 0.1% range for large signals. The bigain

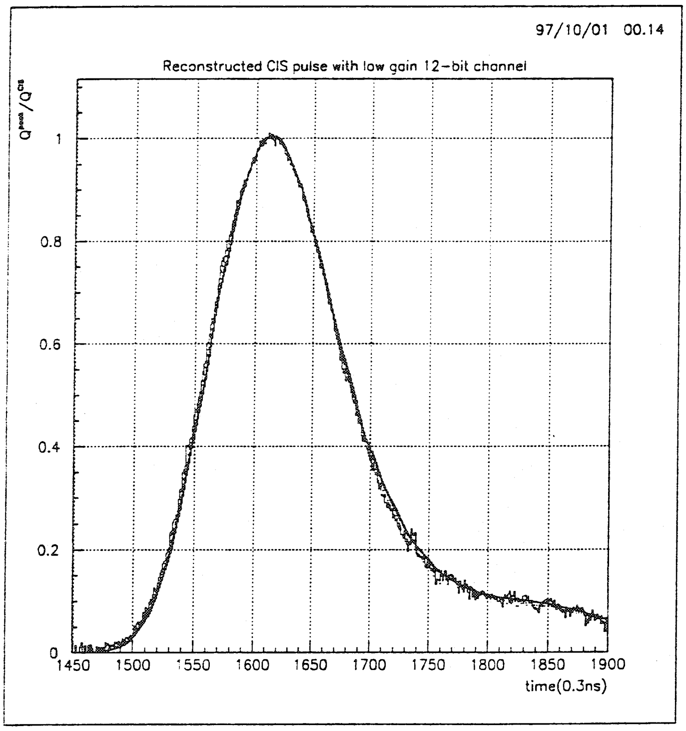

Figure 4.19: Shape invariance of $s(t)$ for the passive shaper in the bigain 3-in-1 from 1997 low gain charge injection data. A small and a very large pulse are superimposed.

system was evaluated in detail by Eftymiopoulos and Kontos [37]. They demonstrated a linearity and resolution for large signals below 0.5% using only an unweighted sum of 5 samples. Note that no linearization is needed! At this point it was clear that the compressor concept was out of the game and a decision was taken to go for the bigain solution from now on. The compressor simply had too many unsolved problems. Beside the ones mentioned, one problem concerned the fluctuations in the AC coupled pedestal levels on each side of the non linear component, an obvious nightmare for calibration in the presence of pile-up noise. However, one question remained for the fast readout: could the bigain 12 bit ADC be replaced by a 10 bit ADC?

4.5.4 Global correlations

A global property of the electronics that needs to be kept low is the correlations between channels. There are two aspects of this, noise correlations, and signal correlations. Both can be very dangerous when physical objects e.g. jets are constructed from a large collection of channels. The electronic cross-talk could e.g. be tested by injecting charge channel by channel and look for correlations in other channels. This was not tested since all channels in the setup were injected at the same time in order to reduce the overall time of the calibration procedure. However the noise correlations between the channels can be measured from a pedestal run and an example is shown in Figure 4.20.

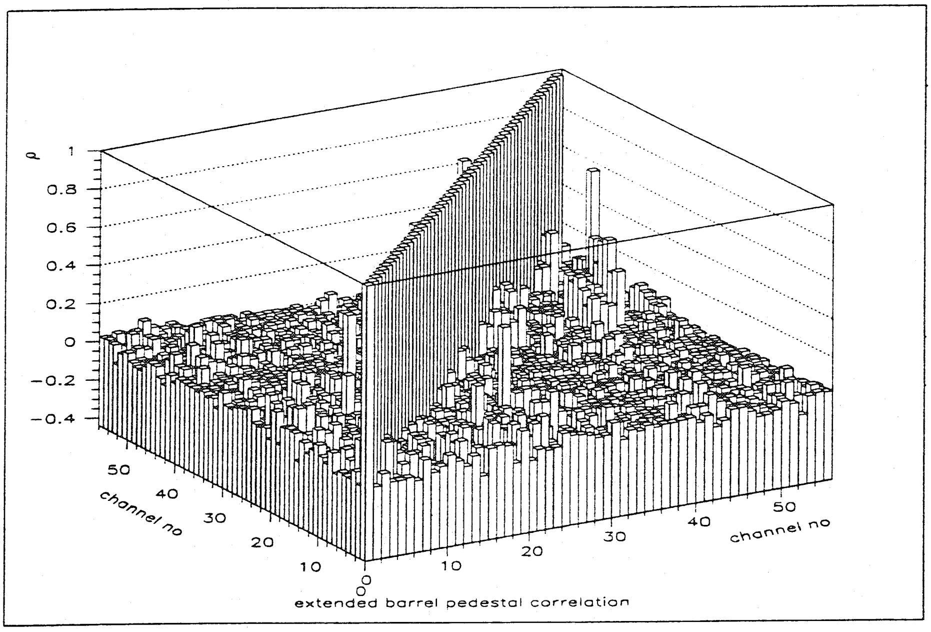

Figure 4.20: Correlations between the channels in the BNL extended barrel module 0. A channels is 100% correlated with itself thus the diagonal is 1. 12 bits bigain are channel 33-38, 45-50 and 55-56. The matrix is symmetric. Unfortunately negative correlations are not visible in the 3D plot. Both 10 bits and 12 bits channels show a correlated behavior. The cluster in the upper right corner is actually 12 bits ADCs. The level of the correlated noise is so low so that it should not affect the results from the test-beam analysis.

4.6 10 bit or 12 bit ADC for bigain compression, test-beam 1998

In 1998 module 0 was tested again with 45 PMTs connected to bigain 3-in-1 cards. The 3-in-1 card had a new improved shaper and a new injector capable of 800 pC with low leakage. The difference in gain between low and high gain was increased to 64 compared to 16 during 1997 in order to cover the same dynamic range with 10 bit ADCs. A detailed description of the 3-in-1 can be found in [38]. 27 PMTs used 10 bit FERMI ADCs and 18 PMTs used 12 bit commercial ADCs (cells A7-A10, BC6-BC9 and D3). In total there were

90 ADC channels.

4.6.1 Calibration and stability

Since the injector had two capacitors and only the large one was known to high precision¶, data had to be cross calibrated. However, the range of charge injection data in the overlap region was not large enough. This caused at lot of technical problems and made the actual calibration very tedious. One reason to use the small capacitor was that it should give a smaller leakage pulse, but as we can see in Figure 4.21 the difference between the small and large capacitor is very small‖. Another technicality in the pulse reconstruction is that

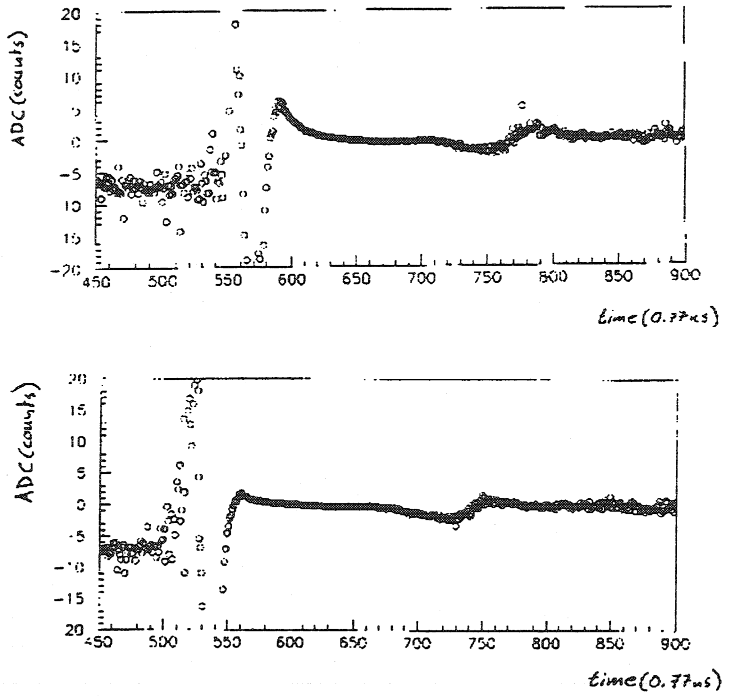

Figure 4.21: Bias and leakage(b+$l(t)$) for charge injection with the large capacitor (top), and the same plot for using the small capacitor (bottom). The improvement of smaller leakage with the smaller capacitor by no means compensates for the large technical complications in the calibration procedure, e.g. in the cross calibration.

frames shifted one sample have to be removed before the averaging is done, see Figure 4.22.

The purpose of the charge injection calibration is of course to assert the absolute level of the reconstructed charge. The references are the reference voltage and the 100 pF capacitor in the injector. The technical problem with lack of the data for cross calibration made the high gain data very unreliable. However, cross-checks could be made with the Cs calibration

¶For very small capacitors, stray capacitance starts to be important.

‖If calibration data had been taken with the large capacitor only, the work load in the calibration procedure had been largely reduced and a much better absolute scale would have been achieved.

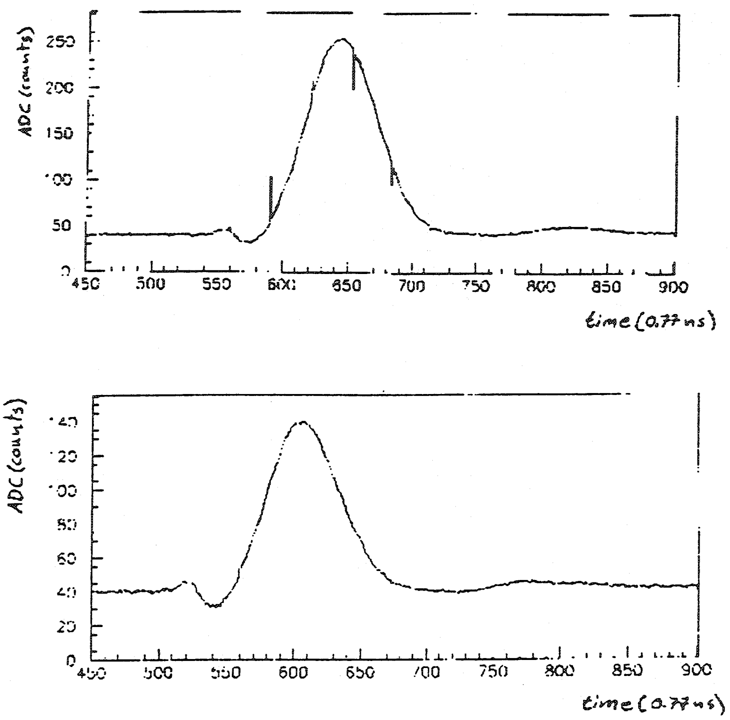

Figure 4.22: Small reconstructed pulse where shifted frames are not removed before the averaging (top), the same plot with shifted frames removed. Note the leakage pulse in the beginning of the pulse, this is what is shown in Figure 4.21.

that suggested that using only the 5.1 pF capacitor, corrected for an additional 0.1 pF of stray capacitance, gave reasonable results. Without any external reference as the Cs system, one would be blind in this case since there is no guarantee for the precision of very small values of the effective capacitance. The long time charge reconstruction stability of the low gain channels given a fixed calibration is shown in Figure 4.23. The effects of applying the calibration constants from charge injection runs are shown in Figure 4.24. It is hard to draw any conclusions concerning the stability since the hardware was changed several times during this time period. Several channels had a tendency to change the response with a factor of two even within the same run.

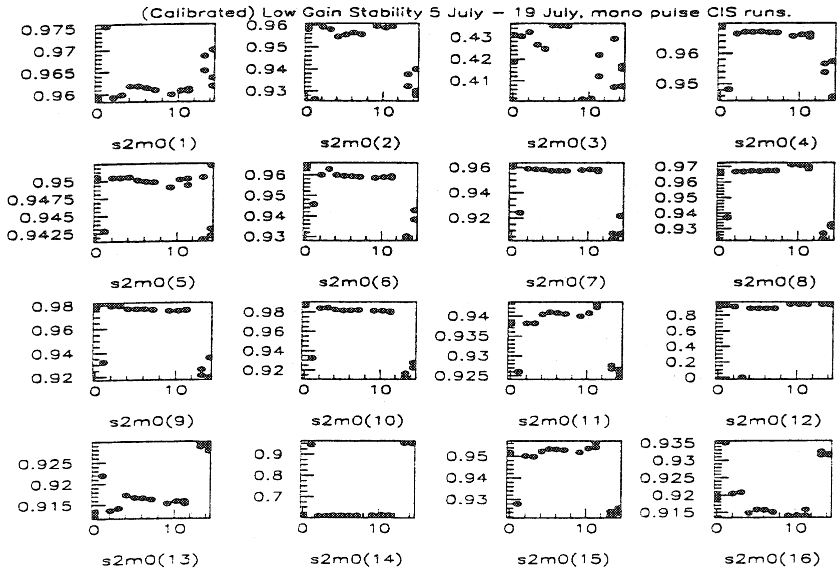

Figure 4.23: Long time charge response stability of the low gain electronics to a fixed amount of injected charge. The calibration constants are held fixed during the full time period. Please note that the scale is not fixed. The y-axis shows the response divided by the injected charge, and the x-axis shows the time in days.

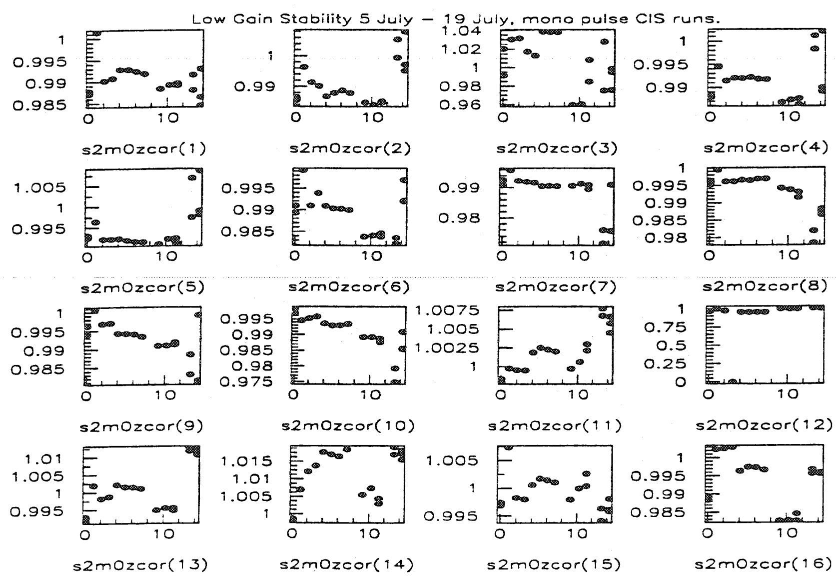

Figure 4.24: Same plots as in Figure 4.23, but with charge calibration constants applied.

4.6.2 Pedestal analysis

During 1998 the same 10 bits ADCs were used as in 1996 and 1997. However, now they were connected to bigain 3-in-1s. One striking feature of the 10 bits pedestals is the presence of strong correlations, see Figure 4.25. The same type of strong correlations were seen in 1996 and 1997, but the correlations were even stronger and the σ almost twice as large, so the 10 bits ADCs cannot alone explain the large noise in 96-97 data. The small differences between low and high gain, see 4.25 and 4.26 tells us that during 98, the main correlated noise source is the 10 bits ADCs. However, as we see in the pedestal overview in Figure 4.27 the noise levels are very low.

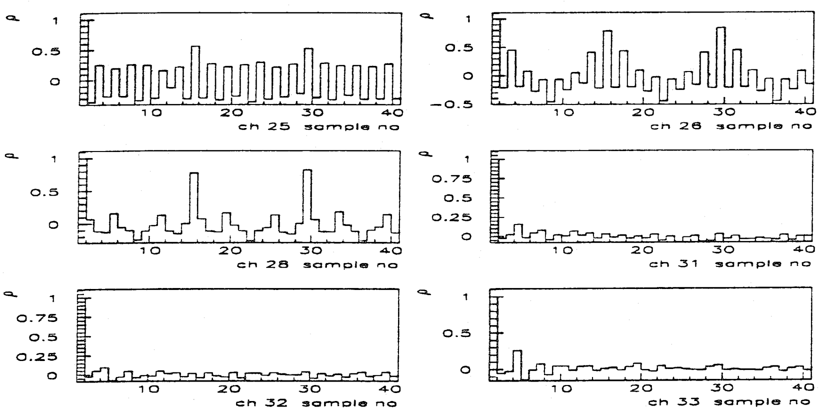

Figure 4.25: Sample correlations for low gain channels during 1998. The channels 25, 26 and 28 show 10 bits ADCs and the channels 31, 32 and 33 show show 12 bits ADCs.

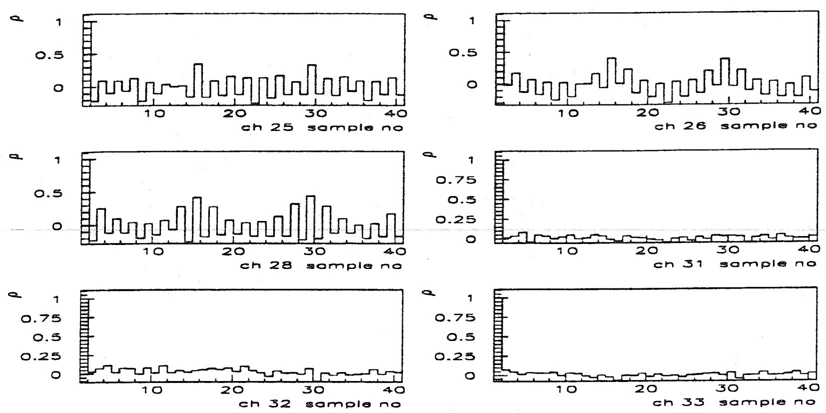

Figure 4.26: Sample PMT channels as in Figure 4.25, but for high gain.

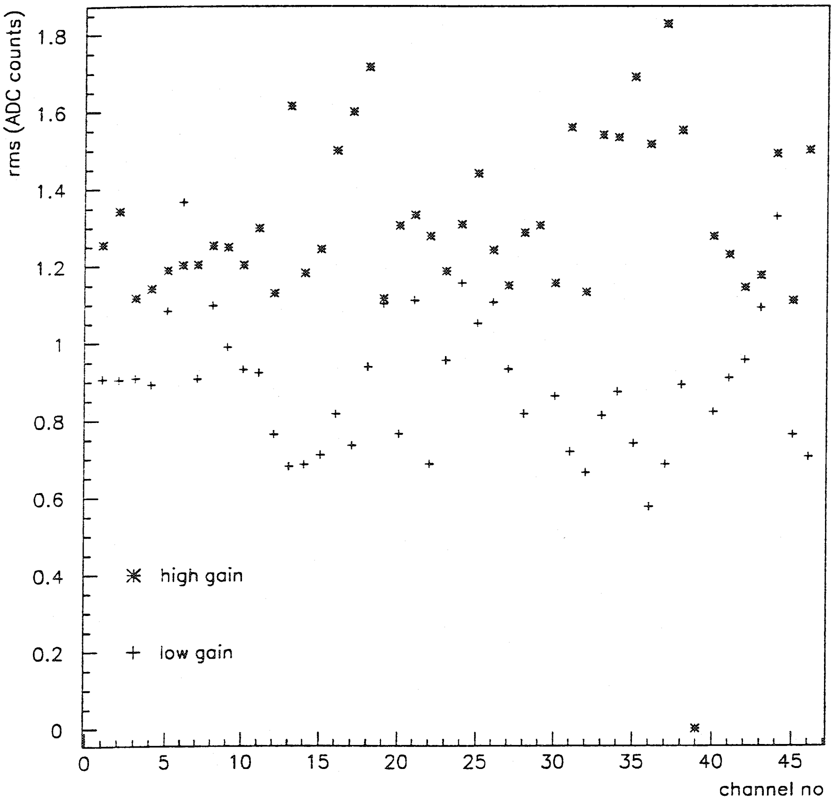

Figure 4.27: Overview of the pedestal RMS during 1998. Both low and gain gain channels are shown. Since the vertical scale is in ADC counts it does not reflect the physical noise levels. 12 bits ADCs have 0.007 pC/count in low gain and 0.45 pC/count in high gain. For the 10 bits ADCs the numbers are 0.014 pC/count and 0.87 pC/count. Channel 13, 16-18, 31-38 are 12 bits ADCs.

4.6.3 10 bits or 12 bits ADCs

One of the goals with the 1998 test-beam was to verify the performance with 10 bits ADCs. The place where the calorimeter resolution is most affected is in the low gain channel at the gain switch, see Figure 4.28. The figure illustrates single cell comparisons between analytical calculations, 12 bits charge injection data in 1997, 10 bits truncated from 12 bits in 1997 and results with 10 bit data taken with the new in drawer Digitizer in the end of 1998. Details concerning the 10 bits truncated data can be found in Publication I. The Digitizer data was analyzed and no severe deviations from the simulations were found, except for large low frequency noise in a few channels. The problem could easily be traced to the motherboard hardware. The margin is still good between the calorimeter and the intrinsic Digitizer resolution, remember that the two contributions are orthogonal. Electron resolution during calibration runs is not believed to be relevant for the final energy resolution since they are only used for the absolute scale calibration. One might worry if the single cell assumption really is the worst case. But any vicious energy distribution among the cells, e.g. at the gain switch, cause the resolution to scale in the same way as the calorimeter so the margin remains the same at higher energies as at the gain switching point.

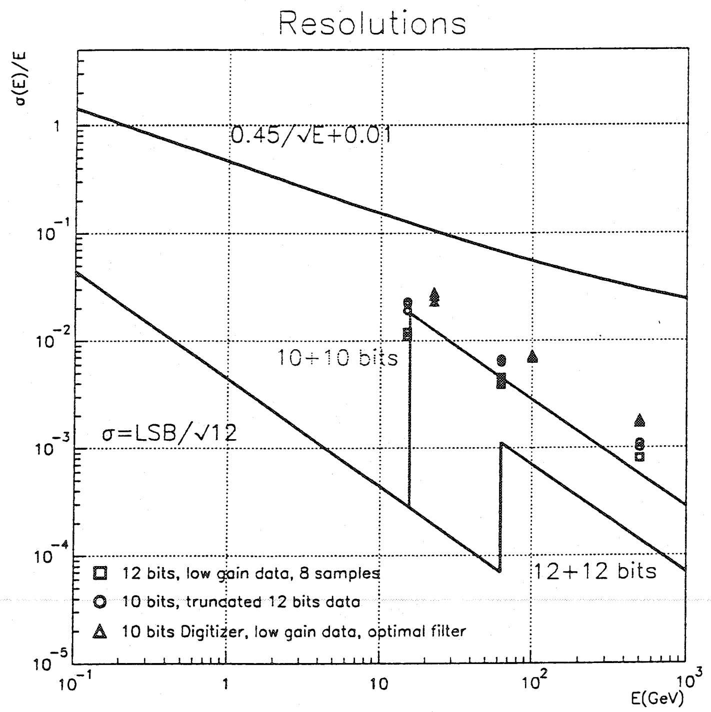

Figure 4.28: Resolution for a single electronics channel. The points represent charge injection data and the lines represent analytical calculations. These are compared to the intrinsic resolution of the calorimeter. Remember that for one cell in the calorimeter there are two electronics channels.

5

Jet reconstruction

The concept of collimated hadrons with high multiplicity as the result of a fragmentation process appeared already in the end of the 60's in deep inelastic scattering, see e.g. [40]. The first really convincing experimental evidence for hadronic jets came from dijet events observed in 1975 in e^+e^- collisions [41]. However, before we can say anything qualitative, the notion of a jet has to be defined. The first and most popular, at least for hadron collisions, is due to Sterman and Weinberg [43]. They demonstrated in 1977 a divergence free observable in terms of cross-section for the energy flow within a cone, using LO QCD calculations. This class of jet algorithms, not unexpectedly, goes under the name of cone algorithms. As a consequence of the calculation they also concluded that dijet events will dominate at high energies as a result of the asymptotic behavior of the coupling constant in QCD. The default cone definition is due to the Snowmass accord [42], where the boost invariant jet observables are

$$E_T = \sum_i E_{T_i},$$

$$\eta = \sum_i \frac{E_{T_i}\eta_i}{E_T},$$

$$\phi = \sum_i \frac{E_{T_i}\phi_i}{E_T}.$$

The index i represents all particles within the cone R, where R is defined as $R = \sqrt{\delta\eta^2 + \delta\phi^2}$. R is typically between 0.4 and 0.7. The energy E_T is the transverse energy relative to the beam axis, i.e $E_T = E\sin\theta$. The cone algorithm defines the jet in terms of two thresholds: E_{seed} and E_{jet}. The algorithm is

1. For each cell in the (η, ϕ) plane initiate a jet if the cell energy is larger than E_{seed}. The jet direction is given by the jet seed.

2. Sum all cells within the cone R around the jet direction. If the new jet axis does not coincide with the jet seed, iterate until a stable direction is achieved.

3. Keep the jet if the energy is larger than E_{jet}. Repeat 1 until there are no cells left.

In the analysis that follows, the iterative procedure in not included, and any jet overlap is not treated.

Later it has become more and more evident that the definition should be what is called infrared and collinear safe in order to easily compare measured quantities to higher order calculations. This property is not intrinsic for the cone algorithm, however the situation can be greatly improved by modifications of the iterative version [48]. An approach that is intrinsically safe is the so called k_T algorithm [46, 47] inspired by the clustering technique [44]. The main reason for the popularity of the fixed cone, especially in hadron colliders, is that it is easier to control instrumental effects than for the clustering technique.

From the physics point of view there are many reasons for being interested in jets. Apart from QCD, Higgs and the top quark are the good examples. If for example Higgs is a SUSY Higgs, it is very likely that the first evidence will appear as an excess in the $b\bar{b}$ invariant mass spectrum. Measurements of the top quark which also are very important both for the SM and for finding new physics, constitute the state of the art in jet spectroscopy. And for searches of SUSY, jets are extremely important since the dominating production is through squarks and gluionos.

5.1 Jet reconstruction in ATLAS

To cover all aspects of jet reconstruction is very difficult since even without the instrumental effects included, there are many non trivial issues: out-of-cone QCD radiation, soft underlying events, differences in the fragmentation etc. What I will try to do is to highlight the experimental aspects of jet reconstruction in the ATLAS barrel calorimeter and indicate the energy resolution performance using very basic techniques. A more detailed description can be found in Publication II.

As we can see in Figure 5.1, the jets are measured by a large set of calorimeters that have very different behaviors*. The picture is further complicated by the existence of unsampled or "dead" material inhomogeneously distributed in the detector. The dead material is found e.g. in the beam pipe, inner detector, cryostat walls, support structures and the coil.

The dominating experimental contributions to the jet energy resolution are the non compensation, losses in dead material, out-of-cone showers and noise. The investigation of all these effects require full detector simulation. In this case a very detailed description of the ATLAS detector is implemented in GEANT [45]. The jets are light quark dijets events generated at fixed η and energy. For the energy losses found in dead material volumes see Figure 5.2. The jet energy response using only the eletromagnetic scale calibration is shown in Figure 5.3. In Figure 5.3 we see that the jet energy reconstructed at the eletromagnetic scale depends both on the energy scale due to the non compensation, and on the cone size since the jets become narrower at higher energies. The non compensation is reduced by energy dependent weighting which makes use of the calorimeter segmentation. The energy deposited in dead material can be estimated by the geometrical mean of the energy detected in compartments surrounding the dead volumes and by the use of extra scintillators sampling the shower. The noise level will influence the weighting in such a way that compartments with low signal to noise will be weighted less. In order to disentangle the instrumental effects on the jet energy reconstruction, the jet energy response within a cone in the calorimeter is compared to a "true" cone energy E_{true} constructed by the fragmented particles. The only experimental effect applied to the true particles is the bending in

*The possibility to improve the resolution by using charged tracks in the inner detector is not studied. However the dead material in the inner tracker is included in the simulations.

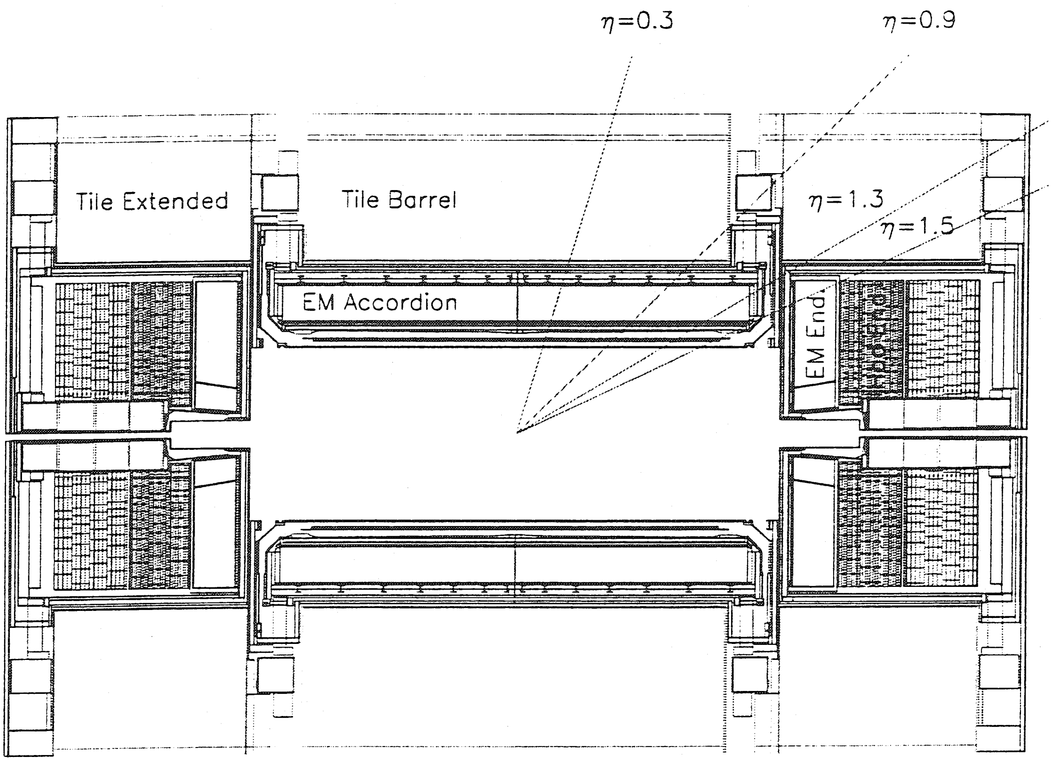

Figure 5.1: Overview of the ATLAS calorimetry volumes, as defined in the GEANT detector simulation.

the magnetic field. The weighting and the calibration are performed by optimizing the expression

$$\min_{w_i} \sum_{j}^{Events} (\sum_{i}^{Compart.} w_i E_{ij} - E_{true j})^2,$$

where compartments are sections of the calorimeter which behave in a similar way, or estimators of dead energy. For further details see Publication II.

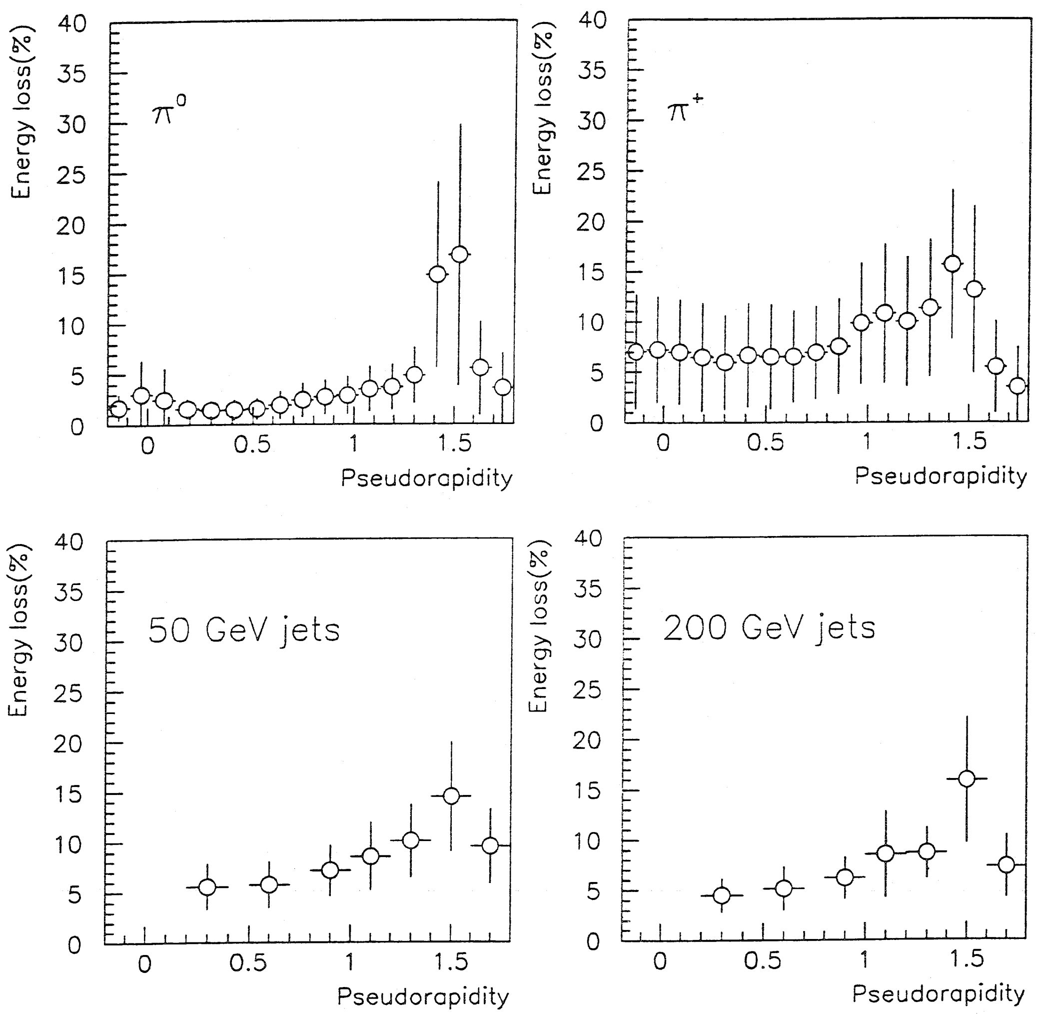

Figure 5.2: Energy lost in dead material. Jets are mostly a mixture of pions. The energy lost by π^0 is shown in the upper left figure and the one by π^+ in the upper right one. The vertical error bars represent the actual RMS of the distribution, not the error of the mean. One sees that the dead material is concentrated in a small window of about 0.2 in η at $|\eta|$=1.45. For charged pions, there are two components, the dead material in front of the calorimeter and the dead material between the EM and HAD calorimeters due to the outer cryostat wall. In the barrel there are larger fluctuations on the hadronic energy loss due to the fluctuation of the starting point of the hadronic shower.

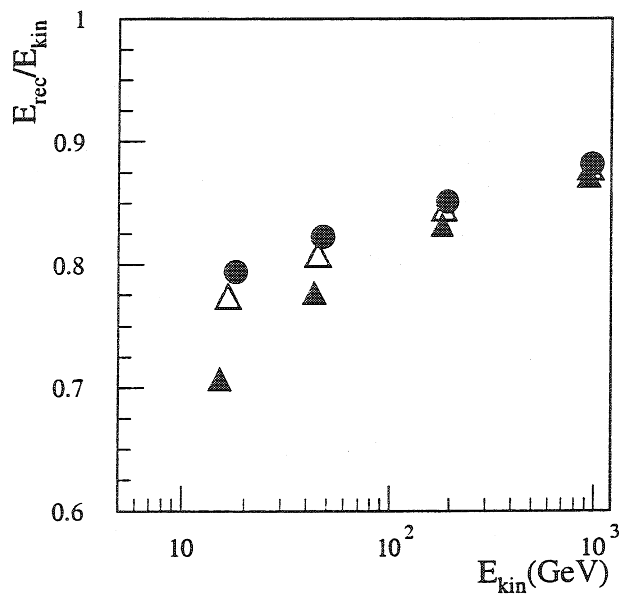

Figure 5.3: Mean relative reconstructed jet response using the EM calibration only at $|\eta| = 0.3$. R=0.4 (filled triangles), R=0.7 (open triangles) and R=1.5 (filled circles). For R=1.5 the response is close to the full calorimeter response, hence the non compensation and energy lost in dead material are the main contributions. For smaller cones like R=0.4, out-of-cone showers become important at low energies. The energy variable $E_{kin} = E_{true}$.

5.2 Jet energy resolution

The main result from the simulations is the jet energy resolution. This is to be compared to the requirements for jets which is

$$\frac{\sigma}{E} = \frac{50\%}{\sqrt{E}} \oplus 3\%.$$

Scans are made both in energy and in η. The resolution for fixed energies are shown in Figure 5.4. An energy parameterization of the resolution is shown in table 5.1 according to the expression

$$\frac{\sigma}{E} = \frac{a}{\sqrt{E}} \oplus b \oplus \frac{c}{E}$$

This study confirms previous results [49] and no alarming degradation is found due to the inclusion of more dead material in the updated geometry. Even with a very simple weighting procedure the performance conforms to the requirements. One should however be aware of the reduced energy resolution when using small cones in the crack region due the large fluctuations of energy lost in dead material.

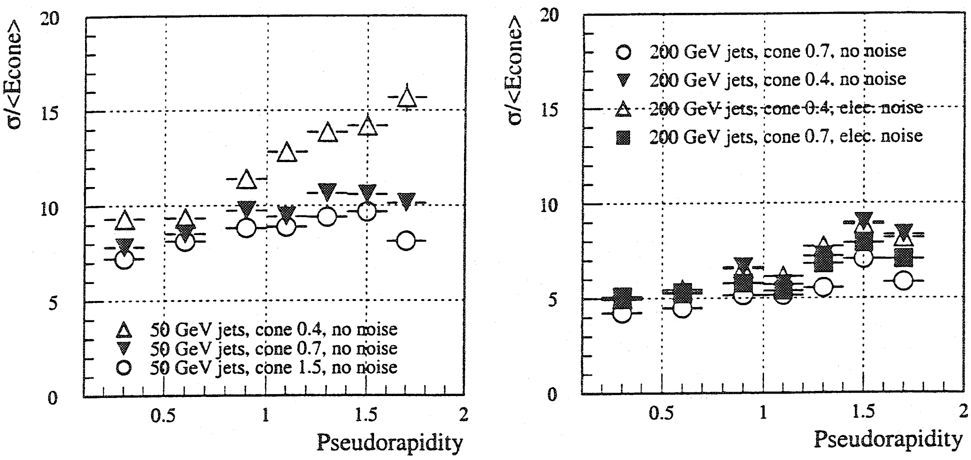

Figure 5.4: Energy resolution for 50 GeV and 200 GeV jets.

$Cone$	η	$a(\%GeV^{1/2})$	$b(\%)$	$c_{0\sigma}(GeV)$	$c_{2.5\sigma}(GeV)$
0.7	0.3	52.3±1.1	1.7±0.1	3.0±0.1	2.0±0.1
0.4	0.3	62.4±1.4	1.7±0.2	2.0±0.1 (pile-up 4.7±0.2)	1.7±0.2
1.5	0.3	48.2±0.9	1.8±0.1		
0.7	0.9	63.0±1.5	2.0±0.3	2.7±0.2	
0.4	0.9	74.7±2.1	2.7±0.5	1.9±0.3	
0.7	1.3	66.1±2.1	3.4±0.2	2.9±0.2	
0.4	1.3	82.3±2.6	4.0±0.3	2.0±0.3	

Table 5.1: Parameterization of the jet resolution. During the fit of the noise term, the a and b parameters are kept fixed. The c term is given for two different cell cuts, either at 0σ or 2.5σ of the noise.

6

Measurements of GMSB

6.1 Introduction

Much of the GMSB phenomenology applicable for the ATLAS detector has already been explored in a previous study [50]. This investigation takes a closer look at a few points in the parameter space of GMSB models where the the $\tilde{\tau}_1$ slepton is the next-to-lightest sparticle (NLSP). The lifetime of the NLSP depends on a free parameter. Two cases are investigated, either the NLSP decays close to the production vertex or outside of the detector. The lifetime is actually one of the most important handles on the model as is pointed out in [51]. However, lifetime measurements require detailed full simulation which is outside the scope of this study.

6.2 The model

The effective models of GMSB is a sub class of models within the framework of the Minimal Supersymmetric extension of the Standard Model (MSSM). Due to general arguments e.g. soft SUSY breaking (SSB) the number of parameters in MSSM are 124 in addition to the 19 in the SM. Much of the MSSM parameter space is highly unphysical including e.g. rapid proton decay and lepton number violation and hence so called R-parity conservation is added ad hoc. In order to understand the model some assumptions must be made concerning the origin of the SSB terms. One such assumption is GMSB. In GMSB the *observable sector* **O** containing the Standard Model fields communicates with a *messenger sector* M usually built up by GUT preserving gauge fields. M then mediates the SSB by overlapping with a rather unspecified *secluded sector* S

$$\mathbf{O} \leftarrow SU(5), SU(10).. \leftarrow \mathbf{M} \leftarrow X \leftarrow \mathbf{S}$$

This automatically generates small flavor violations and preserves Grand Unification. In the minimal version of GMSB (mGMSB) the model is fully determined by six parameters:

- $\Lambda_m = F_m/M_m$, the effective SUSY breaking scale. Here chosen to be 30 TeV.
- M_m, the messenger scale. The messenger scale it set to 250 TeV.
- N_5, the parameterization of the $SU(5)$ messenger fields. Here N_5 is set to 3.

- $\tan\beta$, the ratio of the Higgs vacuum expectation values at the electroweak scale.
- sgn μ, the sign of the Higgsino mass term. Here sgn $\mu = +1$
- C_{grav}, the gravitino mass scaling factor.

All GMSB events are generated by the GMSB implementation in ISAJET 7.48 [52]. The major theoretical arguments at the moment against GMSB are the origin of the Higgs parameters μ and B see [16], which in mGMSB are assumed to be determined at the EW-scale, and the somewhat ad hoc use of gauge fields.

6.3 Phenomenology

6.3.1 The NLSP and the mass spectrum

The dominant SUSY production is through glue and quark interactions into gluino or squark pairs [53]. However, there is also an interesting contribution from prompt neutralino, chargino and slepton production [54]. Due to the imposed R-parity the sparticles will be pair produced and decay down to the LSP. The LSP in mGMSB models is a very light gravitino for any relevant value of the fundamental SSB scale $F \sim C_{grav}F_m$

$$m_{\tilde{G}} = \frac{F}{\sqrt{3}M_P} \leq 1\text{keV},$$

where M_P is the reduced Planck mass. This is expected since the model is constructed to keep flavor violations small and hence gravitational effects must be suppressed. The upper bound on $m_{\tilde{G}}$ actually comes from cosmology [16]. For most of the parameter space the NLSP is either a $\tilde{\chi}_1^0$, co-NLSP $\tilde{l}_R$, a $\tilde{\tau}_1$ or $\tilde{\chi}_1^0$ and $\tilde{\tau}_1$ co-NLSP. In a very small corner of parameter space $\tilde{\nu}$ NLSP is also possible. An inverted case with the $\tilde{g}$ as NLSP happens when M_m is very very large. For the parameters in this investigation the NLSP is either $\tilde{\tau}_1$ (G3) or co-NLSP $\tilde{l}_R$ (G2), see Table 6.1. The models G2a and G2b were investigated in [50].

Point	Λ_m (TeV)	M_m (TeV)	N_5	$\tan\beta$	sgn μ	C_{grav}
G2a	30	250	3	5	+	1
G2b	30	250	3	5	+	5000
G3a	30	250	3	12	+	1
G3b	30	250	3	12	+	5000

Table 6.1: The GMSB model parameters. For the long lived NLSP case the decay is disabled via the ISAJET option NOGRAV.

The sleptons are co-NLSP in this case and decay close to vertex for $C_{grav} = 1$ or outside the detector when the gravitino mass is rescaled. As $\tan\beta$ is increased the $\tilde{\tau}_1$ becomes the NLSP due to mixing effects proportional to m_τ. The other SUSY mass differences due to the shift in $\tan\beta$ appears to be of less phenomenological importance (see Table 6.2). The connection between the model parameters and the physical mass spectrum is according to [16] at leading order proportional to $N_5\Lambda_m$ for the gaugino masses, and $\sqrt{N_5}\Lambda_m$ for the slepton masses. There is also an overall logarithmic dependence on M_m due to the boundary conditions for the RGEs.

Particle	G2	G3	Particle	G2	G3	Particle	G2	G3
$\tilde{g}$	699	699						
$\tilde{u}_L$	658	658	$\tilde{u}_R$	635	635	$\tilde{\chi}_1^0$	113.9	115.5
$\tilde{d}_L$	662	662	$\tilde{d}_R$	634	634	$\tilde{\chi}_2^0$	196.2	196.1
$\tilde{t}_2$	674	672	$\tilde{t}_1$	577	582	$\tilde{\chi}_3^0$	277	265
$\tilde{b}_2$	640	644	$\tilde{b}_1$	631	626	$\tilde{\chi}_4^0$	329.9	316.5
$\tilde{e}_L$	204.1	204.5	$\tilde{e}_R$	102.7	103.3	$\tilde{\chi}_1^\pm$	191.8	193.0
$\tilde{\tau}_2$	204	207	$\tilde{\tau}_1$	101.6	97.4	$\tilde{\chi}_2^\pm$	328	316
$\tilde{\nu}$	189	188	$\tilde{\nu}_\tau$	189	188			
h^0	106	111	H^0	337	311			
A^0	334	311	$H^\pm$	344	321			

Table 6.2: Masses in GeV as $\tan\beta$ is increased from 5 to 12. Note that $\tilde{e}$ and $\tilde{\mu}$ are degenerate.

6.3.2 Topology

Typical signatures at the end of the decay chain for the G2 and G3 models are

G2

$$\begin{array}{llll} \tilde{\chi}_1^0 & \rightarrow & \tilde{\mu}_R^\pm & \mu^\mp \\ & & | & \\ & & \rightarrow \tilde{G} & \mu^\pm \end{array}$$

G3

$$\begin{array}{lllll} \tilde{\chi}_1^0 & \rightarrow & \tilde{\mu}_R^\pm & \mu^\mp & \\ & & | & & \\ & & \rightarrow \tilde{\tau}_1 & \mu^\pm & (\tau) \\ & & \quad | & & \\ & & \quad \rightarrow \tilde{G} & \tau & \end{array}$$

Due to the $\tilde{G}$ all GMSB scenarios produce missing E_T. One exception is when the NLSP is quasi-stable, charged, reconstructed and included in the E_T calculation. In this study the quasi-stable NLSP is included. If the NLSP is charged and quasi-stable its mass and momentum can be fully reconstructed in the muon system and the background in that environment is not an issue.

The signature for the G3 models unconditionally involves τ which makes the detection more challenging compared to the G2 case. The decay mode at the end of the decay chain is either of the type

$$\tilde{\mu}_R^\pm(\tilde{e}_R^\pm) \rightarrow \tilde{\tau}_1 + \mu^\pm(e^\pm) + \tau \tag{6.1}$$

when the $\tilde{\tau}_1$ decays outside the detector, or if the $\tilde{\tau}_1$ lifetime is very short

$$\tilde{\tau}_1^\pm \rightarrow \tau^\pm + \tilde{G} \tag{6.2}$$

Due to the limited phase-space in the decay (6.1), the τ lepton is undetectable.

A very large fraction of the events contains the decay

$$\tilde{\chi}^0 \to \tilde{\mu}_R^{\pm}(\tilde{e}_R^{\pm}) + \mu^{\mp}(e^{\mp}) \tag{6.3}$$

which provides a very clear same flavor opposite charge (SOC) dilepton signal. The SOC results is sharp mass edges (see appendix A in Publication III) and also removes most of the light QCD background. By forming the flavor combination

$$\mu^+\mu^- + e^+e^- - \mu^{\pm}e^{\mp} \tag{6.4}$$

a lot of the combinatorial background can be subtracted.

A standard handle on the SUSY signals is M_{eff}. M_{eff} is defined as

$$M_{\text{eff}} = \max_{|\vec{p}_{T_{\text{jet},i}}|} \sum_i^4 |\vec{p}_{T_{\text{jet},i}}| + E_{T_{\text{miss}}}$$

This is very useful since squarks and gluionos generate a lot of hard jets. For prompt $\tilde{\chi}^0$, $\tilde{\chi}^{\pm}$ and $\tilde{l}$ production this is not the case, and one has to rely on $E_{T_{\text{miss}}}$ and e.g. a lepton sinature.

6.3.3 From mass measurements to model parameters

In the same way as parameters in the SM can be extracted from various precision observables, parameters in an underlying SUSY model can be estimated. Following the approach outlined in [50] the SUSY masses are here used to fit the most probable model parameters. If sgn μ and C_{grav} are held fixed there are four independent parameters. Hence, in absence of degeneracy four independent masses should be enough to pinpoint the model. The light higgs mass m_h is assumed to be measured independently within ± 3 GeV. The minimum set of masses are a squark or gluino mass, the $\tilde{\chi}_1^0$ and $\tilde{\chi}_2^0$ masses* and a slepton mass. Conceptually the situation looks like

$$M_i(p_j) \to m_i \to m_i^* \tag{6.5}$$

where $M_i(p_j)$ are the masses of the model parameters p_j. m_i^* represents the masses after the smearing of the detector. To find the inverse mapping back to p_j a fit is made using the known errors

$$\chi^2 = \sum_1 \frac{(M(p_j) - m_i^*)^2}{\sigma_i^2} \tag{6.6}$$

6.4 Experimental setup

6.4.1 Production

SUSY Signal and integrated luminosity

The total cross-section for SUSY production in the G3 models is 17 pb. Assuming the LHC low luminosity of 10^{33} cm^{-2}s^{-1}, one year yields a total integrated luminosity of 30 fb^{-1}.

*Looking at the mass relations [16] they turn out not be closely related.

Let us say that 10 fb^{-1} will be available, then 170000 SUSY events should be simulated for correct statistical fluctuations. Here all SUSY models use 170000 signal events to represent one year of low luminosity.

Of the total signal 10% is due to prompt gaugino and slepton production. Since the jet multiplicity for prompt production is much lower than for the strong production, a jet veto enables very effective selection of this type of events. Prompt production can e.g. be interesting in an exclusive cross-section analysis.

Standard model background

For model G3b the SM background is not an issue due to the presence of heavy charged particles. However, since the signature in G3a contains SM particles only, the SM background is significant. The Monte Carlo cross-sections for the main SM contributions are listed in Table 6.3. Only backgrounds with potentially large Ptmiss and dilepton signals have been evaluated. All background events are simulated by PYTHIA [55]. Examples of background compared to signal are shown in Figure 6.1. The number of plotted events are always rescaled to 10 fb^{-1} and hence the statistical fluctuations are equal or larger than expected.

Channel	σ[pb]	Events prod.	Events simu.
$t\bar{t}$	580 (833 [56])	5.8M	400k
Wj($p_T > 20$ GeV)	35000	350M	200k
Zj($p_T > 20$ GeV)	580	5.8M	200k
WW,WZ,ZZ	65	650k	200k
QCD($p_T > 50$ GeV)	$23 \cdot 10^6$	$2.3 \cdot 10^{11}$	300k
$b\bar{b}$($p_T > 50$ GeV)	88000	880M	300k

Table 6.3: SM backgrounds used in the simulations. All Z are Z $\rightarrow \tau^+\tau^-$. A separate sample of $b\bar{b}$ is included since it produces potentially dangerous dimuon signals at the 1.2% level.

6.4.2 Trigger

The signal has a fairly high probability to pass the trigger due to the presence of very high P_T jets, see e.g. the leading jet variable in Figure 6.1. The results given by ATLFAST for the standard trigger menu options XE50+J50 and J180 are shown in Table 6.4. XE50 represents missing E_T above 50 GeV, and J180 represents jets above 180 GeV. For prompt production in G3a, the trigger criteria τ20+XE30 combined with a jet veto was investigated. The acceptance for prompt production with this trigger was found to be 9%.

6.4.3 Detection

Ordinary particles

The response of the ATLAS detector is simulated by fast parameterizations using the ATLFAST package [57]. The default settings are used. That is, the acceptance is limited to

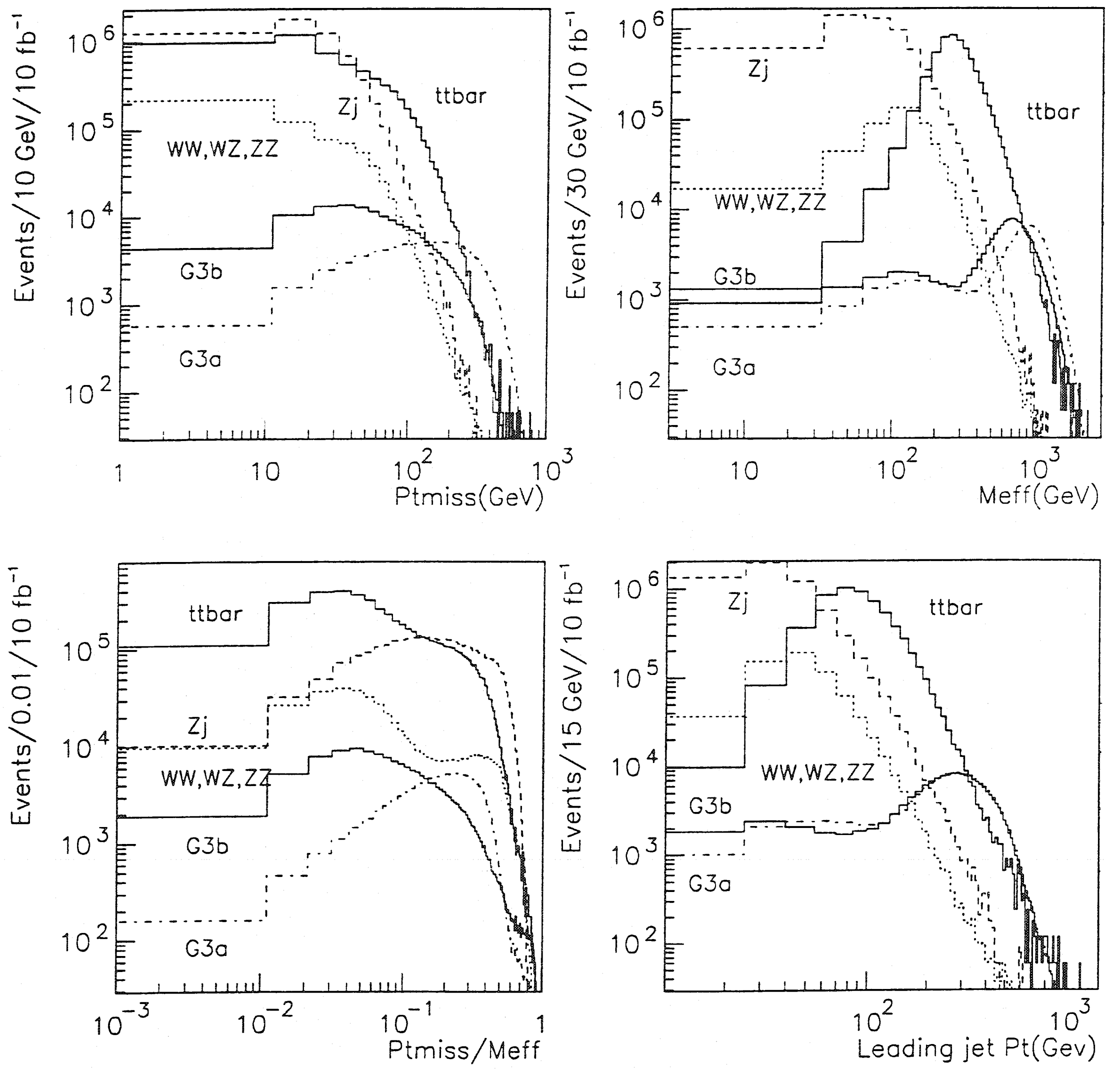

Figure 6.1: Variables that can be used to control the SM background. The signal is also included in the plots for comparison. It is quite obvious that $t\bar{t}$ is the most dangerous background. Meff is defined as the scalar sum of the four leading jets plus Ptmiss. The number of events shown in the plot are events reconstructed in the detector, but without trigger efficiencies.

Channel	XE50+J50[%]	J180[%]
G3a	92	83
G3b	62	87 (0.015 Hz)
$t\bar{t}$	31	7.3 (0.04 Hz)
Wj($p_T > 20$ GeV)	4.0	0.7
Zj($p_T > 20$ GeV)	6.0	0.6
WW,WZ,ZZ	10	1.3
QCD($p_T > 50$ GeV)	0.05	0.5 (100 Hz)
$b\bar{b}(p_T > 50$ GeV)	0.7	0.6

Table 6.4: Fraction of the events that pass the trigger criteria. The results are from ATLFAST. The equivalent trigger rates are shown within parentheses. No efficiencies are included. Note that the true trigger rates are higher since no pile-up is included in the simulation, at least a factor of five is expected e.g. for the XE50 trigger. The estimates for the high P_T trigger should however be more reliable.

$|\eta| < 2.5$, and reliable results should be expected for ordinary particles since the E_T thresholds are conservative: $\gamma > 5$ GeV, $e^{\pm} > 5$ GeV and $\mu^{\pm} > 6$ GeV. Jets are reconstructed with an R=0.4 cone after binning and smearing the fragmented generator particles according to the calorimeter performance. The jet threshold is $P_T > 15$ GeV. The μ and e reconstruction efficiency is assumed to be 100%. However, in the ATLFAST trigger simulation parameterized muon efficiencies are applied.

Tau particles

The tau particles are reconstructed by the hadronic decay modes using standard ATLFAST tau jet isolation criteria. The efficiency and jet rejection are parameterized using the result from a separate tau study [58] where full simulation of both calorimeter isolation and inner tracker constraints are used. The parameterization is p_T dependent. E.g. at $p_T = 15 \div 30$ GeV a 60% efficiency gives a jet rejection of 10. Here the tau efficiency is fixed to 60%. The efficiency for the reconstruction of the charge when needed is 92% taken from [59].

Quasi-stable charged sleptons

The detection of the quasi-stable $\tilde{\tau}_1$ is parameterized using the results in [60] and is implemented into ATLFAST. Effects of the sagitta measurement, multiple scattering and energy loss fluctuations are taken into account. For a mass measurement ($m_{\tilde{\tau}_1} = p/(\beta\gamma)$) β is limited to $0.8 < \beta < 0.91$, see Figure 6.2. At $\beta = 0.85$ the β measurement contribution to the resolution is 10% and the momentum contribution 3%, the two terms are independent. The lower bound on β comes from the time window in the trigger chambers needed for the second coordinate and the upper bound from TOF. Thus $m_{\tilde{\tau}_1}$ can be measured down to the level of the estimated 0.1% systematic effects due to 60k of $\tilde{\tau}_1$ given 10 fb^{-1}. Once $m_{\tilde{\tau}_1}$ is constrained the upper bound on β can be relaxed. 90% reconstruction efficiency is assumed within the acceptance.

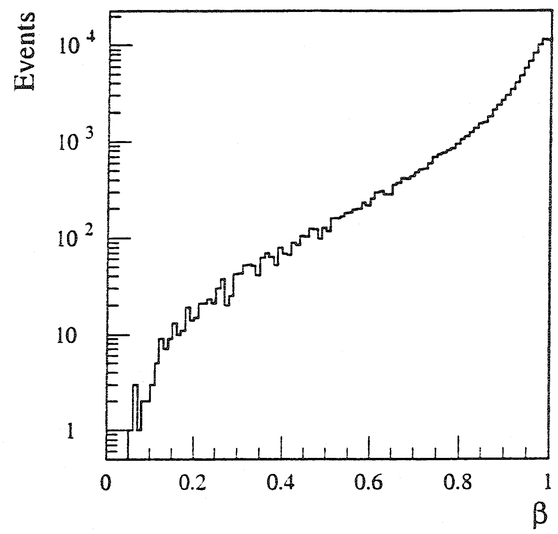

Figure 6.2: Velocity distribution for $\tilde{\tau}_1$.

6.5 Model G3b

In this model the $\tilde{\tau}_1$ is a quasi-stable NLSP and it decays outside of the detector. The golden event signature is a very heavy charged particle in the muon system. Virtually no standard model background is present. As described in the previous section, the $\tilde{\tau}_1$ mass is measured independently in the muon system. This enables the momentum resolution to be vastly improved by a mass constraint. Since everything in the decay chain $\chi^0_{1,2} \to l^+\tilde{l}^-_R \to l^+l^-\tilde{\tau}_1(\tau)$ is measurable except for the very soft τ, the effective mass reconstruction is almost trivial. Examples of reconstructed masses are shown in Figure 6.3 and 6.4. The $\tilde{l}_R$ mass is found from the edge in the invariant mass $M_{\tilde{\tau}_1 l}$ distribution, see the left plot in Figure 6.3. The $\chi^0_{1,2}$ masses can either be found directly from $M_{\tilde{l}^-_R l^+}$, or indirectly from $M_{l^+l^-}$, see right plot in Figure 6.4. For an introduction to effective invariant masses see appendix A in Publication III. Edges are expected at

$$M_{ll}^{max} = M_{\tilde{\chi}^0_1}\sqrt{1-\frac{M^2_{\tilde{l}_R}}{M^2_{\tilde{\chi}^0_1}}}\sqrt{1-\frac{(M_{\tilde{\tau}_1}+M_\tau)^2}{M^2_{\tilde{l}_R}}} = 14.5 \text{ GeV } (14.3\pm0.05 \text{ GeV}), \tag{6.7}$$

and at

$$M_{ll}^{max} = M_{\tilde{\chi}^0_2}\sqrt{1-\frac{M^2_{\tilde{l}_R}}{M^2_{\tilde{\chi}^0_2}}}\sqrt{1-\frac{(M_{\tilde{\tau}_1}+M_\tau)^2}{M^2_{\tilde{l}_R}}} = 46.8 \text{ GeV } (46.7\pm0.05 \text{ GeV}). \tag{6.8}$$

All dilepton figures are improved by the flavor subtraction $\mu^+\mu^- + e^+e^- - \mu^\pm e^\mp$. The $\tilde{q}_{L,R}$ masses can be extracted from edges in the invariant mass spectrum M_{llj}. The dominant decay is $\tilde{q}_R \to \chi^0_1 q$, see the left plot in Figure 6.5. The events are selected by requiring $M_{ll} < 15$ GeV, $P_{Tll} > 65$ GeV, 2 jets with $P_T > 25$ GeV and 2 jets with $P_T > 50$ GeV. The right plot in Figure 6.5 also shows the spectrum M_{llj}, but with 15 GeV $< M_{ll} <$ 46 GeV.

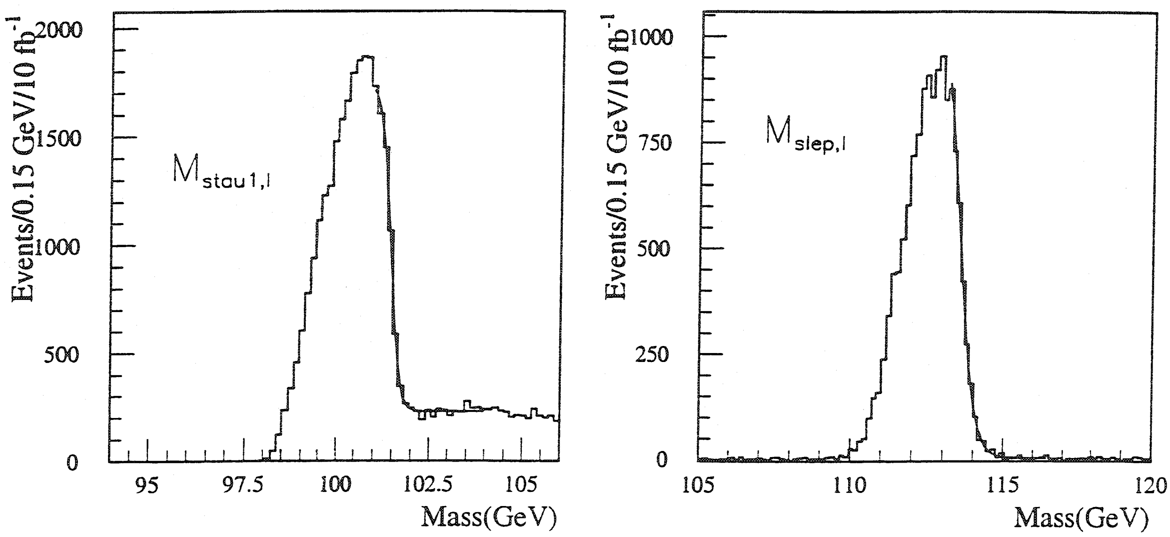

Figure 6.3: Minimal invariant mass distribution (left) for a stau and a lepton ($M_{\tilde{\tau}_1 l}$). The $\tilde{l}_R$ mass is extracted from the edge in the three-body decay. The fitted function is a first order polynomial times a sigmoid plus a constant background. The fit yields: $M_{\tilde{l}_R} = M_{\tilde{\tau}_1 l} + M_\tau = 103.3 \pm 0.05$ GeV. The right plot shows the spectrum of $M_{\tilde{l}^{+}_{R} l^{-}}$. Same type of fit as in the left plot is used. The result from the fit is: $M_{\tilde{\chi}^0_1} = M_{\tilde{l}_R l} + M_\tau = 115.3 \pm 0.1$ GeV.

The dominant decay is $\tilde{q}_L \to \chi^0_2 q$. The expected edges are

$$M_{llj}^{max} = M_{\tilde{q}R}\sqrt{1 - \frac{M^2_{\tilde{\chi}^0_1}}{M^2_{\tilde{q}_R}}}\sqrt{1 - \frac{(M_{\tilde{\tau}_1} + M_\tau)^2}{M^2_{\tilde{\chi}^0_1}}} = 320 \text{ GeV } (316 \pm 3 \text{ GeV}), \tag{6.9}$$

and

$$M_{llj}^{max} = M_{\tilde{q}_L}\sqrt{1 - \frac{M^2_{\tilde{\chi}^0_2}}{M^2_{\tilde{q}_L}}}\sqrt{1 - \frac{(M_{\tilde{\tau}_1} + M_\tau)^2}{M^2_{\tilde{\chi}^0_2}}} = 546 \text{ GeV } (539 \pm 5 \text{ GeV}). \tag{6.10}$$

The masses within parenthesis are from the fit. The errors are errors from the fit generously rounded upwards. The estimation is based on values taken from several fits within different regions and different sets of data. Errors from absolute energy scale calibrations are not included. Given the six mass measurements, it is easy to solve for the six masses.

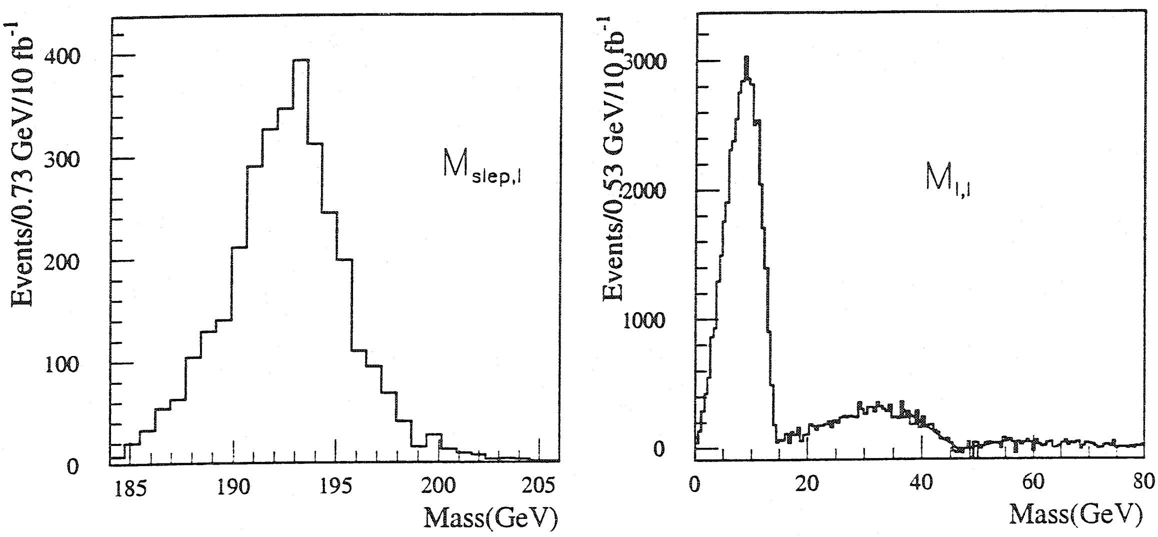

Figure 6.4: Minimal invariant mass (left) for a slepton and a lepton. The resolution for $M_{\tilde{\chi}_2^0}$ in the left plot is not very good. A better choice is to use the second edge in the dilepton invariant mass (M_{ll}) instead. The result from the fit is: $M_{ll} = 46.7 \pm 0.05$ GeV.

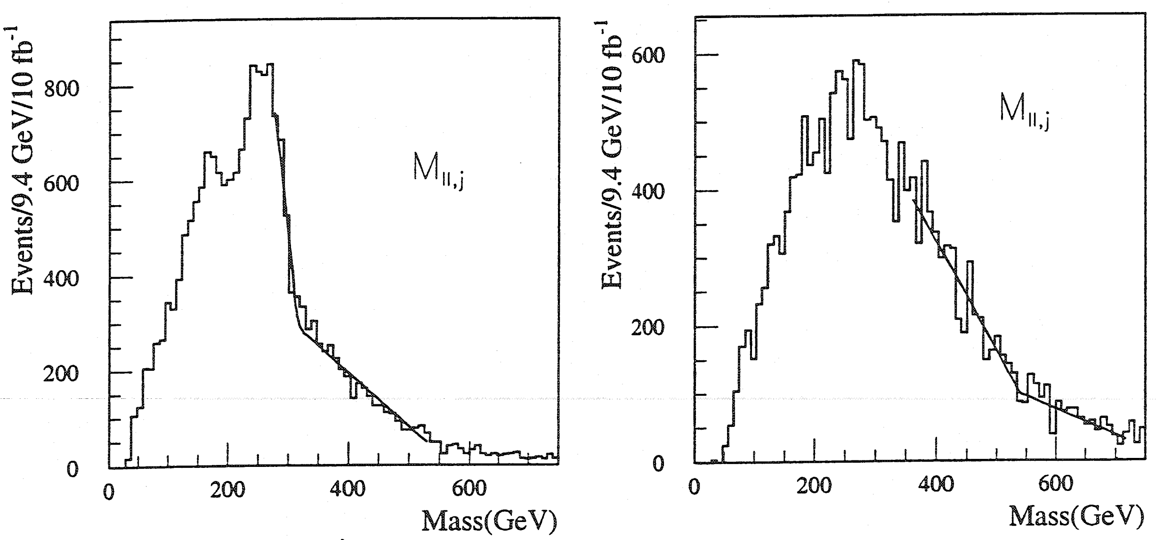

Figure 6.5: Invariant mass for a dilepton pair and a jet. The left plot shows M_{llj} for M_{ll} with a $P_T < 15$ GeV. The decay is dominated by $\tilde{q}_R \to \chi_1^0 q$. The right plots shows M_{llj} for M_{ll} with a $15 < P_T < 46$ GeV. This cut enhances the decay $\tilde{q}_L \to \chi_2^0 q$.

6.6 Model G3a

In the G3a model the NLSP is assumed to decay close to the vertex. As a result, no SUSY particle is directly detectable. However, a large amount of missing transverse energy is generated due to the LSP. In order to reject the SM background the following cuts have been applied:

- 4 jets with $P_T > 25$ GeV, jets identified as τ-jets are not included.
- At least one pair of same flavor opposite signed leptons.
- $M_{eff} > 300$ GeV.
- $E_{T_{miss}}/M_{eff} > 0.1$.

At the end of the decay chain we find a very hard tau. The most efficient reconstruction of the tau turns out to be via the hadronic decay modes. Hence only taus decaying into hadrons are used.

The decay chain is the same as in G3b, but with the difference that the $\tilde{\tau}_1$ now decays into $\tilde{\tau}_1 \to \tilde{G}\tau$. The complete investigated decay chain looks like $\tilde{q}_R \to \tilde{\chi}^0_{1,2} q \to \tilde{l}^-_R l^+ q \to \tilde{\tau}_1(\tau) l^- l^+ q \to \tilde{G}\tau(\tau) l^- l^+ q$. The (τ) is not detectable in the calorimeter due to the limited available phase-space. The lepton from the $\tilde{l}_R$-decay is very soft but detectable. The average P_T is 10 GeV, and a cut is made above 15 Gev to select these leptons. The p_T of the tau is required to be larger than 75 GeV. The invariant mass $M_{\tau l}$ is shown in Figure 6.6. Edges are expected at

$$M_{\tau l}^{max} = \sqrt{M^2_{\tilde{l}_R} - (M_{\tilde{\tau}_1} + M_\tau)^2} = 29.0 \text{ GeV } (28.4 \pm 1 \text{ GeV}). \tag{6.11}$$

and

$$M_{\tau l}^{max} = \sqrt{M^2_{\tilde{\chi}^0_1} - M^2_{\tilde{l}_R}} = 51.7 \text{ GeV } (44 \pm 5 \text{ GeV}). \tag{6.12}$$

The first edge in the plots in Figure 6.6 is not very much affected by the SM background. However, the second edge is more sensitive. Since the statistics is too low, e.g. a factor 10 for $t\bar{t}$, the fluctuations are too large to represent the real background. Real statistics should improve the situation in the left plot. In the right plot the background is more complicated. The background under the signal looks similar to the signal and causes a systematic shift of the edge. Special cuts to reduce the $t\bar{t}$ background may improve the situation. The background in the jet plots is almost negligible. The edges for M_{ll} and M_{llj} are the same as in G3b. The results from the fits are

$$M_{ll}^{max} = 14.5 \text{ GeV } (14.3 \pm 0.1 \text{ GeV}),$$

$$M_{ll}^{max} = 46.8 \text{ GeV } (57 \pm 1 \text{ GeV}),$$

and

$$M_{llj}^{max} = 320 \text{ GeV } (313 \pm 6 \text{ GeV}),$$

$$M_{llj}^{max} = 546 \text{ GeV } (530 \pm 5 \text{ GeV}),$$

The measured endpoint is systematically lower in many cases. This is expected to some extent since taus and jets leak out of the cone. The tau also has an unmeasured neutrino.

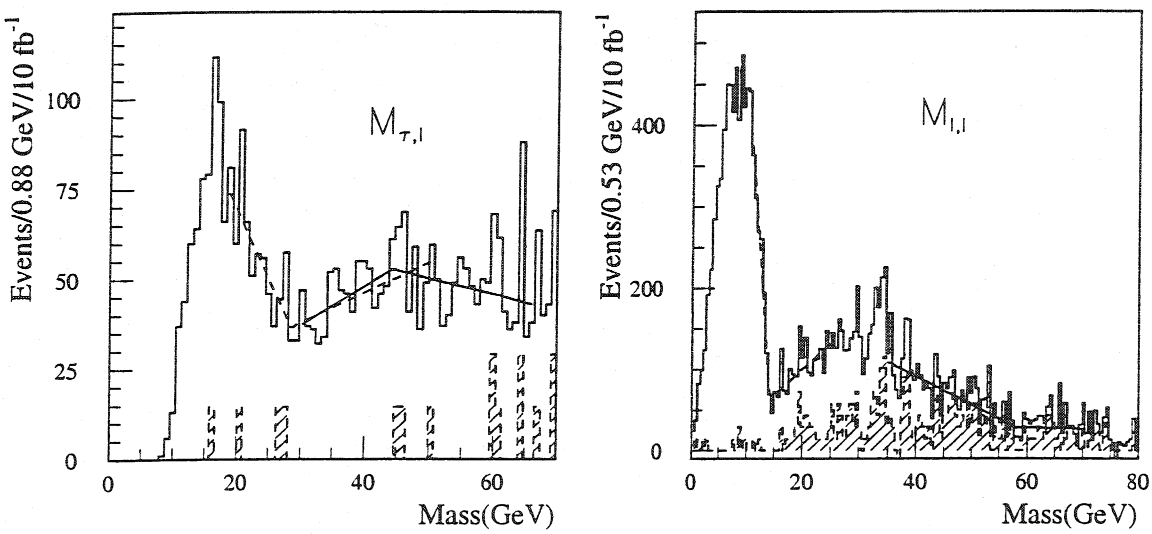

Figure 6.6: The invariant mass for a hard tau and a very soft lepton (left). The fluctuations of the background is large since the statistics does not represent the real expected background. The right plot shows the distribution of M_{ll}. The second edge is systematically shifted due to the shape of the background.

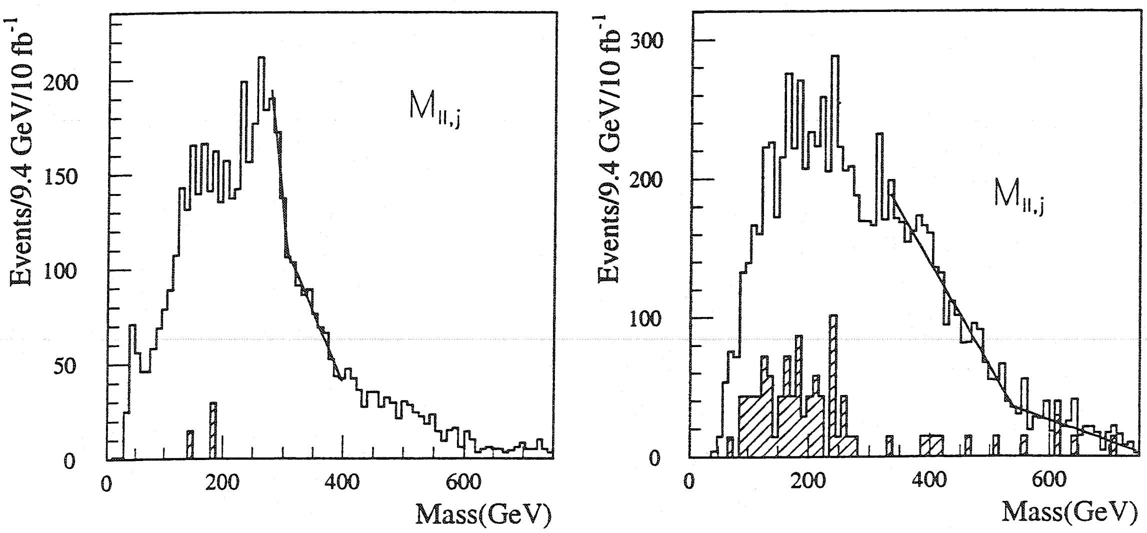

Figure 6.7: The same M_{llj} distributions as in G3b, but for G3a and with SM background included. The background is negligible under the fitted region.

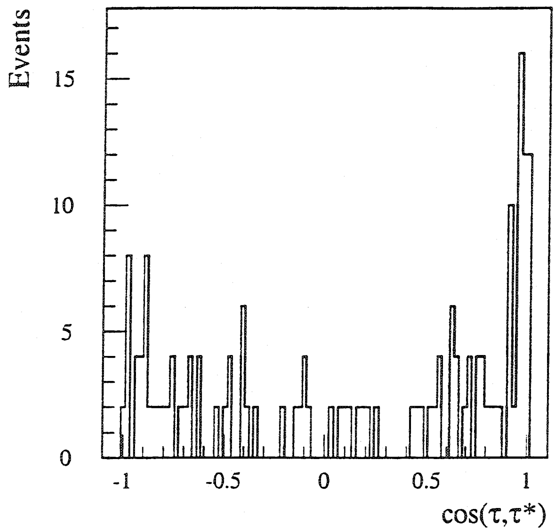

Figure 6.8: The plot shows $\cos\theta$ for the opening angle θ between the true tau momentum vector $\vec{\tau}$ and the tau momentum vector $\vec{\tau}^*$ estimated from a mass constrained decay chain.

6.7 Proof of the NSLP flavor

In the G3b model one cannot prove the flavor of the NLSP unless the soft tau is found. Since the P_T is so low it cannot be detected in the calorimeter. However, apart from the soft tau everything else is measureble. Thus, after measuring three masses, the tau momentum can be solved by imposing the mass constraints, see appendix B in Publication III for details.

Three masses and four 4-vectors are needed. These are taken from the well measured decay: $\tilde{l}_L \to \chi_1^0 l \to \tilde{l}_R^- l^+ l \to \tilde{\tau}_1(\tau) l^- l^+ l$. The opening angle between the true $\vec{\tau}$ vector and the mass constrained estimation $\vec{\tau}^*$ is shown in Figure 6.8. Perfect masses are assumed. The vector $\vec{\tau}$ could e.g. be replaced with tau vertex candidates from the inner tracker and a correlation of the type seen in Figure 6.8 would constitute a definite proof of the NLSP flavor.

7

Conclusions

The fast readout electronics for the Tile calorimeter has been evaluated under test-beam conditions. The original concept of non linear compression was found to be less competitive than the bigain compression concept and a choice was made to go for bigain compression in the final production. A 10 bits ADC was found to be the optimal solution, given the constraints set by performance, complexity and cost. This was also tested and evaluated in a close to final in drawer Digitizer.

Jets in the ATLAS barrel calorimeter have been measured by using full simulations of the detector and Monte Carlo generated light quark dijet events. The result was included in the ATLAS Detector and Physics Performance Technical Design Report. The results confirm the good jet energy resolution found in previous studies using older geometries.

The signals from GMSB models with $\tilde{\tau}_1$ as the NLSP have been investigated. Both the case with a quasi-stable NSLP (G3b), and the case with a NLSP decaying close to the vertex (G3b). The G3b model can be fully reconstructed with good mass resolution similar to related models studied previously [50]. The G3a model is harder than G3b from an experimental point of view due to the fact that the decay chain reconstruction is based on tau leptons in the final state. However, also in this case can masses of sleptons, neutralinos and squarks be determined with surprising precision, and nothing prevents a reasonable estimation of the model parameters from the measured masses.

Acknowledgements

First of all I want to thank Kerstin Jon-And for encouraging me to join the Stockholm ATLAS group and to take part in the effort to build the Tile calorimeter, and for always supporting me and keeping the mood high. I have felt great support and received good advice from Sven-Olof Holmgren whenever needed. Sten Hellman has also been one of my advisors and has help me numerous times concerning hadron physics and in proof reading this thesis.

I also want to give acknowledgement to Björn Sellden for providing part of the analysis and the plots concerning 1996 test-beam data. At CERN I want thank Martine Bosman for helping me with the jet reconstruction and sharing her deep knowledge concerning jets and full detector simulations. Ilias Efthymiopoulos was also helpful during my very first year at CERN. Thanks to Ian Hinchliffe for letting me stay at Berkeley Labs and for maintaining an impossible good mood and always answering all of my questions within a blink of an eye. Thanks also to Giacomo Polesello and Frank Paige for answers to my questions concerning SUSY.

At last I want thank Lena Leinonen for being a very good friend and making all day to day office hours less tedious.

Bibliography

[1] ATLAS Detector and Physics Performance TDR, CERN/LHCC/99-14.

[2] For a historical overview and pedestrian introduction see: S.F. Novaes, *Standard Model: An Introduction*, hep-ph/0001283

[3] D.G. Charlton, *Precise Electroweak Results from LEP2*, hep-ex/9912019.

[4] Chris Quigg, *The State of the Standard Model*, hep-ph/0001145.

[5] D.P. Roy, *Higgs and SUSY Searches at LHC*, hep-ph/9803421.

[6] R. N. Mohapatra, *Supersymmetric Grand Unification: Un update*, hep-ph/9911272.

[7] S. Dimopoulus, H. Georgi, *Nucl. Phys.* **B 193**, 150 (1981).

[8] W. Hollik, Plenary talk at the 29th International Conference on High-Energy Physics (ICHEP 98), Vancover, Canada, July 23-30, 1998.

[9] M. Carena et al, *MSSM Higgs Boson Phenomenology at the Tevatron Collider*, hep-ph/9808312.

[10] A. Golfand and E. P. Likhtman, *JETP Lett.* **13**, 323 (1971).

[11] E. P. Likhtman, Supersymmetric Renomalizable Theory of Massive Vector Non-Abelian Field, *JETP Lett.*, **22**, 57 (1975).

[12] L. Haag, J. Lopuszanski and M. Sohnius, Nucl. Phys. **B88**, 257 (1975).

[13] H.P. Nilles, *Phys. Rep.* **110**, 1 (1984).

[14] M. Dine, W. Fishler, *Phys. lett. B*, **110**, 227 (1982).

[15] M. Dine, A. E. Nelson, *Phys. Rev. D* **48**, 1277 (1993).

[16] G.F. Giudice, R. Rattazzi, Theories with Gauge-Mediated Supersymmetry Breaking, hep-ph/9801271.

[17] L. Randall, R. Sundrum, hep-th/9810155.

[18] R. Wigmans, *On the energy resolution of uranium and other hadron calorimeters*, Nucl. Instrum. Methods **A259** (1987) 389-429.

[19] R. Wigmans, *High resolution calorimetry*, Nucl. Instrum. Methods **A265** (1988) 273-290.

[20] C. W. Fabian and T. Ludlam, Ann. Rev. Nucl. Part. Sci. **32** (1982) 335.

[21] J. Badier et al., *Test result of an electromagnetic calorimeter with 0.5 mm scintillating fibers readout*, Nucl. Instrum. Methods **A337** (1994) 314-325.

[22] E. Bernardi et al., *Performance of a compensating lead-scintillator hadronic calorimeter*, Nucl. Instrum. Methods **A262** (1987) 229-242.

[23] M.P.Casado and M. Cavalli-Sforza, H1-inspired analysis of the 1994 combined test of the Liquid Argon and Tilecal calorimeter prototypes, ATL-TILECAL-96-075 (1996).

[24] ATLAS Technical Proposal CERN/LHCC/94-43

[25] F. Ariztizabal et al., *Construction and Performance of an Iron-Scintillator Hadron Calorimeter with Longitudinal Tile Configuration*, Nucl. Instrum. Methods **A349** (1994) 384.

[26] ATLAS Tile Calorimeter TDR, CERN/LHCC/96-42.

[27] W.E. Cleland, E.G. Stern, *Signal processing considerations for liquid ionization calorimeters in a high rate environment*, Nucl. Instr. and Methods, **A 338** (1994) 467-497.

[28] Jim Pilcher, Private communications.

[29] FERMI collaboration, a digital Front End and Readout MIcrosystem for high resolution calorimetry, CERN/ATL-DAQ-94-015.

[30] TileMon user manual, http://atlasinfo.cern.ch /Atlas/SUB_DETECTORS/TILE/testbeam/tb1999/TestBeam_1999run.html

[31] ZEBRA, CERN Program Library Long Writeups Q100/Q101.

[32] FERMI collaboration, Results of the testbeams of RD16 (FERMI) With electromagnetic and hadronic calorimeter prototypes, CERN/ATL-DAQ-95-042.

[33] S. Angvall et al., Evaluation of Fermi Readout of the ATLAS Tilecal Prototype, CERN/ATL-TILECAL-97-116.

[34] S. Berglund et al., A Digitizer System for the Tile Calorimeter, CERN/ATL-TILECAL-97-132.

[35] Svante Berglund, Private communications.

[36] C. W. Cattaneo, A technique for signal shape reconstruction in sampled systems, FERMI note # 45, Submitted to Signal Processing.

[37] I. Efthymiopoulos and T. Kontos, Analysis of the CIS calibration data of the new Tile Calorimeter bi-gain readout system, ATLAS internal note, TILECAL-NO-143.

[38] K. Andersson et al., Front-end Electronics for the ATLAS Tile Calorimeter, Writeup from 1998 Rome LEB meeting.

[39] T. Davidek and R. Leitner, Parametrization of the Muon Response in the Tile Calorimeter, ATLAS internal note, ATL-TILECAL-97-114.

[40] S. D. Drell et al., Phys. Rev. **187** 2159 (1969).

[41] G. Hanson et al., Phys. Rev. Lett. **35** 1609 (1975).

[42] J. E. Huth et al, Proceesings of the Summer Study on High Energy Physics, Snowmass, Colorado, 1990, p. 134.

[43] G. Sterman and S. Weinberg, Phys. Rev. Lett. **39**, 1436 (1977)

[44] T. Sjöstrand, Comp. Phys. Commun. **28** 227 (1983).

[45] GEANT 3, ATLAS version 3216 98_2. DICE 3.20 geometry and digitization.

[46] M. Seymour, Zeit. Phys. **C62** 127 (1993).

[47] S.D. Ellis and D.E. Soper, Phys Rev. D. **48** 2160 (1993).

[48] T Akers et al., OPAL Collaboration, Z. Phys. **C63** 197 (1994).

[49] ATLAS Calorimeter performance, CERN/LHCC/96-40.

[50] I. Hinchliffe and F. Paige, Measurements in Gauge Mediated SUSY Breaking Models at LHC, ATL-PHYS-98-134 (1998).

[51] S. Ambrosanio, G. Blair, Precision GMSB at a Linear Collider, hep-ph/9907396.

[52] F. Paige, S. Protopopescu, ISAJET 7.44 A Monte Carlo Generator for pp, $\bar{p}p$ and e^+e^- Reactions. http://penguin.phy.bnl.gov/~paige/

[53] M. Krämer, Supersymmetric particle production at hadron colliders, hep-ph/9809259.

[54] W. Beenakker et. al., The production of charginos/neutralinos and sleptons at hadron colliders, hep-ph/9906298.

[55] T. Sjöstrand, PYTHIA 5.7 and JETSET 7.4, Computer Physics Common. **82**, 1994. Program version 6.136.

[56] R. Bonciani et al, NLL Resummation of the Heavy-Quark Hadroproduction Cross-Section, hep-ph/9801375.

[57] E. Richter-Was, D. Froidevaux, L. Poggioli, A Fast Simulation Package for ATLAS, ATL-COM-PHYS-98-011 (1998).

[58] D.Cavalli and S.Resconi, Tau-jet separation in ATLAS detector, ATL-PHYS-98-118.

[59] Y. Coadou et al, Identification of Hadronic Tau decays in ATLAS, ATL-PHYS-98-126.

[60] G. Polesello, A. Rimoldi, Reconstruction of quasi-stable charged sleptons in the ATLAS Muon Spectrometer, ATL-MUON-99-006 (1999).

Publication I

European Organisation for Nuclear Research

ATLAS Internal Note
TILECAL-NO-0xx
23 January 1997

Studies of internal resolution for 12 bit and 10 bit ADCs in the Tilecal readout electronics

Sven-Olof Holmgren and Jörgen Sjölin
Stockholm University

1 Introduction

Cost and power consumption suggest using 10 bit instead of 12 bit ADCs in the Tilecal readout electronics. Hence, the aim of this study is to estimate the consequences to the internal electronics resolution. The result will be a prediction of the measurable internal resolution, channel by channel, that one could expect in a new configuration with 10 bit electronics. However, the internal electronics resolution at the critical high gain saturation energy correlates with a "worst case" scenario for the calorimeter where all the energy is released in one channel (Since there are two channels per cell one could regard that as a safety margin of $\sqrt{2}$). Any distribution of the energy among the cells will only improve the resolution from electronics point of view since less energy is likely to be at the most critical values. This "worst case" is not explicitly physical, but serves as a safe upper limit of the expected impact on the overall performance since the electronics resolution is just one of many other effects: photo-electron statistics, e/h, fibre to fibre fluctuations, etc..

2 Simple analytical model

In a first attempt to estimate the impact of digital resolution a very basic model was used to enable simple calculations. The model is based on one peak sample, perfectly located in time and read out by a perfect ADC.

The LSB voltage assumes 1V full swing and the relative gains assume that the overall gain has been adjusted so that the low gain covers the entire energy range.

The resolution given in Table 1 is the resolution in the lower gain channel at the energy where the higher gain saturates. This is the worst case.

The last row in the table gives the expected intrinsic calorimeter resolution at the same saturation energy. This estimate is simply $47\%/\sqrt{E}$, i.e. neglecting the constant term which is the most conservative assumption one can make.

To get the effect of the digital resolution on a given sample one should add the intrinsic and the digital resolution in quadrature. If we do this for the above examples the resolution in the last column goes from 5.9% to 6.1%. In all the other places there is no deterioration of the intrinsic resolution.

All this assumes that the contribution from noise can be neglected at the ADC level. The maximum allowed noise indicated in the table is just the LSB divided by $\sqrt{12}$ at which limit the noise is the same as the RMS error of the sampling.

In reality the energy estimate in one channel is a combination (filter) of up to 7 consecutive samplings which reduce the contribution of the digital resolution since these add in quadrature. But here only one sample is used: the theoretical peak of the pulse. This again is a conservative estimate.

Each calorimeter cell is seen by two independent PMT channels. This reduces the contribution of the digital resolution to the resolution of the overall energy estimate by $\sqrt{2}$.

For the parameters that go in to the model se Table 1, and resulting Goggi plot Fig. 1.

There are interesting factors left out in this simple model, e.g.: noise and multi sample filters. In order to get closer to the real design, a simulation using real 12-bit data was used to estimate a 10-bit system. This simulation is presented in the next section.

3 Simulation based on real data

The base of this simulation is the charge injection (CIS) data taken during the September 1997 test-beam. These data were originally used for calibration of the 12 bit bigain electronics.

The simulation was done within the framework of the Tilemon program. For the 12 bit electronics the compression of the dynamic range was performed by the use of two separate channels with different gains. Since this study concerns with worst case, not averages, only the low gain channel was considered.

To remove the sampling phase dependence of the energy estimator and get closer to the real conditions in ATLAS a sum of 8 samples was used as an energy measure. The samples were equally weighted, that is, the filter was not optimised. However, it turns out to work good enough to reduce the phase dependence below the level of the overall noise.

With the proposed final 10 bit electronics there are two major changes that affect the resolution: the replacement of 12 bit ADCs with 10 bit ADCs and adjustments to ATLAS full range of 800pC (in 1997 data 640pC). A minor effect compensated for is the reduction of the dynamic range due to the pedestal (90 counts in 12 bit 1997 data and 15 counts assumed for the 10 bit simulated data). These effects are implemented in the following way:

$$ADC_{10} = C * round(\frac{ADC_{12}}{C})$$

where

$$C = \frac{4095 - 90}{1023 - 15} * \frac{800}{628}$$

and ADC_{10} are 10 bit simulated ADC samples and ADC_{12} are low gain raw data ADC samples.

An important issue that is left out of this study is that from experiance it is known that an X bit ADC does not behave exactly as X bit, but rather as $X - \epsilon$ bit. Simulating a 10 bit ADC by rounding a 12 bit ADC probably gets very close to an ideal 10 bit ADC. Reasonable would be to expect an ϵ between 0.5 to 1 bit. However, if this degradation mainly is due to noise in the ADC and this noise is lower than the maximum allowed noise (see Table 1), then it should not significantly alter the results of the present study.

4 Results

Critical points are the gain switching points. For a gain ratio of 64 between the channels in the 10+10 bit system this will happen at 15 GeV if the muon requirement is 15 MeV/count. For a 12+12 bit system the critical point will be at 62 GeV. These are to be compared to the intrinsic resolution of the calorimeter for hadrons which is 12% at 15 Gev and 5.9% at 62 Gev assuming $47\%/\sqrt{E}$ as the hadron calorimeter resolution.

In Figs. 2 and 3 are shown distributions of measured and simulated data. In Fig. 4 measured and simulated resolutions are compared to the detector resolution. Compared to the analytical model 10 bit data agrees much better then the 12 bit data. This is probably mainly due to the fact that a real 12 bit ADC rounded to 10 bit have close to 10 effective bit resolution , while the real 12 bit have 10-11 effective bit resolution. Note also that with the current filter, no improvement beyond one ideal peak sample is reached.

5 Conclusion

The internal resolution of a new 10 bit readout system is simulated and compared to the 12 bit readout used in Tilecal 1997 test-beam. The results could be seen as a "worst case". If so, the worst case effect ever to be induced by the 10 bit system for hadrons is a $2.3\% \oplus 12\% - 12\% = 0.2\%$ degradation in absolute percent compared to $0.4\% \oplus 5.9\% - 5.9\% = 0.01\%$ using a 12 bit system.

General assumption: for a flat probability distribution in one dimension the Standard Error (RMS) is $1/\sqrt{12}$ times the sampling pitch.

Under this assumption we investigate the contribution to the energy resolution from a single sampling and for different combinations of bi-gain or tri-gain bit-widths.

General parameters common to all options:

Quantity	value
Maximum energy/cal.cell	2 TeV
Maximum energy/PMT chnl	1 TeV
Max carge/PMT chnl	800 pC
LSB for highest gain	15 MeV
Muon energy /cal. cell	350 MeV
Muon energy/PMT chnl	175 MeV
# counts for muon in high gain	11

Options:

	12 + 12 bits		10 + 12 bits		10 + 10 bits		8 + 8 + 8 bits		
	hi	lo	hi	lo	hi	lo	hi	mi	lo
Range (bits)	12	12	10	12	10	10	8	8	8
Gain	16	1	16	1	64	1	256	16	1
Max charge (pC)	50	800	12	800	12	800	3	52	800
LSB (MeV)	15.25	244	15.25	244	15.25	977	15.25	256	3906
LSB (μV)	244	244	977	244	977	977	3906	3906	3906
Sat. (MeV)	62500	1 TeV	15625	1 TeV	15625	1 TeV	3906	62500	1 TeV
# cnts at prev Sat		255		63		15		15	15
Resolution at Sat		0.1%		0.45%		1.9%		1.9%	1.9%
Max allowed noise (μV)		70		70		282		1000	1000
Intrinsic cal res at Sat		5.9%		12%		12%		24%	5.9%

Table 1: Analytical model configurations.

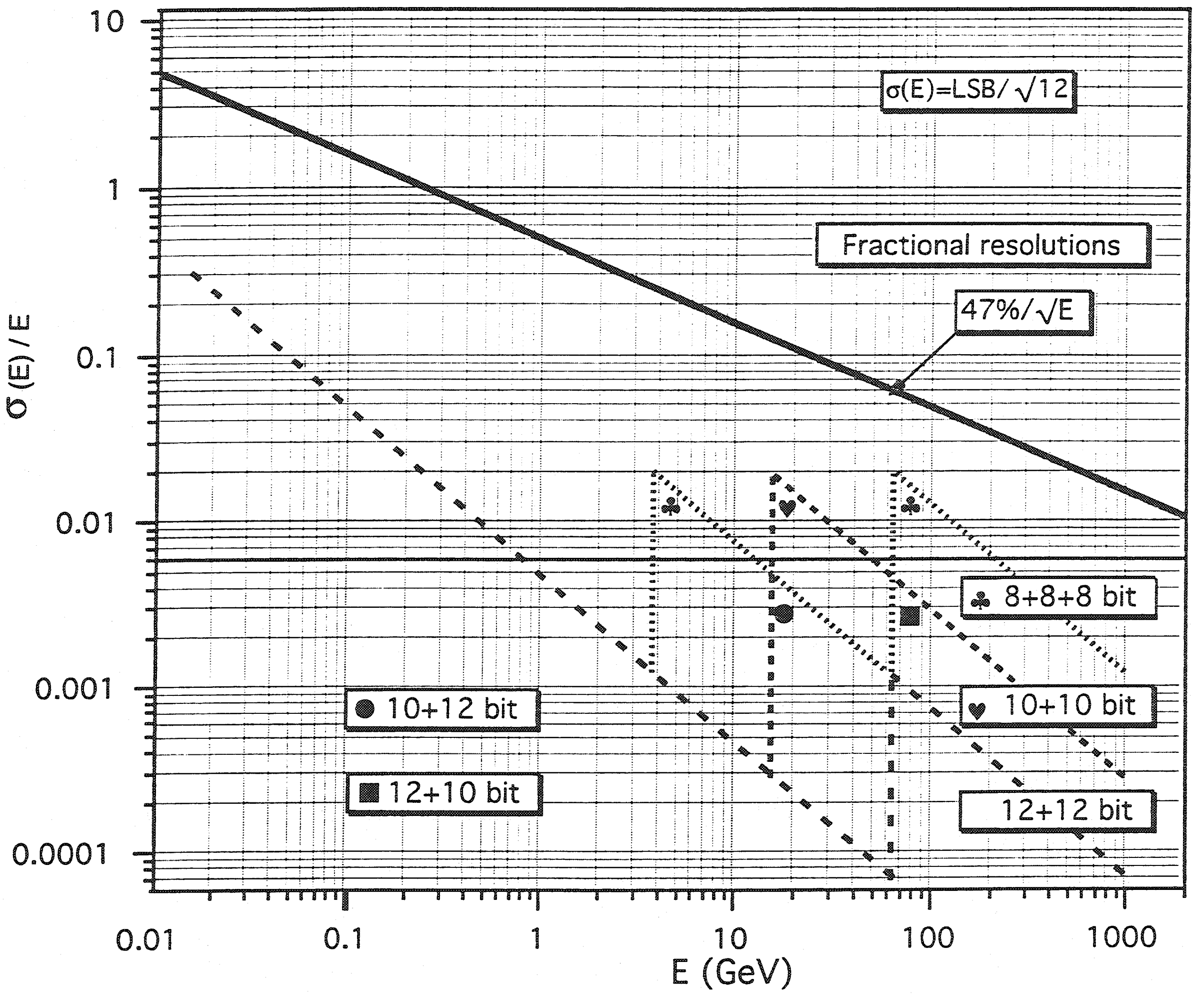

Figure 1: Analytical resolution for different configurations compared to the detector resolution for hadrons.

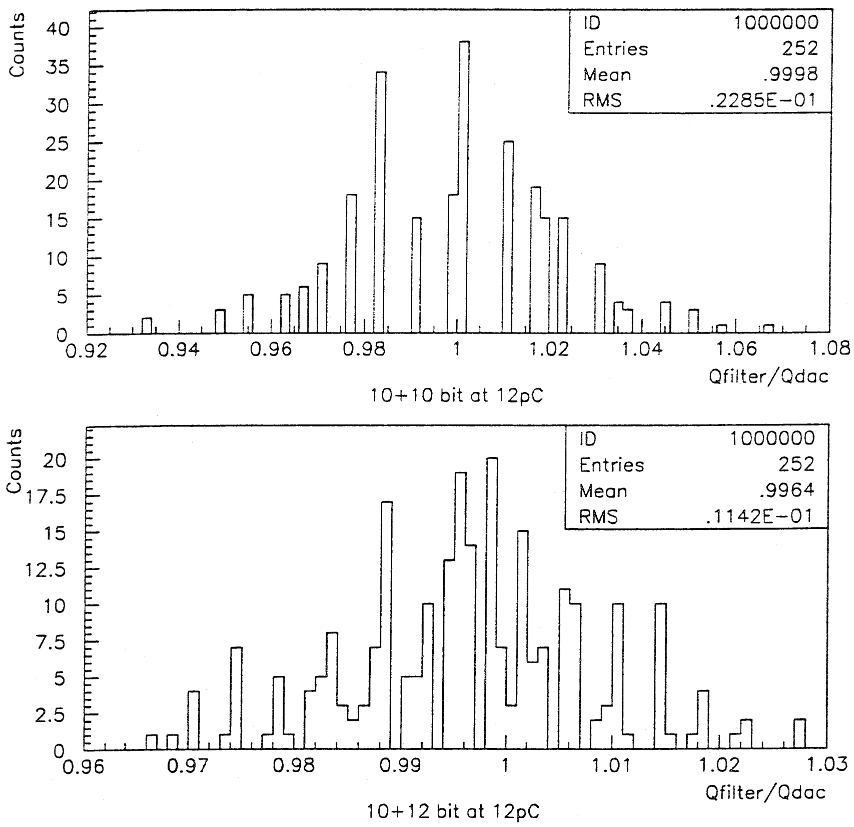

Figure 2: Internal resolution (σ/μ) at the most critical charge (12pC) for the 10+10 bit alternative (2.3%) compared to 10+12 bit (1.1%). One channel example.

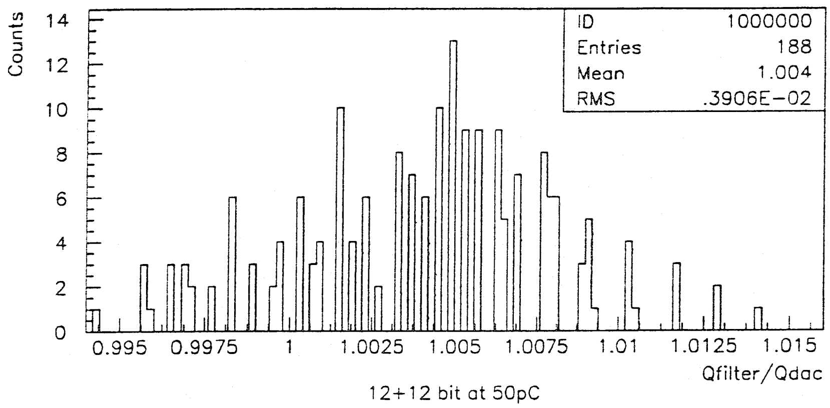

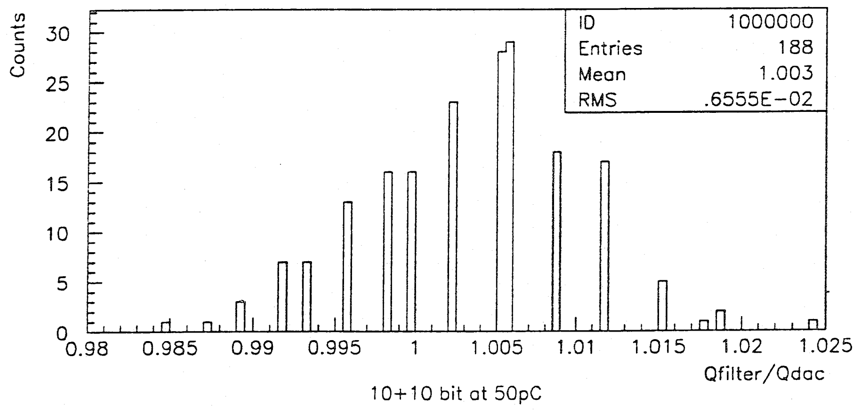

Figure 3: Internal resolution (σ/μ) at the most critical charge (50pC) for the 12+12 bit alternative (0.4%) compared to 10+10 bit (0.7%). One channel example.

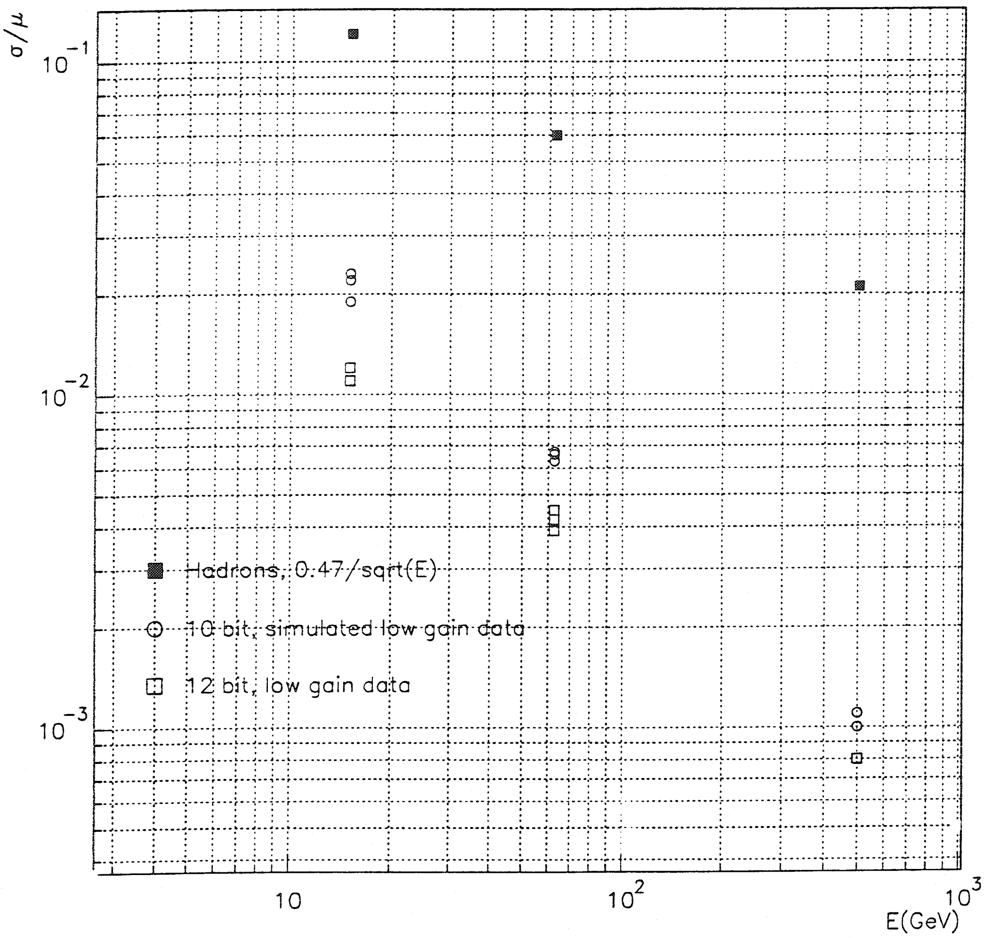

Figure 4: Internal resolution for three independent 10+10 bit 12+12 bit channels compared to the intrinsic hadron resolution of the detector at critical energies.

Publication II

ATLAS Internal Note
ATL-COM-TILECAL-99-012
11 May 1999

Jet reconstruction in the ATLAS Barrel Calorimeter

Jörgen Sjölin
Stockholm University

Abstract

Monte Carlo simulated light quark dijet events are investigated in the ATLAS Central and Extended Barrel calorimeters covering the pseudorapidity range up to 1.7. A standard cone algorithm and a jet energy reconstruction procedure using the information of the energy deposited in the various calorimeter compartments are used to evaluate the performance, both intrinsic and in the presence of noise and pile-up. The main results are based on the comparison between reconstructed jet energy and the particle level energy after fragmentation. Simple parameterizations of the resolution for different configurations are also provided.

Contents

1 Introduction

The calorimetry of ATLAS [1] consists of an EM calorimeter (Pb/LAr) covering the pseudorapidity region $|\eta| < 3.2$, a barrel hadronic calorimeter (Fe/Scintillator) covering $|\eta| < 1.7$ and an end-cap hadronic calorimeter (Cu/LAr) covering $1.5 < |\eta| < 3.2$. The forward calorimeter covers $3.1 < |\eta| < 4.9$. The various calorimeters have different degrees of non-compensation and the unavoidable presence of dead material makes the task of jet energy measurement very difficult. In this note simple and well known methods are used at each step in order to understand all the ingredients of the jet reconstruction chain from first principles. The main goal is to explore methods to restore the uniformity of the response by estimating the energy lost in dead material with the informations from the extra scintillators, by interpolation and by making use of the granularity of the detector. Hopefully it can also help those readers, completely new to the subject, to get some insight in the problem of jet reconstruction and energy evaluation.

2 Detector geometry

For many reasons it is desirable for a calorimeter to be perfectly homogeneous; however, due to practical and economical reasons this is not possible in a detector like ATLAS. Important factors are dead material in e.g. the cryostats, coils and unavoidable cables and beam pipes. One extremely critical region is e.g. the corner where EM accordion ends at $\eta = 1.45$ (see Figure 1 and Figure 2).

A very detailed description of the detectors and dead material is provided by DICE, the GEANT3 based detector simulation [2] (see Figure 1). The inner tracking detector is also included in the simulation. The information from the tracks is not explicitly used but the effects of the 0.5-1.0 radiation lengths of material, e.g. conversions and electron bremsstrahlung, are included in the simulation. The tracker of course plays a vital role e.g. in b and τ jet tagging and the information of the momenta of the charged tracks belonging to a jet could contribute to a better energy measurement, but this question is not addressed here.

A direction in space at vertex is specified by the boost invariant variables (ϕ, η), where ϕ is in the cylindrical symmetry direction, and η is the pseudorapidity. $\eta = -\ln\tan(\theta/2)$, where θ is the angular deviation from the beam axis.

The EM calorimeters have a very fine granularity optimized for EM shower measurements, whereas the granularity of the hadronic calorimeter, 0.1x0.1 in ηxϕ, is adapted to the size of a hadronic shower.

For jet reconstruction the standard strategy is to project the energy from the calorimeter cells into towers of 0.1x0.1 in ηxϕ.

3 Calorimeters within pseudorapidity $|\eta| < 1.7$

In the analysis presented in this note, the various calorimeter layers are chosen to be grouped into the following compartments, the acronyms represent the sum of the digitized energy from that compartment:

$EM_B(E_{1j})$: Liquid argon electromagnetic barrel accordion: the same weight is applied to all three longitudinal segments (also the 4th small segment at $\eta = 1.5$ is included);

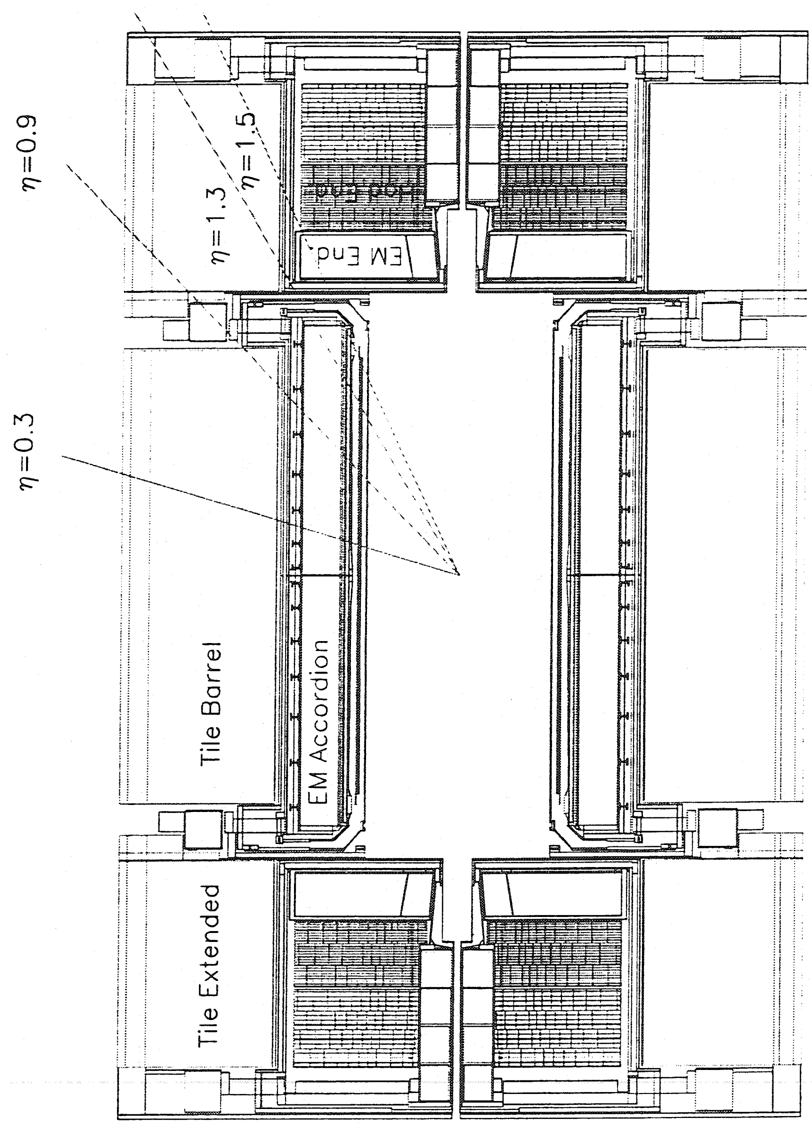

Figure 1: GEANT volumes defining the ATLAS calorimetry. Version 98-2. The outer radius of the Tile calorimeter is 4.2 meters.

$|\eta| < 1.475$;

$EM_E(E_{2j})$: the liquid argon electromagnetic endcap; all segments included; $1.375 < \eta < 3.2$;

$HAD_B(E_{3j})$: the Tile hadronic iron-scintillator barrel; all 3 segments included; $|\eta| < 1.0$;

$HAD_X(E_{4j})$: the Tile hadronic iron-scintillator extended barrel; all 3 segments included; $0.8 < \eta < 1.7$;

$HAD_E(E_{5j})$: the liquid argon hadronic endcap; all segments included; $1.5 < \eta < 3.2$.

The optimized weighted sum of these energies is referred to as E_{calo} and represents the estimated energy from the jet algorithm using the calorimeters only.

4 Complementary energy estimators for calorimetry

Beside the non compensation, i.e. electromagnetic and hadronic processes not giving the the same response in the calorimeter, the major cause for performance degradation is the energy lost in the dead material E_{dead} (see Figure 2). Dead material m_{dead} is defined as absorbing material that is not sampled. Its effect will depend on the location, e.g. if situated close to the shower maximum or not. The effect is also strongly dependent on the event topology, e.g. single particles like pions or wider object like jets. In ATLAS the design has been optimized such as to concentrate as much as possible of the dead material in a small interval at $|\eta| = 1.45$. To reduce the effect of the dead material, one can use estimators of the energy loss such as the ones used in this study:

$PS_B(E_{6j})$: the single layer LAr presampler to sample showers initiated in the inner tracker, inner cryostat walls and the coil; $|\eta| < 1.52$;

$CRYO_B(E_{7j})$: the geometric mean between the last layer in EM_B and the first layer in HAD_B estimates energy lost in the outer cryostat wall; $|\eta| < 1.0$;

$PLUG_1(E_{8j})$: the Intermediate Tile calorimeter ITC 1 in the barrel and extended barrel crack; $0.8 < |\eta| < 0.9$;

$PLUG_2(E_{9j})$: ITC 2; $0.9 < |\eta| < 1.0$;

$SCIN_1(E_{10j})$: the scintillator extension of the ITC in the barrel and extended barrel region; $1.0 < \eta < 1.2$;

$SCIN_2(E_{11j})$: $1.2 < |\eta| < 1.4$;

$SCIN_3(E_{12j})$: $1.4 < |\eta| < 1.6$;

$PS_E(E_{13j})$: the single layer LAr presampler to sample the concentration of material in the corner between EM barrel and EM endcap. $1.5 < |\eta| < 1.8$;

$CRYO_E(E_{14j})$: the geometric mean between the 6th,7th and 8th segment in EM_E and the first layer in HAD_X to estimate the energy in the endcap cryostat wall; $1.2 < |\eta| < 1.475$.

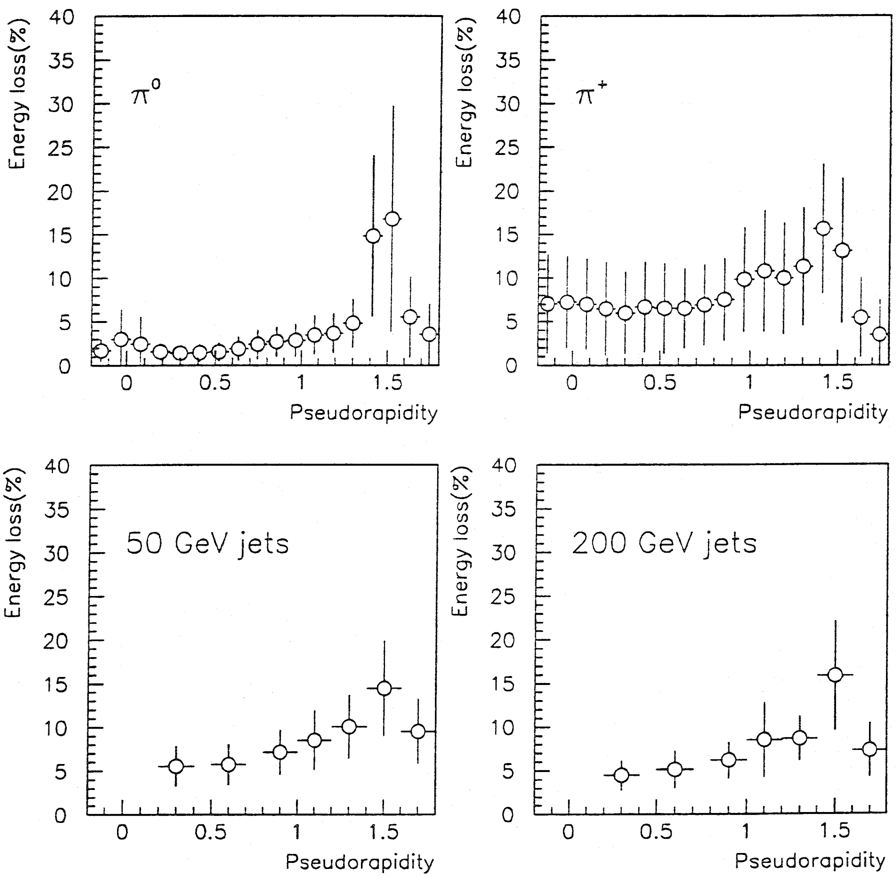

Figure 2: Energy lost in dead material. Jets are mostly a mixture of pions. The energy lost by π^0 is shown in the upper left figure and the one by π^+ in the upper right one. The vertical error bars represent the actual RMS of the distribution, not the error of the mean. One sees that the dead material is concentrated in a small window of about 0.2 in η at $|\eta|$=1.45. For charged pions, there are two components, the dead material in front of the calorimeter and the dead material between the EM and HAD calorimeters due to the outer cryostat wall. In the barrel there are larger fluctuations on the hadronic energy loss due to the fluctuation of the starting point of the hadronic shower.

This class of estimators $\mathcal{E}_{est} = \{E_{6j}, E_{7j}, .., E_{14j}\}$ have the potential to, on an event by event basis, reconstruct a fraction of E_{dead}; which is crucial since E_{dead} has large fluctuations. However, one must be aware that $\mathcal{E}_{est}$ is dependent on the jet energy. It is clearly visible from an energy scan of the estimator weights w_i after calibration (see Figure 3). The energy dependence of the weights is logarithmic as expected from the fact that e/π has a logarithmic energy dependence as well as the shower longitudinal size [3]. The validation and selection of the most efficient estimators were based on scatter plots that showed the correlation between the estimated energy loss and the true energy lost in the m_{dead} GEANT volumes (see Figure 4).

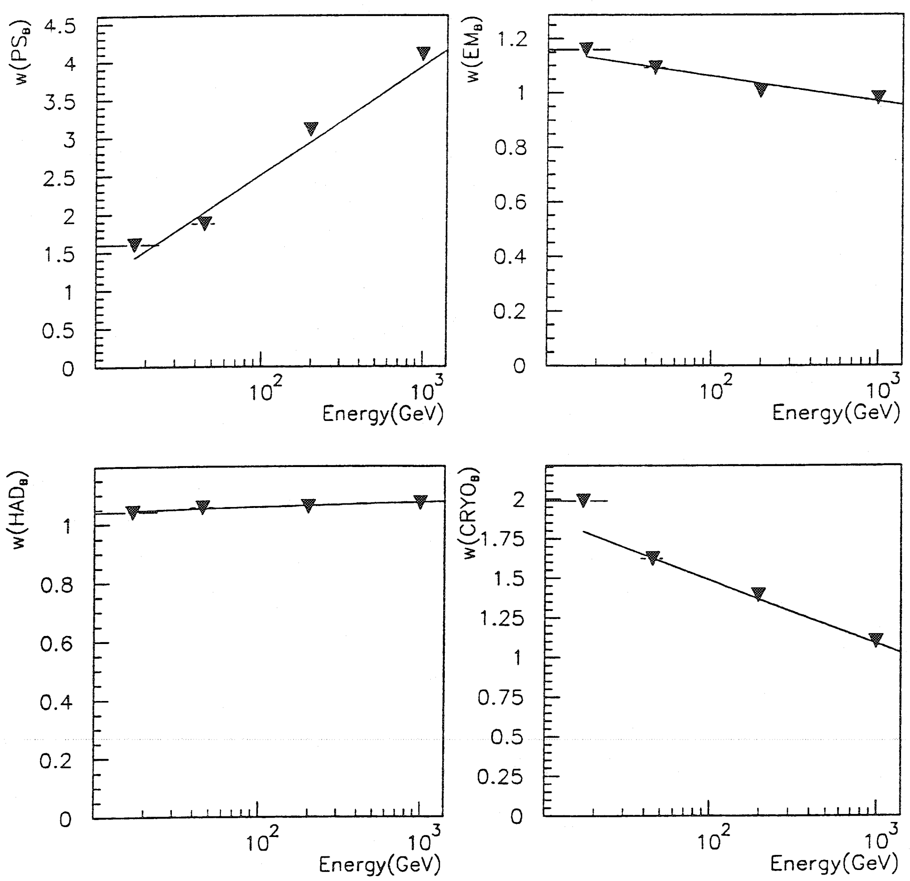

Figure 3: Weight energy dependence for the estimators E_{ij}, $|\eta| = 0.3$ and $cone = 0.7$. The small energy dependence for $w(HAD_B)$ is mainly due to an accidental e/π compensation by punch through leakage at high energy.

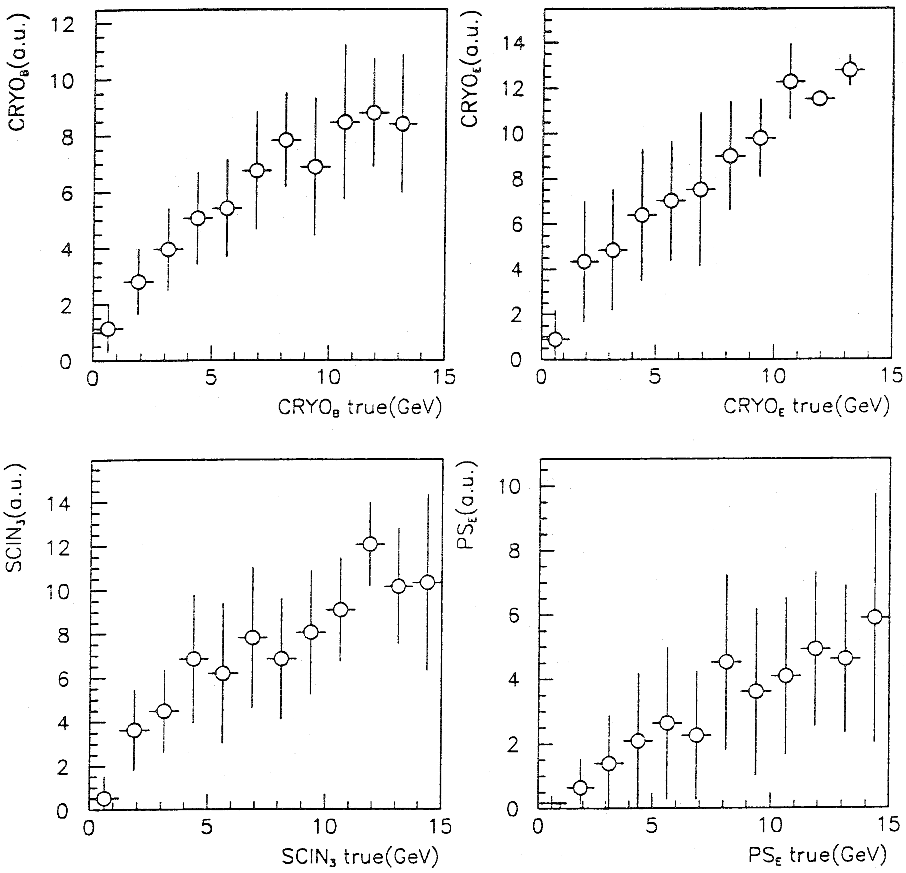

Figure 4: Correlation between the estimator and energy lost in the m_{dead} GEANT volumes. All plots except the upper right are based on π^+ simulations since only detailed m_{dead} volume information were available for π particles. The upper right plot shows energy in the endcap cryostat for 200 GeV jets at $|\eta| = 1.3$. The error bars give the RMS of the distribution.

5 Input data, event topology and selection

For the event topology $\mathcal{T}$, keeping in mind the spirit of maximum simplicity, the simulated event starts by generating back-to-back light quark anti-quark pairs using the generator PYTHIA 5.7 [4] with fixed energy at different fixed η positions but continuous in ϕ. After fragmentation the particles are tracked through the ATLAS detector with GEANT, digitized and reconstructed with the ATRECON package [5].

The quark energies [6] studied are 20, 50, 200 and 1000 GeV: 50 and 200 GeV are generated at $\eta = \{0.3, 0.6, 0.9, 1.1, 1.3, 1.5, 1.7\}$; while 20 GeV and 1000 GeV are generated at $\eta = \{0.3, 0.9, 1.3\}$ only. All jets reconstructed at particle level with more than 70% of the original parton energy and reconstructed in the calorimeter within 0.15 of the nominal

η, are kept for further analysis. This selection is done to decouple the effect of the tails of the fragmentation and study the intrinsic resolution of the calorimeter.

In the case of a proton-proton interaction, final state particles and beam remnants will be boosted in the forward direction so it is favorable to use boost invariant parameters like ϕ, η and E_T in the data analysis. However, non compensating calorimeters are sensitive to the total energy E deposited, therefore it is also useful to work with this quantity while studying calorimeter behavior.

Muons are minimum ionizing particles and usually carry energy beyond the hadronic calorimeters. Inclusion of this energy would require combined measurements with the muon chambers. However, less than 1% of the energy is carried by muons in the case of light quark jets. Hence any influence of the muons is simply ignored.

6 Jet definition

6.1 Jet algorithm

Jets are not clearly defined objects like elementary particles, but rather follow from definition. The definition is not unique, and the choice depend on algorithm performance for different observables and on implementations.

The most commonly used definition in hadron colliders up till now has been based on the cone algorithm [7]. The other main approach is based on clustering algorithms [8], e.g. the K_T algorithm [9]-[10]. From a theoretical point of view the standard cone is not favored due to the obvious lack of intrinsic infrared and collinear safety[1] which makes it difficult to compare higher order observable effects with theory. Due to this non uniqueness of the jet definition, the study of jet algorithms is an active field of research in phenomenology.

In this study a fixed cone algorithm of either size R=0.4 or R=0.7 has been used, where $R^2 = (\Delta\eta)^2 + (\Delta\phi)^2$. No treatment of jet overlap is applied. The algorithm is taken from the JetFinder Library [12] in ATRECON. Two thresholds define the jet in the cone algorithm: the initial jetseed E_T threshold $S_{(GeV)}$ and the minimum jet E_T threshold $T_{(GeV)}$. The reconstruction is done with the calorimeter calibrated at the EM scale. In addition, resolution effects, noise and pile-up, energy loss in dead material affect the visible energy (see Figure 5 and 6). Due to the event selection of the calibration sample the $S_{(GeV)}$ and $T_{(GeV)}$ are not critical as long as the efficiency is not severely affected, see table 1. The baseline definition is $S_{1.5}$ and T_7 for 20 GeV jets at $|\eta| = 0.3$ with no pile-up, and $S_{2.5}$ when pile-up is enabled (see the noise chapter for more details). For non pile-up 20 GeV jets (note that the jet energy is in E not E_T) at large $|\eta|$, $S_{0.8}$ and T_3 was used to avoid a biased selection of more energetic and hence EM rich jets which have a better resolution than the rest of the jet sample. $S_{(GeV)}$ for pile-up is kept constant due to the uniform pile-up level across η.

6.2 Separation of detector response and out of cone physics

To have a chance to understand the role of the detector, the detector specific effects must be disentangled from the out of cone physics. The way it is done here is the following: the true energy E_{true} is defined as the sum of those fragmented particles from the generator

[1] This drawback can be remedied by a simple modification to the iterative version of the cone algorithm[11].

Simu. level.	$S_{0.5}$	$S_{1.0}$	$S_{1.5}$	$S_{2.0}$	$S_{2.5}$	$S_{3.0}$
Generator(T_3)	2.6	2.6	2.6	2.4	2.3	2.1
Generator(T_7)	1.9	1.9	1.9	1.9	1.9	1.9
Calorimeter(T_3)	2.3(93)	2.2(94)	2.0(96)	1.7(98)	1.4(98)	1.0(98)
Calorimeter(T_7)	1.7(98)	1.7(98)	1.6(98)	1.5(99)	1.3(99)	1.0(99)
Calo.+noise(T_7)	1.6(97)	1.6(97)	1.6(97)	1.5(98)	1.2(98)	1.0(99)
Calo.+pile.(T_7)	15.2(8)	14.3(9)	9.5(13)	5.5(22)	3.4(30)	2.3(37)

Table 1: *EM* scale 20 GeV dijet multiplicity (purity in %) for R=0.4 and $|\eta|$ = 0.3 as a function of the jet seed $S_{(GeV)}$. The purity is defined here as the number of calo. jets within R=0.2 of a generator level jet divided by the number of calo. jets. Generator level means fragmented particles without the detector.

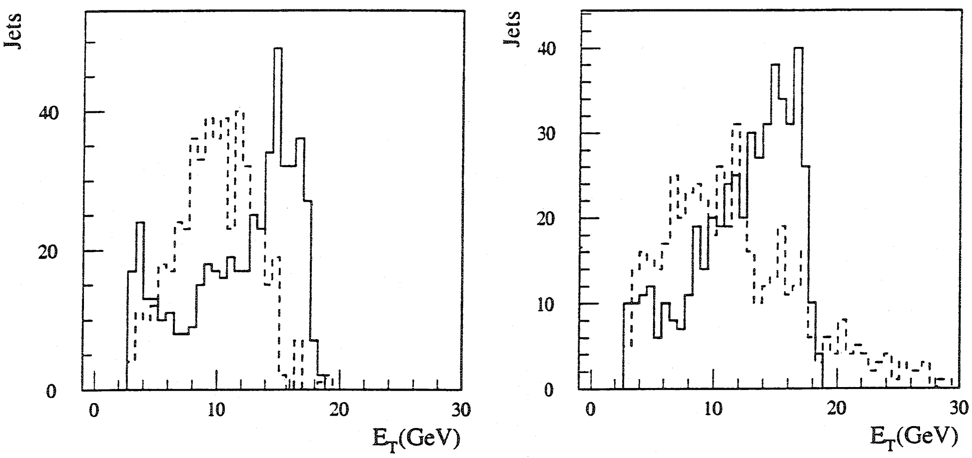

Figure 5: *EM* scale E_T distributions for 20 GeV jets, R=0.4 at $|\eta|$ = 0.3. Solid plots show generator E_T and dashed plots show calorimeter E_T. The EM scale response of the calorimeter is of course lower then at generator level, see figure 7. For the left plot no noise is added ($S_{1.5}$), and for the right plot electronic noise and pile-up are added ($S_{2.5}$). All plots are T_3 instead of T_7 in order to show more of the distributions. One jet is randomly selected from each event.

that, after bending in the magnetic field, pass within cells that belong to the reconstructed jet cone. That is, E_{true} is assumed to be the unknown energy that is to be measured and should not be confused with the original hard scatter tree level quark or gluon energy.

This enables us to concentrate on the detector performance for reconstructing jets by looking at the deviations between the reconstructed jet response and E_{true}. The reasons for deviation are many: energy lost in dead material, non compensation due to difference in electromagnetic and hadronic response $h/e \neq 1$, energy leaking out of the cone due to showers, longitudinal leakage at high energies, etc (see Figure 7). When those effects are under control, one can start to turn on the noise from the electronics, pile-up at high luminosity $\mathcal{L}$. Also any cell or tower cut thresholds E_{tresh} play an important role.

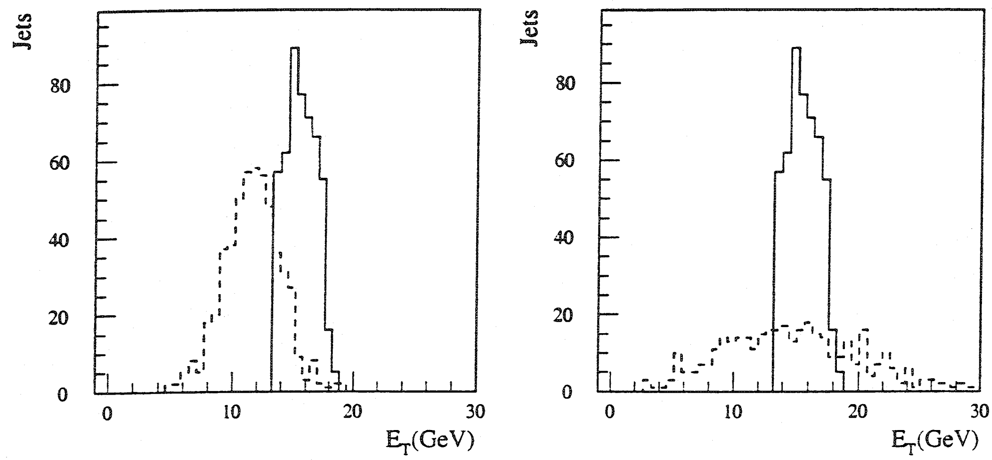

Figure 6: EM scale E_T distributions for 20 GeV jets after selection for the calibration sample, R=0.4 at $|\eta| = 0.3$. Solid plots show generator E_T and dashed plots show calorimeter E_T. For the left plot no noise is applied ($S_{1.5}$), and for the right plot electronic noise and pile-up are applied ($S_{2.5}$). All plots are T_3. The reconstruction efficiency of the pile-up jet sample in the calorimeter is 75% in this particular case.

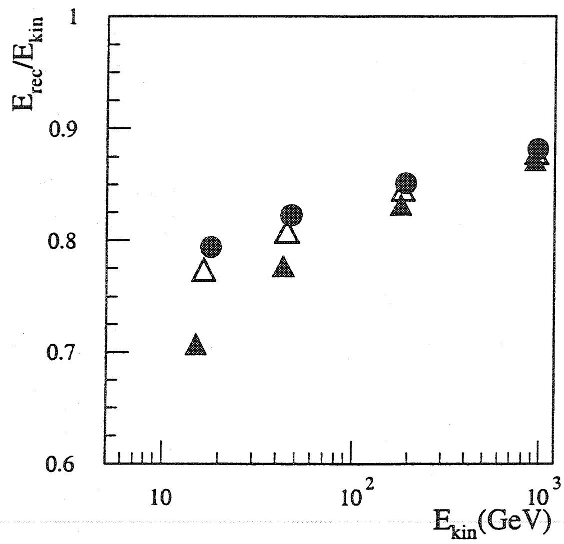

Figure 7: Mean relative reconstructed jet response using the EM calibration only at $|\eta| = 0.3$. R=0.4 (filled triangles), R=0.7 (open triangles) and R=1.5 (filled circles).

6.3 Jet energy reference reliability

As mentioned in the previous section, there is no clear definition of the true energy [2]. The cell approximation, fluctuations at the boundary of the cells or the theoretical jet cone

[2]This was clear in the ATRECON 1.42 version where only calorimeter cells with energy after cuts from the chosen jet finder were used for the true energy estimation. As a result the energy expected to be the

introduces uncertainties. By comparing the difference between the theoretical cone and the cell approximation it is possible to estimate the order of magnitude of this effect. The difference was found to be 3% or less. This is a rather large effect and sets a bound on how well the fluctuations in e.g. dead material can be compensated, regardless of the properties of the estimator.

Another source of uncertainty is low momentum particles. Charged particles are cut off by the bending magnet and curl within the magnetic field at $P_t < 0.5$ GeV. However, for these light quark jets the multiplicities of charged low p_T particles are very low and the impact on the jet energy was measured to be completely negligible, at least with no minimum bias background present. The total amount of low momentum photons was 3% or less within the jet.

7 Calibration

The reference given by E_{true} allows to disentangle the calibration of the detector from the problem of the definition of the jets, although in real life we will have to face both problems at the same time. Even with this simplification, the calibration C has still a complicated parameter dependence:

$$C = C(\mathcal{T}, \mathcal{L}, R, E, \eta, E_{thres})$$

That is, it is hard to provide a generic calibration for all situations without relying on compromises and parameterizations.

The first step in a Benchmark calibration is to equalize all subdetectors elements to the electromagnetic scale by for example using a known electron beam. However, a jet is composed of a mixture of electromagnetic EM and hadronic HAD interacting particles so the electromagnetic scale will on average not be correct. An effective way to compensate for this would be to study the energy dependence of every cell in every subdetector; then by looking at the energy deposited in each cell on an event to event basis correct to a common scale before adding up the total jet energy. This is what is done in e.g. the H1 method [13]. Just considering ATLAS 214000 EM cells and 20000 HAD cells gives you a flavor of that this is not a trivial task. But it can be done, just as in the H1 experiment, and as in smaller test beam analysis [14]. The reason why the problem becomes possible to handle in the end of the analysis is that the number of parameters can be vastly reduced by parameterizations.

What we do here is very simple. The detector compartments which behave in a similar way are clustered together at the EM scale and then the weighted sum of these compartments are optimized:

$$\min_{w_i} \sum_{j}^{Events} \Big(\sum_{i}^{Compart.} w_i E_{ij} - E_{true j} \Big)^2 \tag{1}$$

This will not correct for event to event fluctuations due to $h/e \neq 1$, but rather minimize the error on average for a given set of events, at least now the average is at the correct energy scale. The procedure is far from optimal; but if it is done with the C parameters fixed, the approximation for that configuration is good enough so that one can start to talk about combined calorimetry and study effects like energy lost in dead material.

truth showed strong dependence on the dead material when tower cuts were applied.

A subtlety which is worth mentioning is that this optimization has a small hidden linearity bias. The effect is so small that it does not really matter in this study[3], however it is instructive to see how this bias comes about. Let the model output energy be $E^* + n$, where n is a normal process $N(0, \sigma)$ and E the nominal energy. Then:

$$\min_{E^*} < (E^* + n - E)^2 >= \min_{E^*}\{E^{*^2} + < n^2 > + E^2 - 2EE^*\}$$

Since for a sampling calorimeter

$$\frac{\sigma^2}{E^{*2}} \simeq \frac{a^2}{E}$$

$$< n^2 >= \sigma^2 = \frac{a^2 E^{*^2}}{E}$$

one arrives at the somewhat surprising result:

$$E^* = E - a^2$$

For a 50 GeV jet this gives (see also fig. 8):

$$\frac{E^*}{E} = 1 - \frac{a^2}{E} = \{a \simeq 50\%\} = 0.995$$

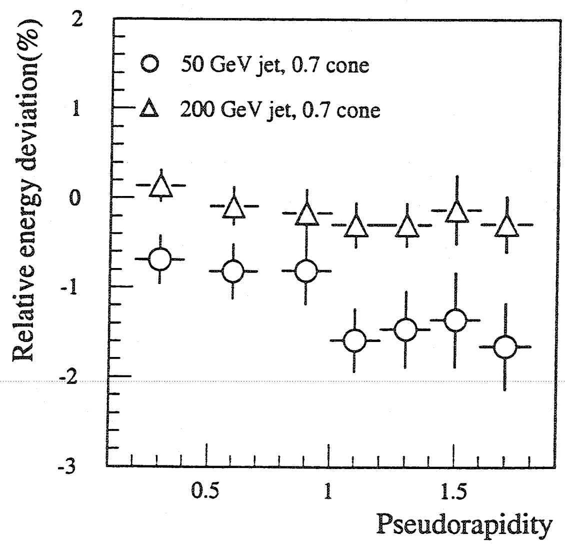

Figure 8: Linearity for 50 GeV and 200 GeV jets. Deviation from linearity is an artifact of the optimization procedure [15] and can be remedied by Lagrangian multipliers [14].

[3]By adding a linearity constraint is has been shown [14] that this side effect can easily be removed.

8 Electronic noise and pile-up

To understand the performance of the detector, one inevitably has to consider the effect of noise. At low $\mathcal{L}$ the dominant noise source is the electronics. The electronic noise is simulated in the digitization by adding gaussian noise according to the specifications for each calorimeter cell. At high $\mathcal{L}$, multiple minimum bias interactions per bunch crossing and the fact that the detectors are sensitive during more than one bunch have the effect of what can be regarded as an additional type of noise, the pile-up noise.

The reader should be aware that there are noise effects that are not included in the simulation. However the design goal is to reach a level were these effects are negligible compared to the intrinsic contributions. Example of such effects are quantization errors in the digitization and photo-electron statistics.

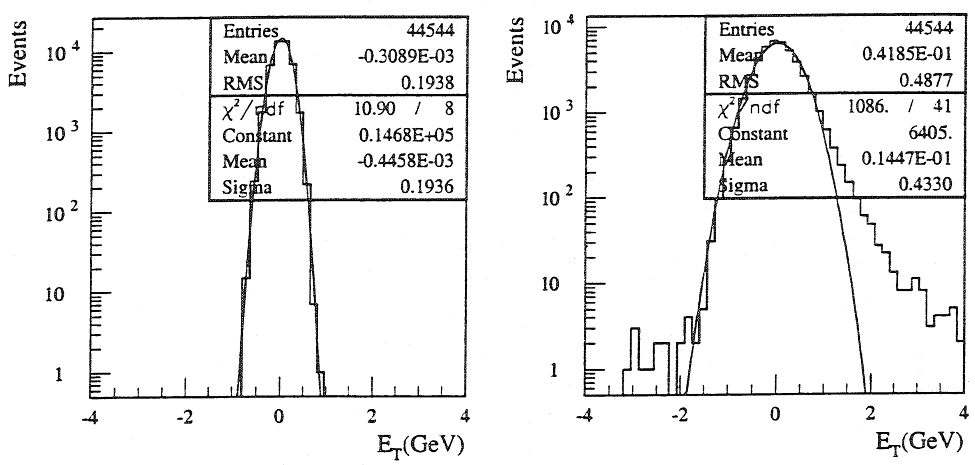

Figure 9: EM scale E_T tower noise distribution at $|\eta| < 0.3$. Left plot shows electronic noise, right plot shows electronic and pile-up noise. The non zero average of the right plot is due to the fact that no pedestal correction is applied in the simulation of the unipolar channels in Tile.

8.1 Electronic noise

The tower electronic noise is approximately 200 MeV (Figure 9 and 10) at the EM scale for $|\eta| < 1.7$ with digital filtering enabled [16]. This increases by $10\% - 20\%$ after weighting. Depending on the energy and the cone size the expected electronic noise level within the cone is ($C^{cone}_{noise-type} \simeq 1.2$ is a scaling constant due to the weighting):

$$E^{0.7}_{noise} = C^{0.7}_{elec} 0.2\sqrt{7^2\pi} \simeq 2.9 \text{ GeV}$$

$$E^{0.4}_{noise} = C^{0.4}_{elec} 0.2\sqrt{4^2\pi} \simeq 1.7 \text{ GeV}$$

The standard method to improve the signal to noise ratio SNR is to introduce an optimal cell cut E_{thresh}. However, one must be very careful to avoid any energy bias. For the electronic noise a symmetric cell cut suffices to keep the result unbiased. To get a feeling

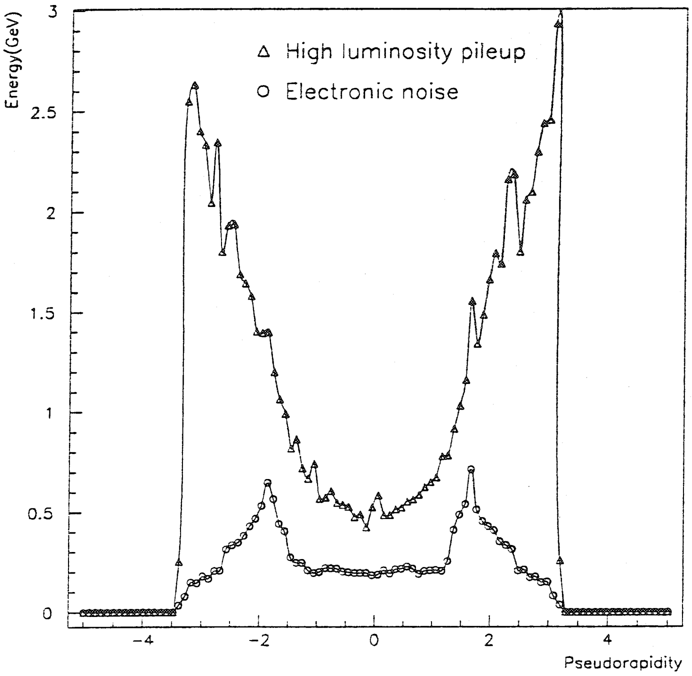

Figure 10: EM scale tower RMS noise as a function of η. The forward region is not included in the noise simulation. When plotting E_T rather then E the pile-up noise stays at 0.5 GeV for higher η.

how a cell cut works it is instructive to make a little toy example. In Figure 11 a uniformly distributed signal between 1 a.u. and 3 a.u. with and without additional Gaussian noise is symmetrically thresholded at 1.5 a.u. For a given noise with standard deviation σ there will be an optimal threshold which depends on the signal level and distribution. An example with the effects of different cell thresholds for 50 GeV jets is given in Table 2. From the table it is clear that the effect of signal loss when the threshold is large is less dramatic after adding noise, simply because smearing reduces the impact of the threshold. The optimal cell cut for electronic noise was found to be $1.5\sigma - 2.0\sigma$ for 50 GeV. For 20 GeV the minimum is very shallow. The overall improvement using thresholds seems not to be very significant, but thresholds are probably needed anyway for practical reasons to reduce the amount of information.

	0.0σ	1.0σ	1.5σ	2.0σ	2.5σ
no noise	7.8%	9.5%	11.4%	12.2%	14.0%
noise	11.2%	11.1%	10.8%	10.8%	11.2%

Table 2: 50 GeV jet resolution applying different cell cuts, with and without noise. $\eta = 0.3$ and R=0.7.

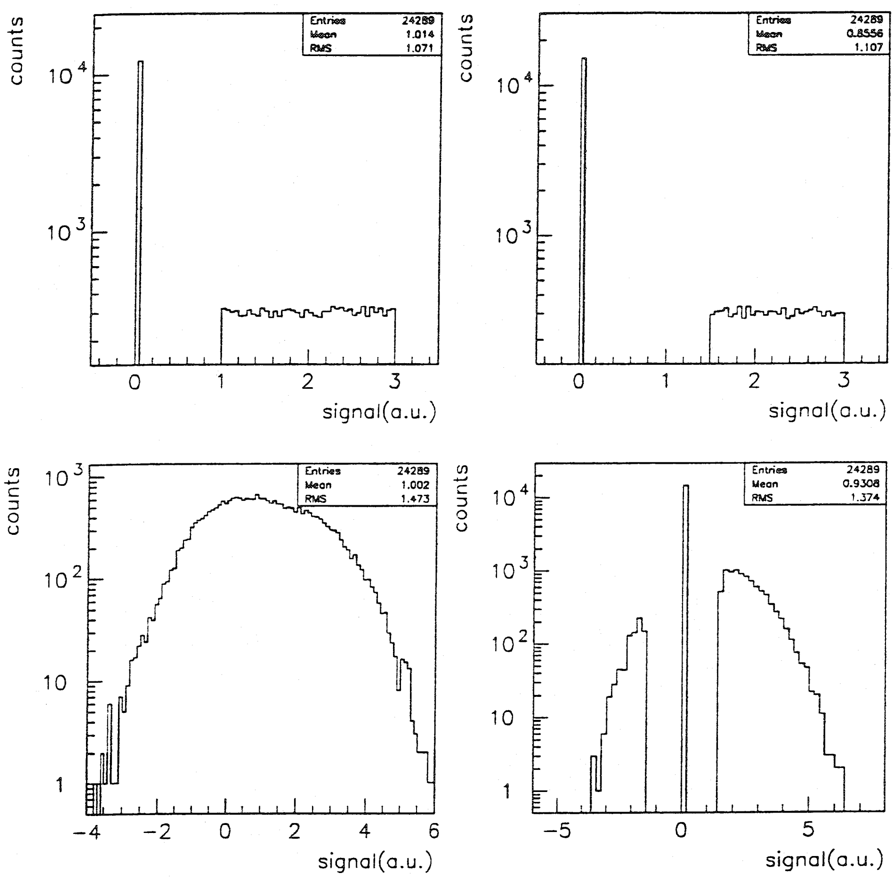

Figure 11: The effect of applying a threshold. It could e.g. be a cell in the calorimeter. The first plot shows a signal with a flat distribution between 1 a.u. and 3 a.u., the probability for a signal different from zero in the event is 50%, i.e. the mean is 1 a.u. In the second plot a threshold at 1.5 a.u. is applied (e.g. a cell cut). The effect of adding $N(0,\sigma)$ noise is shown in the last two plots. Notice how the expected mean of the signal is recovered by adding noise, and how the spread can be diminished by the threshold. The bottom line of this example is to enlighten the reader of the fundamental difference between thresholding a clean signal and thresholding in the presence of noise.

8.2 Pile-up

The simulation of pile-up is done separately and later added in the reconstruction phase [16]. Fully simulated minimum bias events are drawn with Poisson statistics (on average 23 events) and added to each cell during the reconstruction using the correct shaping function for each readout channel. Thus correlations in both space and time are considered. With the results from Figure 9 the expected pile-up noise level within the cone in the central barrel region is:

$$E^{0.4}_{pile-up} = C^{0.4}_p 0.5\sqrt{4^2\pi} \simeq 4.3 \text{ GeV}$$

assuming non coherent towers, which is not exactly true for pile-up.

To improve the SNR for the pile-up noise the most obvious technique is to apply a tower cut. Unfortunately the signal is not unbiased for pile-up. To study this effect a separate analysis was launched. The E_T tower map was stored separately, both generator level and EM calibrated calorimeter level energies. First the JetFinder cone algorithm was run on the generator level to find the proper jet direction, then a cone was applied on the calorimeter level using the proper jet direction. The result is summarized in Table 3. It is important to note that given the direction, no cut whatsoever is applied in the cone summation in order to maintain an unbiased estimator. The bias for pile-up with proper jet direction is expected since no baseline correction is implemented in the simulation for the unipolar Tile channels. The pile-up noise is positive and hence introduces a positive baseline shift. [4] This bias must be corrected before the jet calibration. If this was the only bias source it would now be possible to search for an optimal tower cut since we have full control of the unbiased signal loss once we start to cut. To make this clear, applying any cuts on a biased signal renders the signal useless unless you have complete control of the noise convoluted signal loss. However, there is also another bias, not in the cell energy but in the jet energy estimator which has to do with the intrinsic thresholds in the definition of the jet. The large pile-up bias with jet directions from the calorimeter level cone algorithm hints at the fact that the jet direction is not stable for 20 GeV jets at high luminosity. Not enough data was available to fully understand the energy dependence at low energy. Since robust jet estimator bias corrections were not possible, results with optimal tower cuts are not presented.

	Part. direc. E_T (GeV)	Calo. direc. E_T (GeV)
no noise	11.2	11.7
electronic noise	11.2	11.8
pile-up noise	13.3	15.6

Table 3: Mean E_T for 20 GeV jets, R=0.4 and EM scale calibration using jet direction from particle level or calorimeter level. All jets are pure according to the purity definition in Table 1.

8.3 Reconstruction of the jet direction

Throughout this analysis the jet direction is calculated at the EM scale. It should be noted that the resolution is expected to be improved after proper energy calibration. This option is not further pursued.

Using the particle level jet direction as a reference it is interesting to verify the jet angular resolution, both in η and in ϕ. The angular resolution for 20 GeV jets at $|\eta| = 0.3$ is shown in Table 4.

[4] The bipolar shaping in LAr automatically averages any trigger independent signal (e.g. minimum bias events) to zero.

	$\delta\eta$ (mrad)	$\delta\phi$ (mrad)
no noise	43±3	43±4
electronic noise	49±4	49±3
pile-up noise	59±4	59±4

Table 4: Angular resolution for 20 GeV jets, 0.4 cone, $|\eta| = 0.3$ and EM scale calibration All jets are pure according to the purity definition in Table 1.

9 Main simulation results

The main simulation results concern the resolution of reconstructed jets. The response should be as uniform as possible in η, and conform to the design goal:

$$\frac{\sigma}{E} = \frac{50\%}{\sqrt{E}} \oplus 3\%$$

9.1 Uniformity in η

By performing the minimization defined in (1), at each η point for fixed energies, η uniformity scans were produced (see Figure 12). To find the best set of estimators in the calibration (1), the optimization was performed in several steps. Since many of the estimators are correlated, it was not obvious which one to prefer. By first including all of the estimators the optimizer hints at the best estimators since they have a smaller relative error. As is usually the case for multi parameter fits it is beneficial to reduce the number of free parameters as much as possible. This was done by pruning the estimators with very large errors. This was found to be an effective and robust approach. For an example see table 5.

In Figure 12 one can see that for 50 GeV and $R = 0.4$ the dominant effect at high $|\eta|$ is the fluctuation of energy outside of the cone. The effect can easily be understood geometrically by looking at the relationship:

$$\eta = -\frac{1}{2} \ln \tan \theta/2$$

differentiation leads to,

$$\delta\eta = \frac{1}{2|\sin\theta|}\delta\theta$$

consequently an initial spread in θ translates into an increasing spread in η at large $|\eta|$. The effect is less pronounced at higher energies since the boost makes the jet narrower.

As can be expected, there is still an influence of the dead material. However, there is significant improvement compared to the performance without some of the E_{dead} estimators. Especially the scintillators turns out to be effective for compensating E_{dead}, see Figure 13.

9.2 Energy dependence

The jet reconstruction performance of the calorimeter can also be explored with only the energy as a free parameter. In Figure 14 energy scans are shown for $\eta = 0.3$ and $\eta = 1.3$. The large effect of the cone size and noise for lower energies is clear. One might ask why

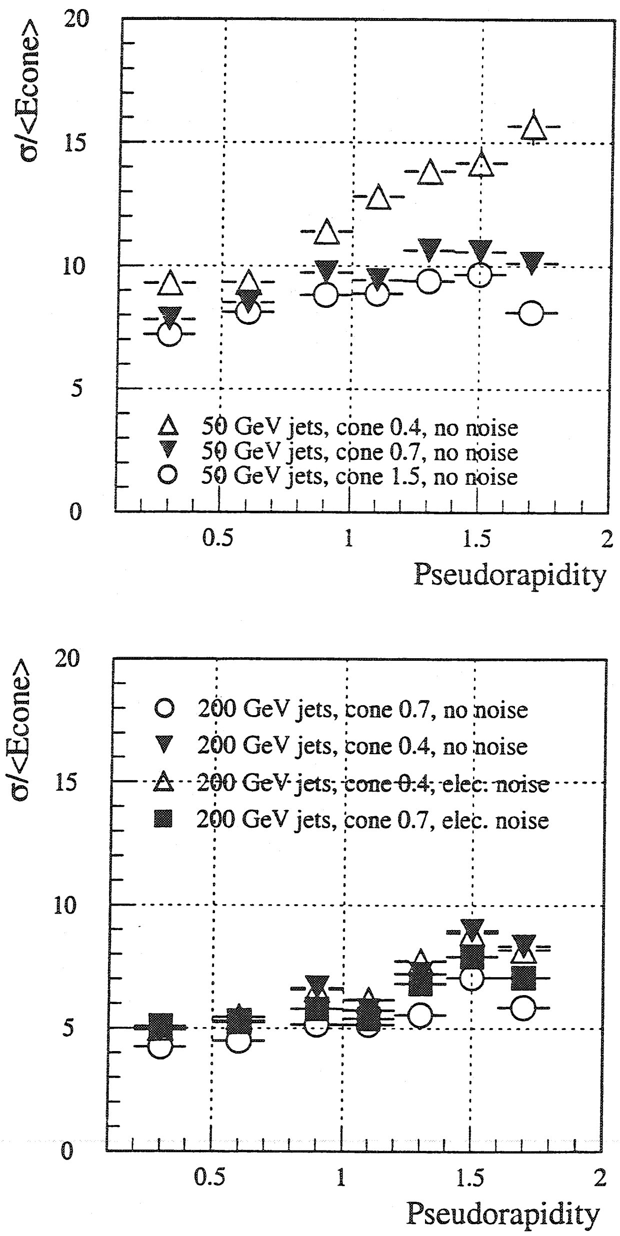

Figure 12: Resolution for 50 GeV and 200 GeV jets, all estimators for energy lost in dead material included.

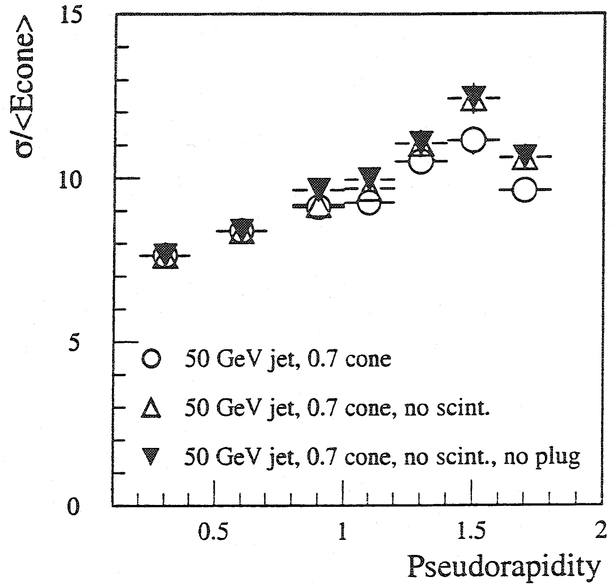

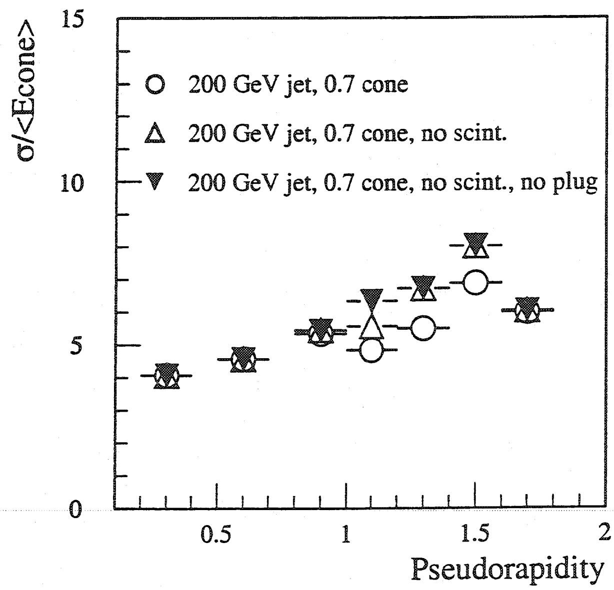

Figure 13: Resolution for 50 GeV and 200 GeV jets, estimator influence on energy reconstruction.

η	PS_B	EM_B	HAD_B	$CRYO_B$	HAD_X	EM_E	HAD_E
0.3	2.63	1.02	1.06	1.38	0.00	0.00	0.00
0.6	2.23	1.00	1.01	1.26	0.00	0.00	0.00
0.9	2.20	0.97	0.98	1.57	0.98	0.00	0.00
1.1	1.55	1.00	0.41	2.70	1.06	2.84	0.00
1.3	1.16	1.07	0.00	4.60	1.13	1.71	1.48
1.5	1.23	1.23	0.00	0.00	1.02	1.09	1.51
1.7	1.55	2.15	0.00	0.00	0.24	1.01	1.27

η	$PLUG_1$	$PLUG_2$	$SCIN_1$	$SCIN_2$	$SCIN_3$	PS_E	$CRYO_E$
0.3	0.00	0.00	0.00	0.00	0.00	0.00	0.00
0.6	0.00	0.00	0.00	0.00	0.00	0.00	0.00
0.9	1.66	2.35	2.51	0.00	0.00	0.00	0.00
1.1	0.17	5.62	1.30	2.65	0.00	0.00	0.23
1.3	0.00	0.00	1.47	1.54	0.65	4.75	0.12
1.5	0.00	0.00	0.00	1.62	0.79	1.19	0.46
1.7	0.00	0.00	0.00	0.00	1.67	1.51	0.97

Table 5: Calibration weights for jets at 200 GeV and R=0.7. The correction is from EM scale to E_{true}.

$R = 0.7$ is included since the resolution is better with $R = 0.4$ when noise is added. However, thresholding the cell energies changes the situation and $R = 0.7$ can become competitive. As we have seen in the section describing the noise the improvement with thresholds is not that dramatic; but, in reality thresholds play an important role to reduce the vast amount of information and may be unavoidable.

9.3 Parameterization of the jet resolution

The parameterization of the jet resolution as a function of energy for different configurations is shown in Figure 14 and Table 6. The resolution can be split into three main contributions with different energy dependence: statistical fluctuations that scale as $\sqrt{E}$ (e.g. the sampling in the calorimeter), linear terms due to e.g. miscalibrations or noncompensation, and a constant term due to noise. In the parameterization the terms are assumed to be uncorrelated thus

$$\sigma^2 = (a\sqrt{E})^2 + (bE)^2 + c^2$$

or in a more common notation

$$\frac{\sigma}{E} = \frac{a}{\sqrt{E}} \oplus b \oplus \frac{c}{E}$$

These parameterizations can be compared to those made in fast simulations such as ATLFAST [18].

When the noise is compared with and without cell cuts, the sampling and the linear term is held constant in order to understand the noise contribution. The reason for fixing the parameters is that they are correlated. It is probably true that the sampling term is affected by the cell cuts but the effect is assumed to be small.

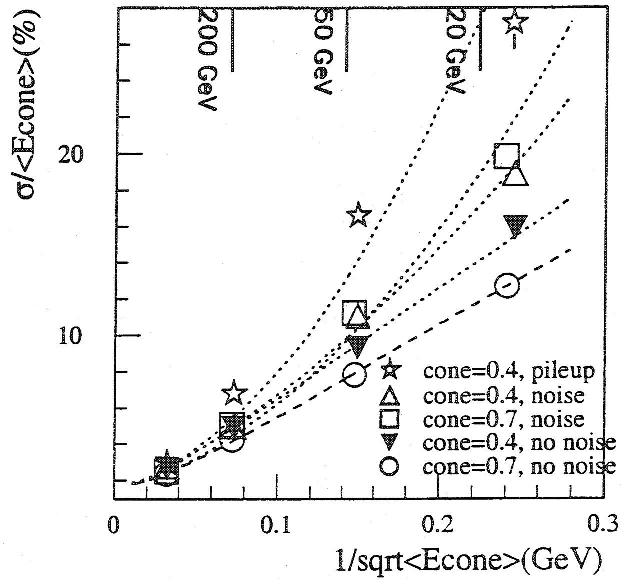

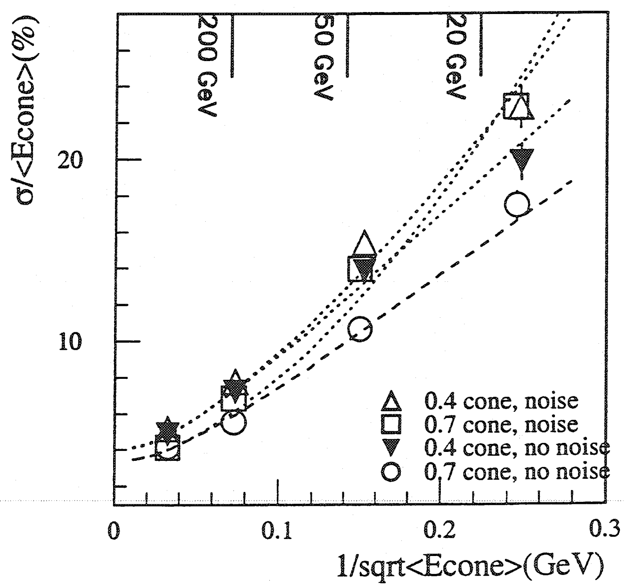

Figure 14: Jet resolution energy dependence. Upper plot η=0.3, and lower plot η=1.3. No cell cut has been applied to the noise.

$Cone$	η	$a(\%GeV^{1/2})$	$b(\%)$	$c_{0\sigma}(GeV)$	$c_{2.5\sigma}(GeV)$
0.7	0.3	52.3±1.1	1.7±0.1	3.0±0.1	2.0±0.1
0.4	0.3	62.4±1.4	1.7±0.2	2.0±0.1 (pile-up 4.7±0.2)	1.7±0.2
1.5	0.3	48.2±0.9	1.8±0.1		
0.7	0.9	63.0±1.5	2.0±0.3	2.7±0.2	
0.4	0.9	74.7±2.1	2.7±0.5	1.9±0.3	
0.7	1.3	66.1±2.1	3.4±0.2	2.9±0.2	
0.4	1.3	82.3±2.6	4.0±0.3	2.0±0.3	

Table 6: Parameterization of the jet resolution. During the fit of the noise term, the a and b parameters are kept fixed. The c term is given for two different cell cuts, either at 0σ or 2.5σ of the noise.

10 Calibration for jets from full detector simulation

The data set available was rather limited for a complete calibration. However, using the data at hand and the results from this note a "first order" calibration [17] was produced for data analysis of the GEANT simulated jets. In the central barrel energy parameterization of the weights was implemented, both with and without noise. For an example of the parameterization of the weights see Figure 3. Outside that region an approximation to the nearest available fixed energy calibration is made. If the absolute scale is not critical, using a calibration from another energy does not seriously affect the resolution (see Figure 15). The calibration has been tested on the physics channel $W \to jj$, see Figure 16. For energy and eta distributions for the jets from the W decay, see Figure 17. The jets are mostly light quarks with a mixture of ~20% c-quarks and less then 1% b-quarks. The calibrated jet residuals for this set of data are shown in Figure 18.

The resolution for the mass with calibrated jets is clearly not in perfect agreement with the fast parameterization. This is somewhat expected since the reconstruction fail to completely unfold all effects that are not parametrized.

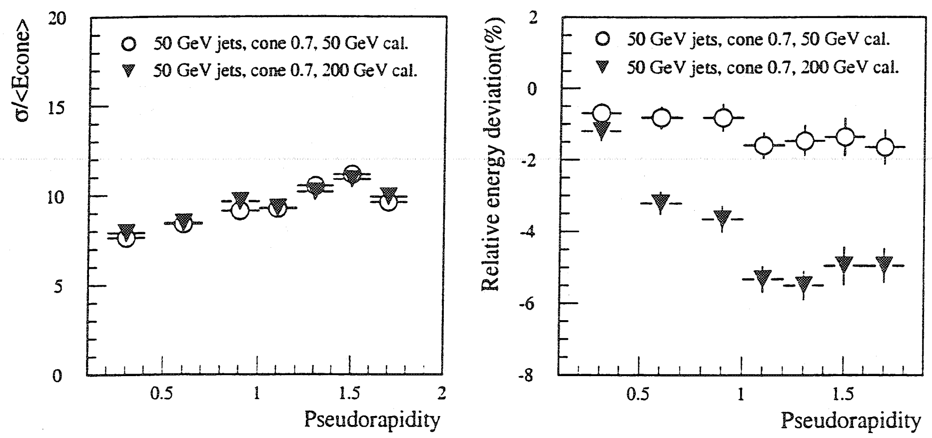

Figure 15: 50 GeV jets using weights from 200 GeV calibration.

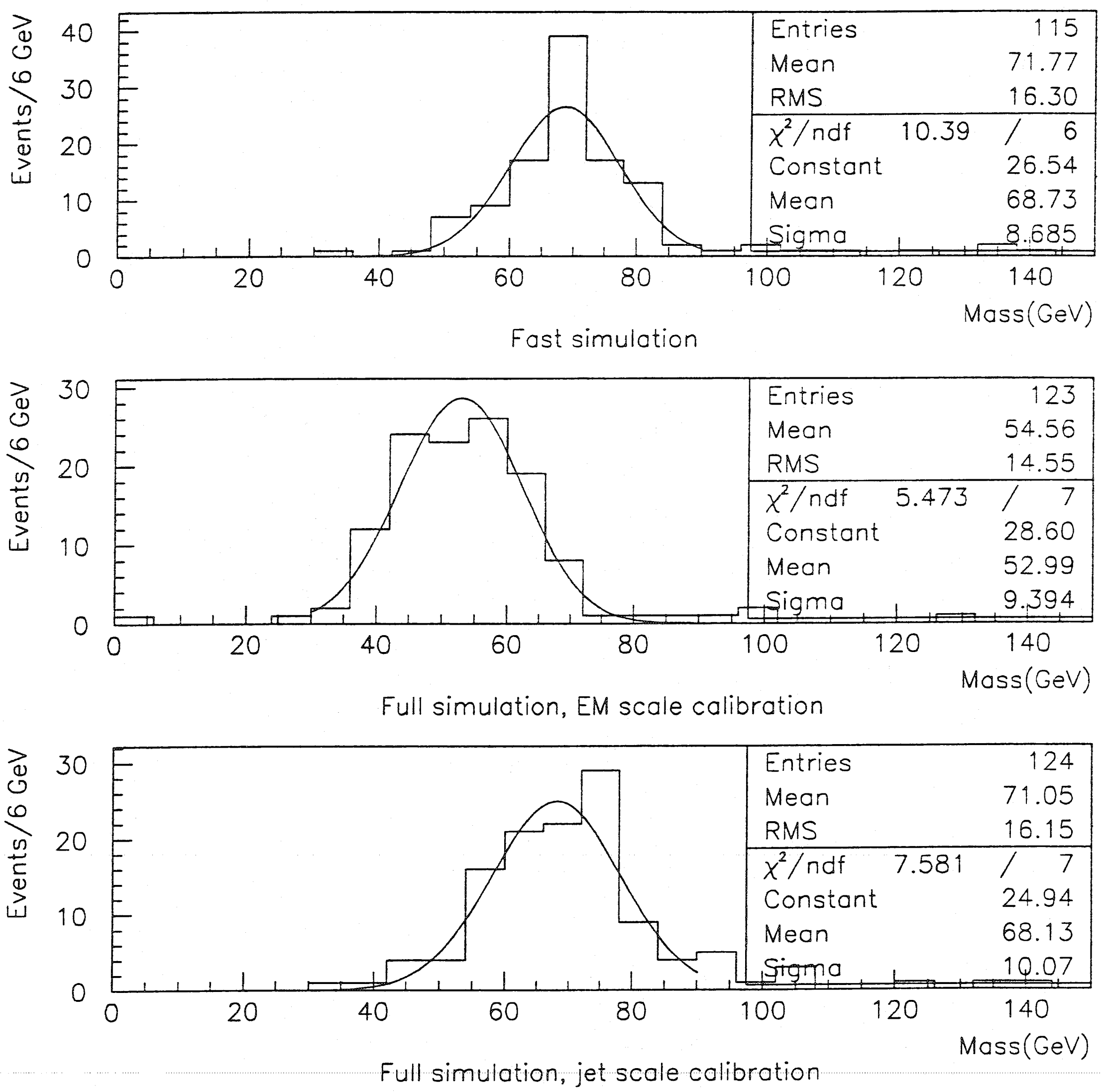

Figure 16: Reconstruction of the invariant mass from the decay $W \rightarrow jj$. The top plot shows the mass reconstructed with ATLFAST [18]. The mass shift is due the the final state radiation and fragmentation loss which leaks out of the cone. The middle plot shows the result using full simulation but with only EM calibration. The bottom plot shows full simulation with the complete detector calibration explained in this note. All examples uses $R = 0.4$.

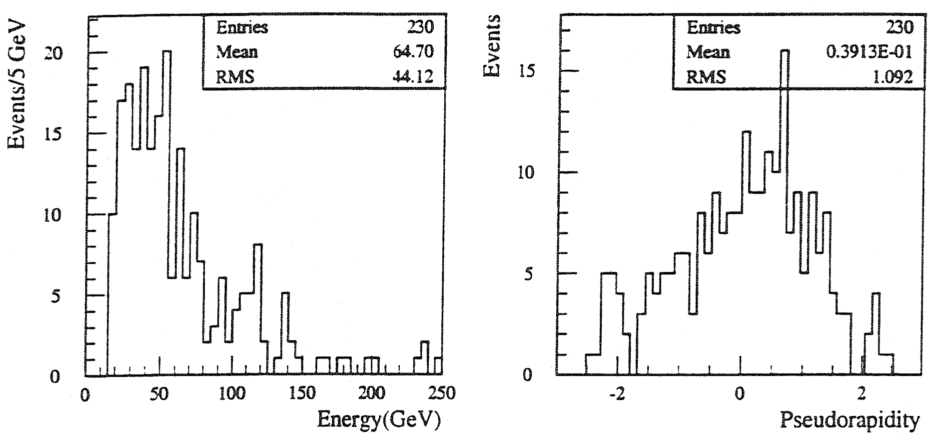

Figure 17: Jet energy and eta distributions for the $W \to jj$ decay.

11 Conclusions

Light dijet events up $|\eta| < 1.7$ have been analyzed with the updated new geometry. Compared to previous analyses made for the ATLAS Calorimeter Performance Technical Design Report, no major degradation of the resolution have been detected. The effects of electronic and pile-up noise have also been studied. However, the pile-up noise is not unbiased and a more detailed analysis is necessary to state qualitative numbers of the performance with applied cuts.

Acknowledgments

I want to thank Martine Bosman for proposing this work and for her patience and useful answers to my endless and sometimes stupid questions.

References

[1] ATLAS Technical Proposal CERN/LHCC/94-43

[2] GEANT 3, ATLAS version 3216 98_2. DICE 3.20 geometry and digitization. 14 aug. 1998. /afs/cern.ch/atlas/offline/hp_ux102/98_2/bin/dice.

[3] R., Wigmans, Nucl. Instr. Meth. **A259** (1987) 389.

[4] PYTHIA 5.7, T. Sjöstrand, Computer Physics Commun. **82** (1994) 74.

[5] ATRECON 1.42, 8 march 1999. Redigitization of TILE, see DICE 3.21. /afs/cern.ch/atlas/project/physics/combined/jets/atrecon/atrecon142_new.

[6] M. Rashid, Calorimeter scan jet production, http://home.cern.ch/mrashid/caloprod.html

[7] G. Sterman and S. Weinberg, Phys. Rev. Lett. **39**, 1436 (1977)

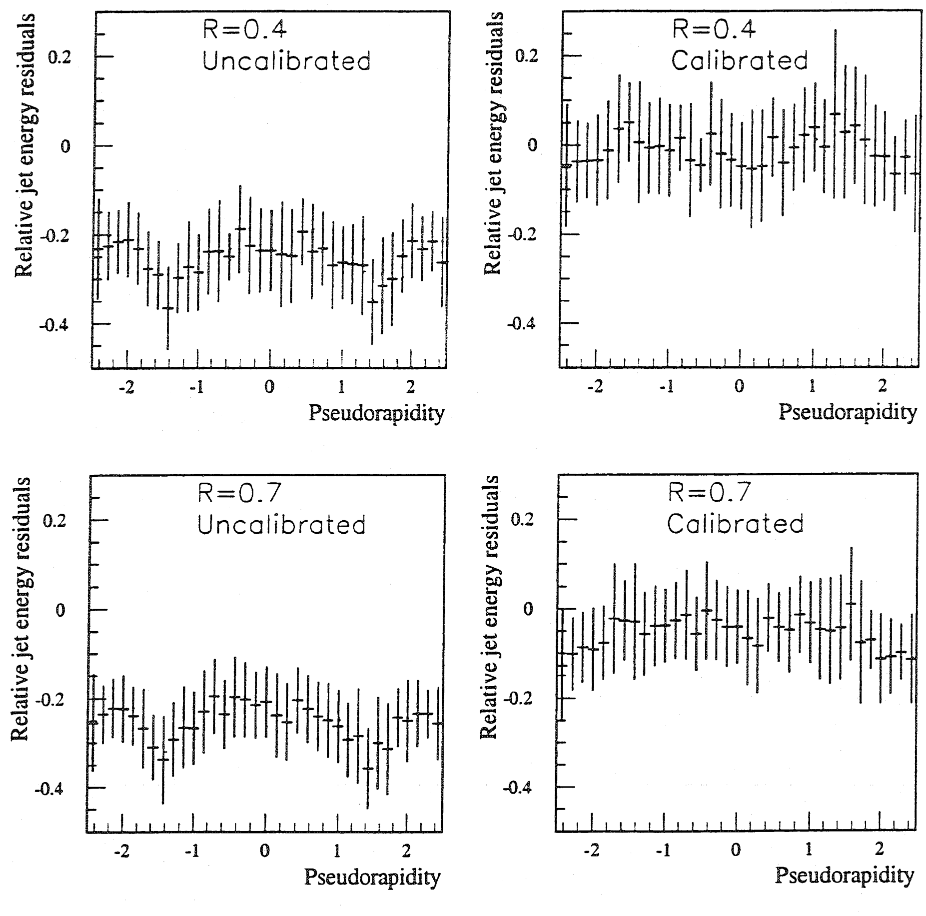

Figure 18: Relative jet energy residuals between $(E_{calo} - E_{true})/E_{true}$ for the $W \to jj$ data sample. There seems to be a problem with the absolute energy scale for $|\eta| > 1.7$. Large $|\eta|$ calibrations were imported and there could perhaps be a mismatch when the weights are applied. Error bars are distribution widths.

[8] T. Sjöstrand, Comp. Phys. Commun. **28** 227 (1983).

[9] M. Seymour, Zeit. Phys. **C62** 127 (1993).

[10] S.D. Ellis and D.E. Soper, Phys Rev. D. **48** 2160 (1993).

[11] T Akers er al., OPAL Collaboration, Z. Phys. **C63** 197 (1994).

[12] M. Bosman et al., Jet Finder Library ver. 1.0, ATLAS Internal Note ATL-SOFT-98-038 (1998).

[13] H1 Calorimeter Group, W. Braunschweig et al., Results from a Test of a Pb Fe Liquid Argon Calorimeter, DESY Internal Report, DESY 89-022 (1989).

[14] M.P.Casado and M. Cavalli-Sforza, H1-inspired analysis of the 1994 combined test of the Liquid Argon and Tilecal calorimeter prototypes, ATL-TILECAL-96-075 (1996).

[15] D. Lincoln et. al., A Hidden Bias in a Common Calorimeter Calibration Scheme, FERMILAB-Pub-93/394 (1993)

[16] S. Simion, Pile-up Simulation for Atlas Calorimeters, CERN/ATL-SOFT-99-001.

[17] Jet calibrations for data analysis with the combined ntuple: http://atlasinfo.cern.ch/Atlas/GROUPS/PHYSICS/JETS/jets.html

[18] E. Richter-Was, D. Froidevaux and L. Poggioli, ATLFAST 2.22, ATL-COM-PHYS-98-011 (1998)

Publication III

ATLAS Internal Note
ATL-COM-PHYS-2000-XXX
25 May, 2000

A study of Gauge Mediated Supersymmetry Breaking with $\tilde{\tau}_1$ as the NLSP in the ATLAS detector

Jörgen Sjölin
Stockholm University

(DRAFT)

Abstract

The feasibility for mass measurements of SUSY particles from GMSB models with $\tilde{\tau}_1$ as the NLSP in the ATLAS detector is studied using parameterized simulations. The measured particles are selected such that model parameters can be estimated.

Contents

1 Introduction

The Higgs field added to the Standard Model (SM) to render it renormalizable has a very famous hierarchy problem associated with it. The plausible models available today that can explain this hierarchy all imply new exotic physics. Probably the most favored alternative is that the world is supersymmetric (SUSY) at high energies. Since all current low energy observations can be explained without SUSY, there must exist a mechanism that breaks SUSY at lower energy into the Standard Model (SM) if SUSY shall have any room to play in the domain of TeV physics. An interesting model from an experimental point of view[1] is Gauge Mediated SUSY Breaking (GMSB) [1]. Much of the GMSB phenomenology applicable for the ATLAS detector has already been explored in a previous study [2]. This note takes a closer look at a few points in the parameter space of GMSB models where the the $\tilde{\tau}_1$ slepton is the next-to-lightest sparticle (NLSP). The lifetime of the NLSP depends on a free parameter. Two cases are investigated, either the NLSP decays close to the production vertex or outside of the detector. The lifetime is actually one of the most important handles on the model as is pointed out in [3]. However, lifetime measurements require detailed full simulation which is outside the scope of this note.

2 The model

The effective models of GMSB is a sub class of models within the framework of the Minimal Supersymmetric extension of the Standard Model (MSSM). Due to general arguments e.g. soft SUSY breaking (SSB) the number of parameters in MSSM are 124 in addition to the 19 in the SM. Much of the MSSM parameter space is highly unphysical including e.g. rapid proton decay and lepton number violation and hence so called R-parity conservation is added ad hoc. In order to understand the model some assumptions must be made concerning the origin of the SSB terms. One such assumption is GMSB. In GMSB the *observable sector* **O** containing the Standard Model fields communicates with a *messenger sector* **M** usually built up by GUT preserving gauge fields. **M** then mediates the SSB by overlapping with a rather unspecified *secluded sector* **S**

$$\mathbf{O} \xleftarrow{SU(5),SU(10)..} \mathbf{M} \xleftarrow{X} \mathbf{S}$$

This automatically generates small flavor violations and preserves Grand Unification. In the minimal version of GMSB (mGMSB) the model is fully determined by six parameters:

- $\Lambda_m = F_m/M_m$, the effective SUSY breaking scale. Here chosen to be 30 TeV.
- M_m, the messenger scale. The messenger scale it set to 250 TeV.
- N_5, the parameterization of the $SU(5)$ messenger fields. Here N_5 is set to 3.
- $\tan\beta$, the ratio of the Higgs vacuum expectation values at the electroweak scale.
- sgn μ, the sign of the Higgsino mass term. Here sgn $\mu = +1$
- C_{grav}, the gravitino mass scaling factor.

Throughout this note the GMSB events are generated by the GMSB implementation in ISAJET 7.48 [4]. The major theoretical arguments at the moment against GMSB are the origin of the Higgs parameters μ and B see [1], which in mGMSB are assumed to be determined at the EW-scale, and the somewhat ad hoc use of gauge fields.

[1]But rather dull from a theoretical viewpoint since the inevitable introduction of gravity is postponed.

3 Phenomenology

3.1 The NLSP and the mass spectrum

The dominant SUSY production is through glue and quark interactions into gluino or squark pairs [5]. However, there is also an interesting contribution from prompt neutralino, chargino and slepton production [6]. Due to the imposed R-parity the sparticles will be pair produced and decay down to the LSP. The LSP in mGMSB models is a very light gravitino for any relevant value of the fundamental SSB scale $F \sim C_{grav} F_m$

$$m_{\tilde{G}} = \frac{F}{\sqrt{3}M_P} \leq 1\text{keV},$$

where M_P is the reduced Planck mass. This is expected since the model is constructed to keep flavor violations small and hence gravitational effects must be suppressed. The upper bound on $m_{\tilde{G}}$ actually comes from cosmology [1]. For most of the parameter space the NLSP is either a $\tilde{\chi}_1^0$, co-NLSP $\tilde{l}_R$, a $\tilde{\tau}_1$ or $\tilde{\chi}_1^0$ and $\tilde{\tau}_1$ co-NLSP. In a very small corner of parameter space $\tilde{\nu}$ NLSP is also possible. An inverted case with the $\tilde{g}$ as NLSP happens when M_m is very very large. For the parameters in this note the NLSP is either $\tilde{\tau}_1$ (G3) or co-NLSP $\tilde{l}_R$ (G2), see Table 1. The models G2a and G2b were investigated in [2]. The

Point	Λ_m (TeV)	M_m (TeV)	N_5	$\tan\beta$	sgn μ	C_{grav}
G2a	30	250	3	5	+	1
G2b	30	250	3	5	+	5000
G3a	30	250	3	12	+	1
G3b	30	250	3	12	+	5000

Table 1: The GMSB model parameters. For the long lived NLSP case the decay is disabled via the ISAJET option NOGRAV.

sleptons are co-NLSP in this case and decay close to vertex for $C_{grav} = 1$or outside the detector when the gravitino mass is rescaled. As $\tan\beta$ is increased the $\tilde{\tau}_1$ becomes the NLSP due to mixing effects proportional to m_τ. The other SUSY mass differences due to the shift in $\tan\beta$ appears to be of less phenomenological importance (see Table 2). The connection

Particle	G2	G3	Particle	G2	G3	Particle	G2	G3
$\tilde{g}$	699	699						
$\tilde{u}_L$	658	658	$\tilde{u}_R$	635	635	$\tilde{\chi}_1^0$	113.9	115.5
$\tilde{d}_L$	662	662	$\tilde{d}_R$	634	634	$\tilde{\chi}_2^0$	196.2	196.1
$\tilde{t}_2$	674	672	$\tilde{t}_1$	577	582	$\tilde{\chi}_3^0$	277	265
$\tilde{b}_2$	640	644	$\tilde{b}_1$	631	626	$\tilde{\chi}_4^0$	329.9	316.5
$\tilde{e}_L$	204.1	204.5	$\tilde{e}_R$	102.7	103.3	$\tilde{\chi}_1^\pm$	191.8	193.0
$\tilde{\tau}_2$	204	207	$\tilde{\tau}_1$	101.6	97.4	$\tilde{\chi}_2^\pm$	328	316
$\tilde{\nu}$	189	188	$\tilde{\nu}_\tau$	189	188			
h^0	106	111	H^0	337	311			
A^0	334	311	$H^\pm$	344	321			

Table 2: Masses in GeV as $\tan\beta$ is increased from 5 to 12. Note that $\tilde{e}$ and $\tilde{\mu}$ are degenerate.

between the model parameters and the physical mass spectrum is according to [1] at leading order proportional to $N_5\Lambda_m$ for the gaugino masses, and $\sqrt{N_5}\Lambda_m$ for the slepton masses.

There is also an overall logarithmic dependence on M_m due to the boundary conditions for the RGEs.

3.2 Topology

Typical signatures at the end of the decay chain for the G2 and G3 models are

G2

$$\begin{array}{llll} \tilde{\chi}_1^0 & \to & \tilde{\mu}_R^{\pm} & \mu^{\mp} \\ & & | & \\ & & \to & \tilde{G} \quad \mu^{\pm} \end{array}$$

G3

$$\begin{array}{lllll} \tilde{\chi}_1^0 & \to & \tilde{\mu}_R^{\pm} & \mu^{\mp} & \\ & & | & & \\ & & \to & \tilde{\tau}_1 & \mu^{\pm} \ (\tau) \\ & & & | & \\ & & & \to & \tilde{G} \quad \tau \end{array}$$

Due to the $\tilde{G}$ all GMSB scenarios produce missing E_T. One exception is when the NLSP is quasi-stable, charged, reconstructed and included in the E_T calculation. In this study the quasi-stable NLSP is included. If the NLSP is charged and quasi-stable its mass and momentum can be fully reconstructed in the muon system and the background in that environment is not an issue.

The signature for the G3 models unconditionally involves τ which makes the detection more challenging compared to the G2 case. The decay mode at the end of the decay chain is either of the type

$$\tilde{\mu}_R^{\pm}(\tilde{e}_R^{\pm}) \to \tilde{\tau}_1 + \mu^{\pm}(e^{\pm}) + \tau \tag{1}$$

when the $\tilde{\tau}_1$ decays outside the detector, or if the $\tilde{\tau}_1$ lifetime is very short

$$\tilde{\tau}_1^{\pm} \to \tau^{\pm} + \tilde{G} \tag{2}$$

Due to the limited phase-space in the decay (1), the τ lepton is undetectable.

A very large fraction of the events contains the decay

$$\tilde{\chi}^0 \to \tilde{\mu}_R^{\pm}(\tilde{e}_R^{\pm}) + \mu^{\mp}(e^{\mp}) \tag{3}$$

which provides a very clear same flavor opposite charge (SOC) dilepton signal. The SOC results in sharp mass edges (see appendix A) and also removes most of the light QCD background. By forming the flavor combination

$$\mu^+\mu^- + e^+e^- - \mu^{\pm}e^{\mp} \tag{4}$$

a lot of the combinatorial background can be subtracted.

A standard handle on the SUSY signals is M_{eff}. M_{eff} is defined as

$$M_{\text{eff}} = \max_{|\vec{p}_{T_{\text{jet},i}}|} \sum_i^4 |\vec{p}_{T_{\text{jet},i}}| + E_{T_{\text{miss}}}$$

This is very useful since squarks and gluinos generate a lot of hard jets. For prompt $\tilde{\chi}^0$, $\tilde{\chi}^{\pm}$ and $\tilde{l}$ production this is not the case, and one has to rely on $E_{T_{\text{miss}}}$ and e.g. a lepton signature.

3.3 From mass measurements to model parameters

In the same way as parameters in the SM can be extracted from various precision observables, parameters in an underlying SUSY model can be estimated. Following the approach outlined in [2] the SUSY masses are here used to fit the most probable model parameters. If sgn μ and C_{grav} are held fixed there are four independent parameters. Hence, in absence of degeneracy four independent masses should be enough to pinpoint the model. The light higgs mass m_h is assumed to be measured independently within ± 3 GeV. The minimum set of masses are a squark or gluino mass, the $\tilde{\chi}_1^0$ and $\tilde{\chi}_2^0$ masses[2] and a slepton mass. Conceptually the situation looks like

$$p_j \xrightarrow{M_i} m_i \xrightarrow{D} m_i^* \tag{5}$$

where $M_i(p_j)$ are the masses of the model parameters p_j. D represents the smearing of the detector. To find the inverse mapping back to p_j a fit is made using the known errors

$$\chi^2 = \sum_1 \frac{(M(p_j) - m_i^*)^2}{\sigma_i^2} \tag{6}$$

4 Experimental setup

4.1 Production

4.1.1 SUSY Signal and integrated luminosity

The total cross-section for SUSY production in the G3 models is 17 pb. Assuming the LHC low luminosity of 10^{33} cm^{-2}s^{-1}, one year yields a total integrated luminosity of 30 fb^{-1}. Let us say that 10 fb^{-1} will be available, then 170000 SUSY events should be simulated for correct statistical fluctuations. Here all SUSY models use 170000 signal events to represent one year of low luminosity.

Of the total signal 10% is due to prompt gaugino and slepton production. Since the jet multiplicity for prompt production is much lower than for the strong production, a jet veto enables very effective selection of this type of events. Prompt production can e.g. be interesting in an exclusive cross-section analysis.

4.1.2 Standard model background

For model G3b the SM background is not an issue due to the presence of heavy charged particles. However, since the signature in G3a contains SM particles only, the SM background is significant. The Monte Carlo cross-sections for the main SM contributions are listed in Table 3. Only backgrounds with potentially large Ptmiss and dilepton signals have been evaluated. All background events are simulated by PYTHIA [7]. Examples of background compared to signal are shown in Figure 1. The number of plotted events are always rescaled to 10 fb^{-1} and hence the statistical fluctuations are equal or larger than expected.

4.2 Trigger

The signal has a fairly high probability to pass the trigger due to the presence of very high P_T jets, see e.g. the leading jet variable in Figure 1. The results given by ATLFAST for the standard trigger menu options XE50+J50 and J180 are shown in Table 4. XE50 represents missing E_T above 50 GeV, and J180 represents jets above 180 GeV. For prompt production in G3a, the trigger criteria τ20+XE30 combined with a jet veto was investigated. The acceptance for prompt production with this trigger was found to be 9%.

[2]Looking at the mass relations [1] they turn out not be closely related.

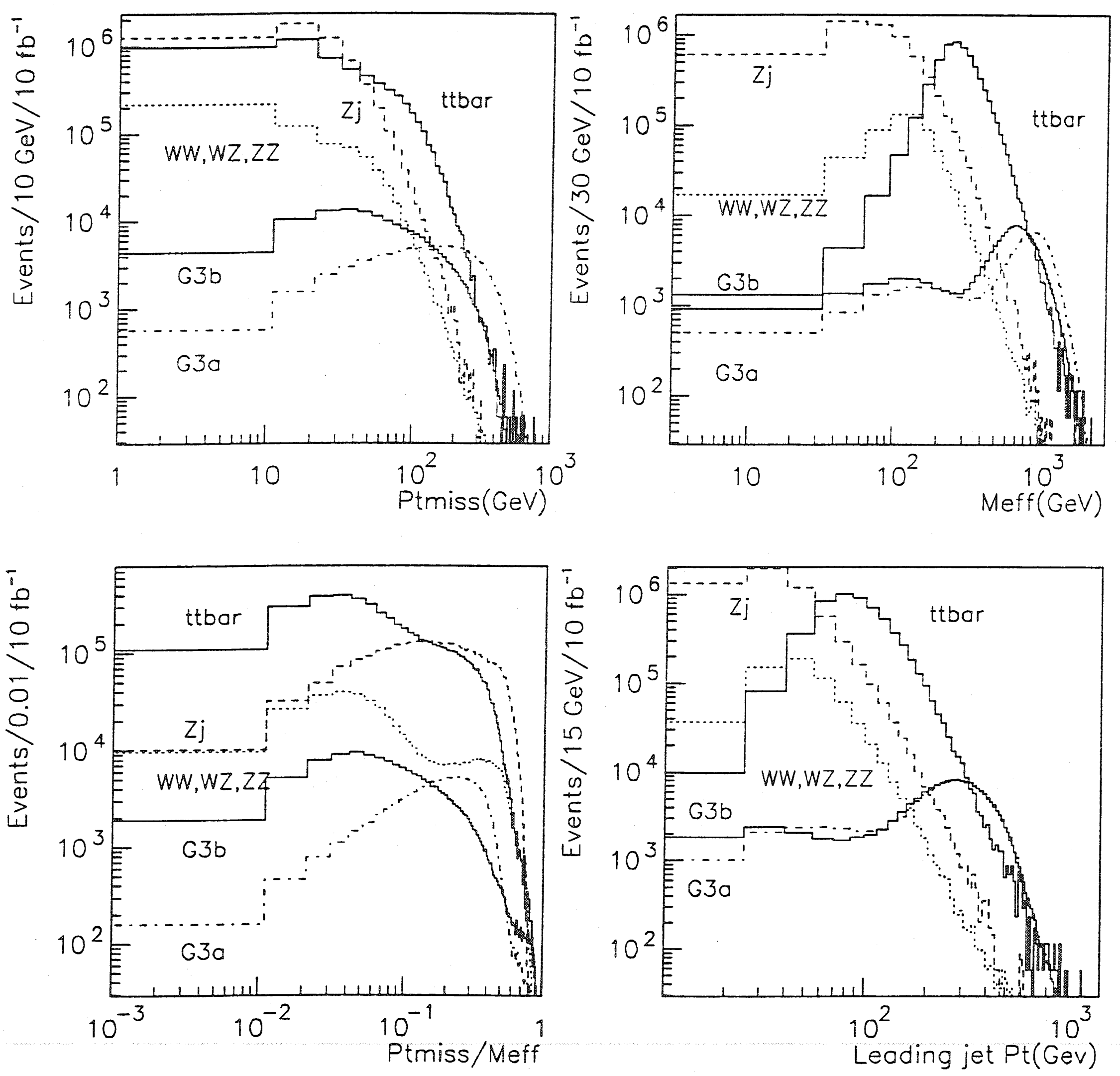

Figure 1: Variables that can be used to control the SM background. The signal is also included in the plots for comparison. It is quite obvious that $t\bar{t}$ is the most dangerous background. Meff is defined as the scalar sum of the four leading jets plus Ptmiss. The number of events shown in the plot are events reconstructed in the detector, but without trigger efficiencies.

Channel	σ[pb]	Events prod.	Events simu.
$t\bar{t}$	580 (833 [8])	5.8M	400k
Wj($p_T > 20$ GeV)	35000	350M	200k
Zj($p_T > 20$ GeV)	580	5.8M	200k
WW,WZ,ZZ	65	650k	200k
QCD($p_T > 50$ GeV)	$23 \cdot 10^6$	$2.3 \cdot 10^{11}$	300k
$b\bar{b}$($p_T > 50$ GeV)	88000	880M	300k

Table 3: SM backgrounds used in the simulations. All Z are $Z \to \tau^+\tau^-$. A separate sample of $b\bar{b}$ is included since it produces potentially dangerous dimuon signals at the 1.2% level.

Channel	XE50+J50[%]	J180[%]
G3a	92	83
G3b	62	87 (0.015 Hz)
$t\bar{t}$	31	7.3 (0.04 Hz)
Wj($p_T > 20$ GeV)	4.0	0.7
Zj($p_T > 20$ GeV)	6.0	0.6
WW,WZ,ZZ	10	1.3
QCD($p_T > 50$ GeV)	0.05	0.5 (100 Hz)
$b\bar{b}$($p_T > 50$ GeV)	0.7	0.6

Table 4: Fraction of the events that pass the trigger criteria. The results are from ATLFAST. The equivalent trigger rates are shown within parentheses. No efficiencies are included. Note that the true trigger rates are higher since no pile-up is included in the simulation, at least a factor of five is expected e.g. for the XE50 trigger. The estimates for the high P_T trigger should however be more reliable.

4.3 Detection

4.3.1 Ordinary particles

The response of the ATLAS detector is simulated by fast parameterizations using the ATLFAST package [9]. The default settings are used. That is, the acceptance is limited to $|\eta| < 2.5$, and reliable results should be expected for ordinary particles since the E_T thresholds are conservative: $\gamma > 5$ GeV, $e^{\pm} > 5$ GeV and $\mu^{\pm} > 6$ GeV. Jets are reconstructed with an R=0.4 cone after binning and smearing the fragmented generator particles according to the calorimeter performance. The jet threshold is $P_T > 15$ GeV. The μ and e reconstruction efficiency is assumed to be 100%. However, in the ATLFAST trigger simulation parameterized muon efficiencies are applied.

4.3.2 Tau particles

The tau particles are reconstructed by the hadronic decay modes using standard ATLFAST tau jet isolation criteria. The efficiency and jet rejection are parameterized using the result from a separate tau study [10] where full simulation of both calorimeter isolation and inner tracker constraints are used. The parameterization is p_T dependent. E.g. at $p_T = 15 \div 30$ GeV a 60% efficiency gives a jet rejection of 10. Here the tau efficiency is fixed to 60%. The efficiency for the reconstruction of the charge when needed is 92% taken from [11].

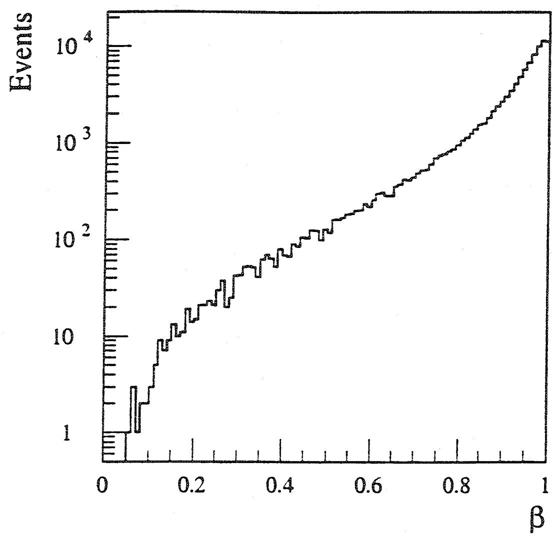

Figure 2: Velocity distribution for $\tilde{\tau}_1$.

4.3.3 Quasi-stable charged sleptons

The detection of the quasi-stable $\tilde{\tau}_1$ is parameterized using the results in [12] and is implemented into ATLFAST. Effects of the sagitta measurement, multiple scattering and energy loss fluctuations are taken into account. For a mass measurement ($m_{\tilde{\tau}_1} = p/(\beta\gamma)$) β is limited to $0.8 < \beta < 0.91$, see Figure 2. At $\beta = 0.85$ the β measurement contribution to the resolution is 10% and the momentum contribution 3%, the two terms are independent. The lower bound on β comes from the time window in the trigger chambers needed for the second coordinate and the upper bound from TOF. Thus $m_{\tilde{\tau}_1}$ can be measured down to the level of the estimated 0.1% systematic effects due to the high statistics given by 60k of $\tilde{\tau}_1$ for 10 fb^{-1}. Once $m_{\tilde{\tau}_1}$ is constrained the upper bound on β can be relaxed. 90% reconstruction efficiency is assumed within the acceptance.

5 Model G3b

In this model the $\tilde{\tau}_1$ is a quasi-stable NLSP and it decays outside of the detector. The golden event signature is a very heavy charged particle in the muon system. Virtually no standard model background is present. As described in the previous section, the $\tilde{\tau}_1$ mass is measured independently in the muon system. This enables the momentum resolution to be vastly improved by a mass constraint. Since everything in the decay chain $\chi^0_{1,2} \rightarrow l^+\tilde{l}^-_R \rightarrow l^+l^-\tilde{\tau}_1(\tau)$ is measurable except for the very soft τ, the effective mass reconstruction is almost trivial. Examples of reconstructed masses are shown in Figure 3 and 4. The $\tilde{l}_R$ mass is found from the edge in the invariant mass $M_{\tilde{\tau}_1 l}$ distribution, see the left plot in Figure 3. The $\chi^0_{1,2}$ masses can either be found directly from $M_{\tilde{l}^-_R l^+}$, or indirectly from $M_{l^+l^-}$, see right plot in Figure 4. For an introduction to effective invariant masses see appendix A. Edges are expected at

$$M_{ll}^{max} = M_{\tilde{\chi}^0_1}\sqrt{1 - \frac{M^2_{\tilde{l}_R}}{M^2_{\tilde{\chi}^0_1}}}\sqrt{1 - \frac{(M_{\tilde{\tau}_1} + M_\tau)^2}{M^2_{\tilde{l}_R}}} = 14.5 \text{ GeV } (14.3\pm0.05 \text{ GeV}), \quad (7)$$

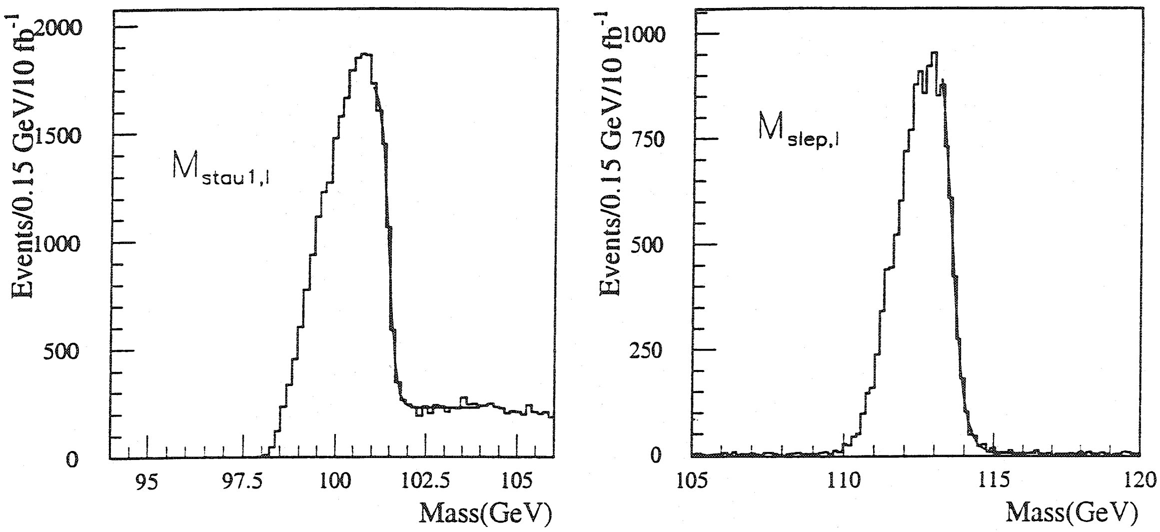

Figure 3: Minimal invariant mass distribution (left) for a stau and a lepton ($M_{\tilde{\tau}_1 l}$). The $\tilde{l}_R$ mass is extracted from the edge in the three-body decay. The fitted function is a first order polynomial times a sigmoid plus a constant background. The fit yields: $M_{\tilde{l}_R} = M_{\tilde{\tau}_1 l} + M_\tau = 103.3 \pm 0.05$ GeV. The right plot shows the spectrum of $M_{\tilde{l}^{\pm}_R l^{-}}$. Same type of fit as in the left plot is used. The result from the fit is: $M_{\tilde{\chi}^0_1} = M_{\tilde{l}_R l} + M_\tau = 115.3 \pm 0.1$ GeV.

and at

$$M_{ll}^{max} = M_{\tilde{\chi}^0_2}\sqrt{1 - \frac{M^2_{\tilde{l}_R}}{M^2_{\tilde{\chi}^0_2}}}\sqrt{1 - \frac{(M_{\tilde{\tau}_1} + M_\tau)^2}{M^2_{\tilde{l}_R}}} = 46.8 \text{ GeV } (46.7\pm0.05 \text{ GeV}). \tag{8}$$

All dilepton figures are improved by the flavor subtraction $\mu^+\mu^- + e^+e^- - \mu^\pm e^\mp$. The $\tilde{q}_{L,R}$ masses can be extracted from edges in the invariant mass spectrum M_{llj}. The dominant decay is $\tilde{q}_R \to \chi^0_1 q$, see the left plot in Figure 5. The events are selected by requiring $M_{ll} < 15$ GeV, $P_{Tll} > 65$ GeV, 2 jets with $P_T > 25$ GeV and 2 jets with $P_T > 50$ GeV. The right plot in Figure 5 also shows the spectrum M_{llj}, but with 15 GeV $< M_{ll} <$ 46 GeV. The dominant decay is $\tilde{q}_L \to \chi^0_2 q$. The expected edges are

$$M_{llj}^{max} = M_{\tilde{q}_R}\sqrt{1 - \frac{M^2_{\tilde{\chi}^0_1}}{M^2_{\tilde{q}_R}}}\sqrt{1 - \frac{(M_{\tilde{\tau}_1} + M_\tau)^2}{M^2_{\tilde{\chi}^0_1}}} = 320 \text{ GeV } (316\pm3 \text{ GeV}), \tag{9}$$

and

$$M_{llj}^{max} = M_{\tilde{q}_L}\sqrt{1 - \frac{M^2_{\tilde{\chi}^0_2}}{M^2_{\tilde{q}_L}}}\sqrt{1 - \frac{(M_{\tilde{\tau}_1} + M_\tau)^2}{M^2_{\tilde{\chi}^0_2}}} = 546 \text{ GeV } (539\pm5 \text{ GeV}). \tag{10}$$

The masses within parenthesis are from the fit. The errors are errors from the fit generously rounded upwards. The estimation is based on values taken from several fits within different regions and different sets of data. Errors from absolute energy scale calibrations are not included. Given the six mass measurements, it is easy to solve for the six masses.

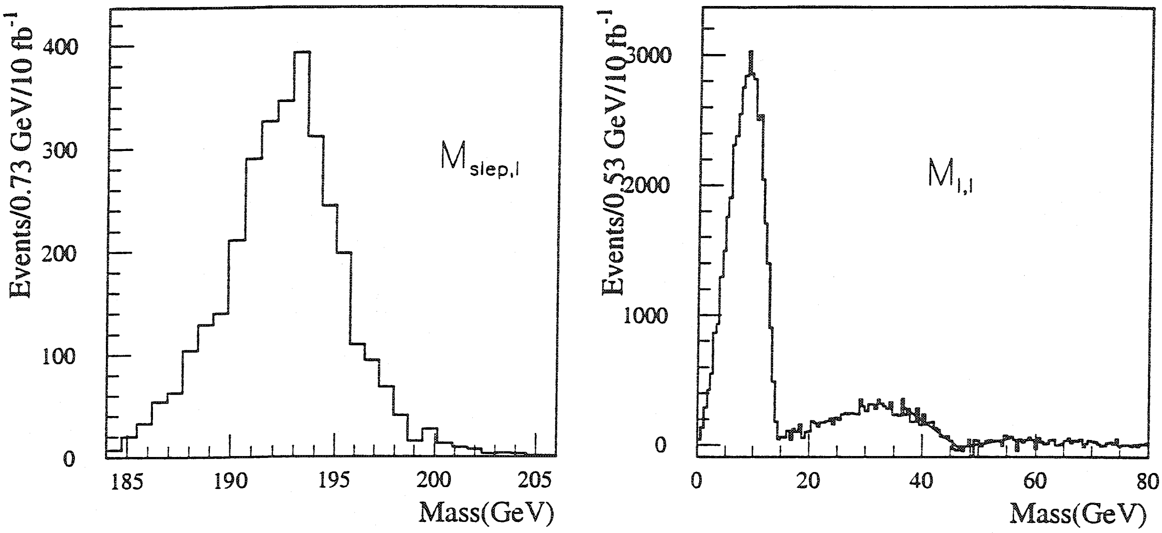

Figure 4: Minimal invariant mass (left) for a slepton and a lepton. The resolution for $M_{\tilde{\chi}_2^0}$ in the left plot is not very good. A better choice is to use the second edge in the dilepton invariant mass (M_{ll}) instead. The result from the fit is: $M_{ll} = 46.7 \pm 0.05$ GeV.

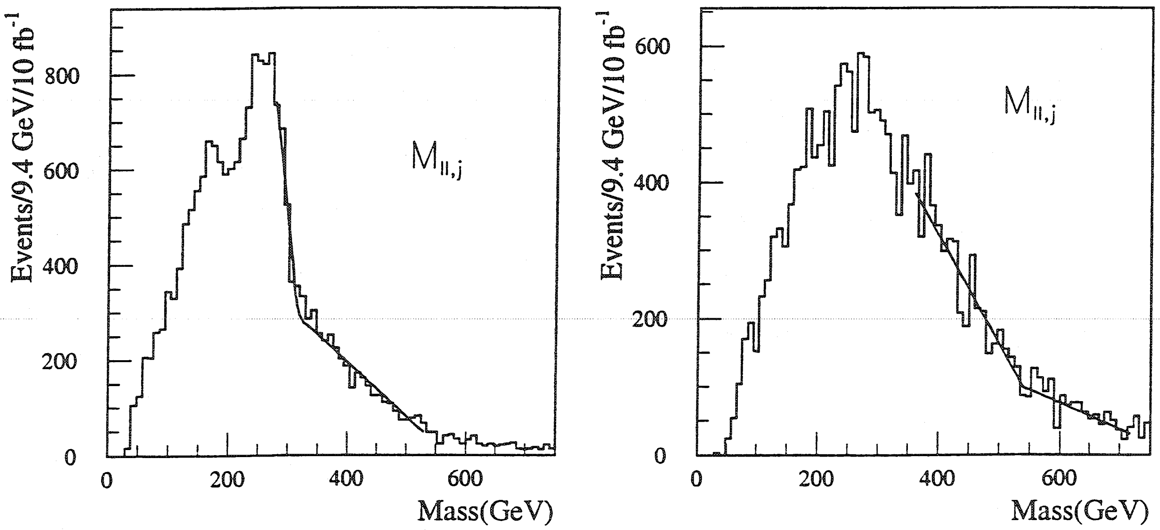

Figure 5: Invariant mass for a dilepton pair and a jet. The left plot shows M_{llj} for M_{ll} with a $P_T < 15$ GeV. The decay is dominated by $\tilde{q}_R \rightarrow \chi_1^0 q$. The right plots shows M_{llj} for M_{ll} with a $15 < P_T < 46$ GeV. This cut enhances the decay $\tilde{q}_L \rightarrow \chi_2^0 q$.

6 Model G3a

In the G3a model the NLSP is assumed to decay close to the vertex. As a result, no SUSY particle is directly detectable. However, a large amount of missing transverse energy is generated due to the LSP. In order to reject the SM background the following cuts have been applied:

- 4 jets with $P_T > 25$ GeV, jets identified as τ-jets are not included.
- At least one pair of same flavor opposite signed leptons.
- $M_{eff} > 300$ GeV.
- $E_{T_{miss}}/M_{eff} > 0.1$.

At the end of the decay chain we find a very hard tau. The most efficient reconstruction of the tau turns out to be via the hadronic decay modes. Hence only taus decaying into hadrons are used.

The decay chain is the same as in G3b, but with the difference that the $\tilde{\tau}_1$ now decays into $\tilde{\tau}_1 \to \tilde{G}\tau$. The complete investigated decay chain looks like $\tilde{q}_R \to \tilde{\chi}^0_{1,2} q \to \tilde{l}^-_R l^+ q \to \tilde{\tau}_1(\tau) l^- l^+ q \to \tilde{G}\tau(\tau) l^- l^+ q$. The (τ) is not detectable in the calorimeter due to the limited available phase-space. The lepton from the $\tilde{l}_R$-decay is very soft but detectable. The average P_T is 10 GeV, and a cut is made above 15 Gev to select these leptons. The p_T of the tau is required to be larger than 75 GeV. The invariant mass $M_{\tau l}$ is shown in Figure 6. Edges are expected at

$$M_{\tau l}^{max} = \sqrt{M_{\tilde{l}_R}^2 - (M_{\tilde{\tau}_1} + M_\tau)^2} = 29.0 \text{ GeV } (28.4\pm1 \text{ GeV}). \tag{11}$$

and

$$M_{\tau l}^{max} = \sqrt{M_{\tilde{\chi}_1^0}^2 - M_{\tilde{l}_R}^2} = 51.7 \text{ GeV } (44\pm5 \text{ GeV}). \tag{12}$$

The first edge in the plots in Figure 6 is not very much affected by the SM background. However, the second edge is more sensitive. Since the statistics is too low, e.g. a factor 10 for $t\bar{t}$, the fluctuations are too large to represent the real background. Real statistics should improve the situation in the left plot. In the right plot the background is more complicated. The background under the signal looks similar to the signal and causes a systematic shift of the edge. Special cuts to reduce the $t\bar{t}$ background may improve the situation. The background in the jet plots is almost negligible. The edges for M_{ll} and M_{llj} are the same as in G3b. The results from the fits are

$$M_{ll}^{max} = 14.5 \text{ GeV } (14.3\pm0.1 \text{ GeV}),$$

$$M_{ll}^{max} = 46.8 \text{ GeV } (57\pm1 \text{ GeV}),$$

and

$$M_{llj}^{max} = 320 \text{ GeV } (313\pm6 \text{ GeV}),$$

$$M_{llj}^{max} = 546 \text{ GeV } (530\pm5 \text{ GeV}),$$

The measured endpoint is systematically lower in many cases. This is expected to some extent since taus and jets leak out of the cone. The tau also has an unmeasured neutrino.

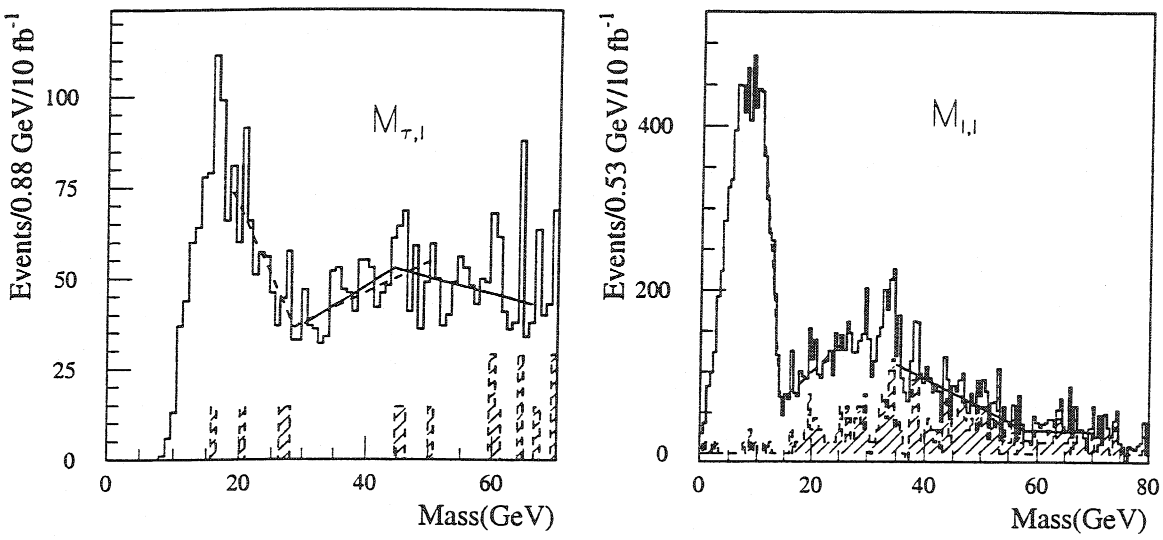

Figure 6: The invariant mass for a hard tau and a very soft lepton (left). The fluctuations of the background is large since the statistics does not represent the real expected background. The right plot shows the distribution of M_{ll}. The second edge is systematically shifted due to the shape of the background.

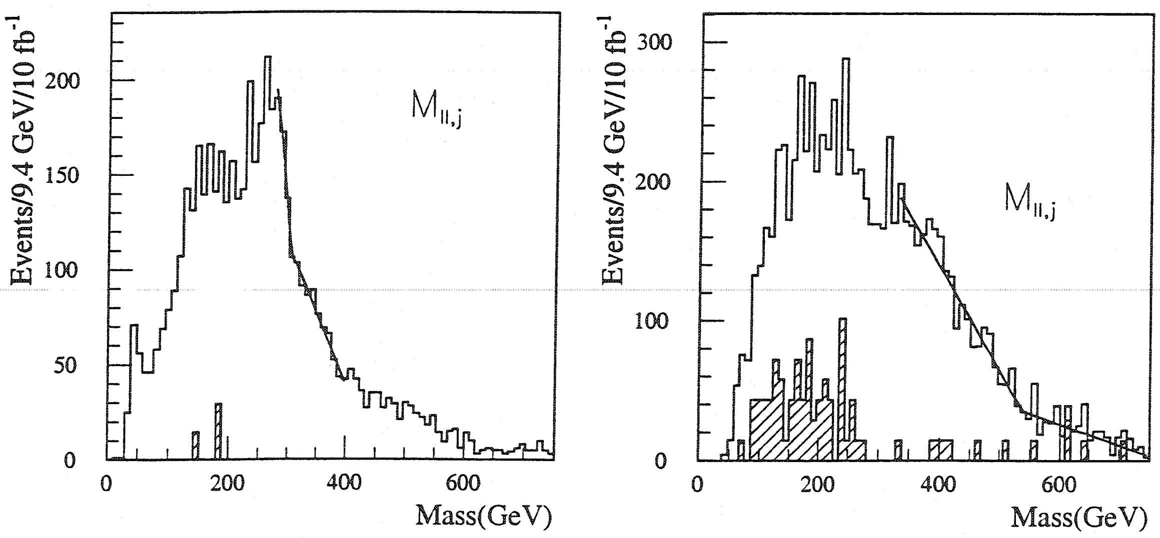

Figure 7: The same M_{llj} distributions as in G3b, but for G3a and with SM background included. The background is negligible under the fitted region.

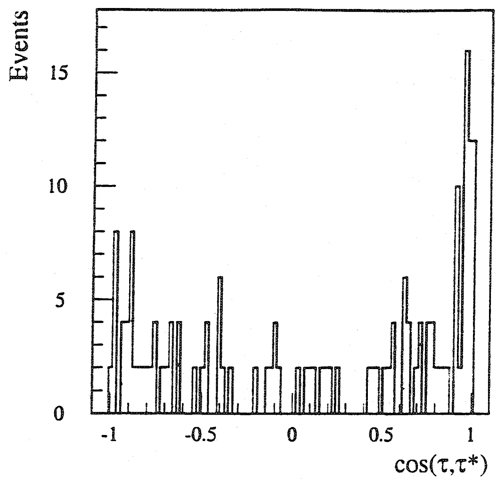

Figure 8: The plot shows $\cos\theta$ for the opening angle θ between the true tau momentum vector $\vec{\tau}$ and the tau momentum vector $\vec{\tau}^*$ estimated from a mass constrained decay chain.

7 Proof of the NSLP flavor

In the G3b model one cannot prove the flavor of the NLSP unless the soft tau is found. Since the P_T is so low it cannot be detected in the calorimeter. However, apart from the soft tau everything else is measureble. Thus, after measuring three masses, the tau momentum can be solved by imposing the mass constraints, see appendix B for details.

Three masses and four 4-vectors are needed. These are taken from the well measured decay: $\tilde{l}_L \to \chi_1^0 l \to \tilde{l}_R^- l^+ l \to \tilde{\tau}_1(\tau) l^- l^+ l$. The opening angle between the true $\vec{\tau}$ vector and the mass constrained estimation $\vec{\tau}^*$ is shown in Figure 8. Perfect masses are assumed. The vector $\vec{\tau}$ could e.g. be replaced with tau vertex candidates from the inner tracker and a correlation of the type seen in Figure 8 would constitute a definite proof of the NLSP flavor.

8 Conclusions

The signals from GMSB models with $\tilde{\tau}_1$ as the NLSP have been investigated. Both the case with a quasi-stable NSLP (G3b), and the case with a NLSP decaying close to the vertex (G3b). The G3b model can be fully reconstructed with good mass resolution similar to related models studied previously [2]. The G3a model is harder than G3b from an experimental point of view due to the fact that the decay chain reconstruction is based on tau leptons in the final state. However, also in this case can masses of sleptons, neutralinos and squarks be determined with surprising precision, and nothing prevents a reasonable estimation of the model parameters from the measured masses.

Acknowledgements

I want to thank Ian Hinchliffe and Frank Paige for proposing this study. Frank helped me several times with ISAJET. Ian has been very helpful with ideas and answering questions, especially during my stay at Berkeley Labs. Giacomo Polesello provided a lot of the information on the quasi-stable stau resolution, and also guided me during the initial phase of the background simulations.

A Effective mass kinematics in decay chains

One of the basic tools in SUSY measurements are edges in the effective mass spectrum. These masses can be formed from squares of arbitrary 4-vectors at different stages in the decay chain. As an illustration I here derive the simplest possible non trivial maximal effective mass, i.e.:

$$\max m_{BD}^2 = (p_B + p_D)^2 \tag{13}$$

in the decay:

$$A \to B + C, C \to D + E \tag{14}$$

The derivation is general, but since it is used in the dilepton effective mass analysis, the leptons (B and D) are assumed to be massless. The equality sign indicates when this approximation is made. The first step is to find the momentum in the CM of the decaying particle:

$$(E_B, \vec{\mathbf{p}}_\mathbf{B}) \leftarrow \quad A \quad \to (E_C, -\vec{\mathbf{p}}_\mathbf{B}) \tag{15}$$

$$(E'_D, \vec{\mathbf{p}}'_\mathbf{D}) \leftarrow \quad C' \quad \to (E'_E, -\vec{\mathbf{p}}'_\mathbf{D}) \tag{16}$$

After expanding Equation (13) and solving for $\vec{p}^2$ one finds

$$p \simeq \frac{m_A^2 - m_C^2}{2m_A}. \tag{17}$$

Thus

$$E_B \simeq \frac{m_A^2 - m_C^2}{2m_A}, \tag{18}$$

$$E_C \simeq \frac{m_A^2 + m_C^2}{2m_A}. \tag{19}$$

The boost between the frames is then simply

$$\beta = \frac{m_A^2 - m_C^2}{m_A^2 + m_C^2}, \tag{20}$$

$$\gamma = \frac{m_A^2 - m_C^2}{2m_A m_C}. \tag{21}$$

By boosting to the unprimed system one finds

$$E_D = \gamma E'_D + \gamma\beta E'_D = \frac{m_C^2 - m_E^2}{2m_C^2} m_A \tag{22}$$

The effective mass is now

$$m_{BD}^2 = 4E_B E_D = m_A^2 (1 - \frac{m_C^2}{m_A^2})(1 - \frac{m_E^2}{m_C^2}) \tag{23}$$

The same technique can be used to construct more complex effective masses.

B Mass constraints

Given three masses in a decay chain it is possible to reconstruct the momentum of one of the decay products. This solution is due to [2] but is given here explicitly for the generic case. The reconstructed momentum is solved for $\vec{p}_1$. The equation system is:

$$\begin{aligned} (p_0+p_1+p_2)^2 &= M_1^2 && (24)\\ (p_0+p_1+p_2+p_3)^2 &= M_2^2 && (25)\\ (p_0+p_1+p_2+p_3+p_4)^2 &= M_3^2 && (26) \end{aligned}$$

Expand the squared 4-vectors and collect $\vec{p}_1$ on the left hand side by subtracting the equations ($E_a \equiv E_0 + E_2$, $\vec{p}_a \equiv \vec{p}_0 + \vec{p}_2$):

$$\begin{aligned} 2E_1E_a - 2\vec{p}_1\cdot\vec{p}_a &= M_1^2 - m_0^2 - m_1^2 - m_2^2 - 2E_0E_2 + 2\vec{p}_0\cdot\vec{p}_2 = C_1 && (27)\\ 2E_1E_3 - 2\vec{p}_1\cdot\vec{p}_3 &= M_2^2 - M_1^2 - m_3^2 - 2E_0E_3 - 2E_2E_3 + \\ &\quad 2\vec{p}_0\cdot\vec{p}_3 + 2\vec{p}_2\cdot\vec{p}_3 = C_2 && (28)\\ 2E_1E_4 - 2\vec{p}_1\cdot\vec{p}_4 &= M_3^2 - M_2^2 - m_4^2 - 2E_0E_4 - 2E_2E_4 - 2E_3E_4 + \\ &\quad 2\vec{p}_0\cdot\vec{p}_4 + 2\vec{p}_2\cdot\vec{p}_4 + 2\vec{p}_3\cdot\vec{p}_4 = C_3 && (29) \end{aligned}$$

We want $\vec{p}_1$ alone on the left hand side. $E_1(|\vec{p}_1|)$ is eliminated by subtraction:

$$\begin{aligned} (27)\cdot E_3 - (28)\cdot E_a \Rightarrow (2\vec{p}_3E_a - 2\vec{p}_aE_3)\cdot\vec{p}_1 = E_3C_1 - E_aC_2 \Rightarrow \vec{D}_1\cdot\vec{p}_1 = F_1 && (30)\\ (28)\cdot E_4 - (29)\cdot E_3 \Rightarrow (2\vec{p}_4E_3 - 2\vec{p}_3E_4)\cdot\vec{p}_1 = E_4C_2 - E_3C_3 \Rightarrow \vec{D}_2\cdot\vec{p}_1 = F_2 && (31) \end{aligned}$$

Given two linear equations we can now find a solution for e.g. p_{1x} and p_{1y}

$$\begin{matrix} D_{1x}p_{1x} + D_{1y}p_{1y} + D_{1z}p_{1z} = F_1 \\ D_{2x}p_{1x} + D_{2y}p_{1y} + D_{2z}p_{1z} = F_2 \end{matrix} \Rightarrow \qquad (32)$$

$$\begin{pmatrix} D_{1x} & D_{1y} \\ D_{2x} & D_{2y} \end{pmatrix}\begin{pmatrix} p_{1x} \\ p_{1y} \end{pmatrix} = \begin{pmatrix} F_1 & -D_{1z} \\ F_2 & -D_{2z} \end{pmatrix}\begin{pmatrix} 1 \\ p_{1z} \end{pmatrix} \Rightarrow \qquad (33)$$

$$\begin{pmatrix} p_{1x} \\ p_{1y} \end{pmatrix} = \frac{1}{D_{1x}D_{2y} - D_{1y}D_{2x}}\begin{pmatrix} D_{2y} & -D_{1y} \\ -D_{2x} & D_{1x} \end{pmatrix}\begin{pmatrix} F_1 & -D_{1z} \\ F_2 & -D_{2z} \end{pmatrix}\begin{pmatrix} 1 \\ p_{1z} \end{pmatrix} \Rightarrow \qquad (34)$$

$$\left\{ \mathbf{A} = \frac{1}{D_{1x}D_{2y} - D_{1y}D_{2x}}\begin{pmatrix} D_{2y}F_1 - D_{1y}F_2 & -D_{2y}D_{1z} + D_{1y}D_{2z} \\ -D_{2x}F_1 + D_{1x}F_2 & D_{2x}D_{1z} - D_{1x}D_{2z} \end{pmatrix} \right\} \qquad (35)$$

$$\begin{matrix} p_{1x} = A_{11} + A_{12}p_{1z} \\ p_{1y} = A_{21} + A_{22}p_{1z} \end{matrix} \qquad (36)$$

This solution is then plugged into equation (27) and squared to avoid the square root in the expression for the energy

$$\begin{aligned} 2E_1E_a &= C_1 + 2\vec{p}_1\cdot\vec{p}_a \Rightarrow && (37)\\ E_1^2E_a^2 &= C_1^2/4 + (\vec{p}_1\cdot\vec{p}_a)^2 + C_1\vec{p}_1\cdot\vec{p}_a && (38)\\ (p_{1x}^2 + p_{1y}^2 + p_{1z}^2 + m_1^2)E_a^2 &= C_1^2/4 + (p_{1x}p_{ax} + p_{1y}p_{ay} + p_{1z}p_{az})^2 + \\ &\quad C_1(p_{1x}p_{ax} + p_{1y}p_{ay} + p_{1z}p_{az}) && (39) \end{aligned}$$

Once the solution for p_{1x} and p_{1y} is plugged in it gets kind of messy, but it is just an ordinary quadratic equation in p_{1z}.

$$\begin{aligned}
-(A_{11}^2 + A_{12}^2 p_{1z}^2 + 2A_{11}A_{12}p_{1z} + A_{21}^2 + A_{22}^2 p_{1z}^2 + 2A_{21}A_{22}p_{1z} + p_{1z}^2 + m_1^2)E_a^2 + \\
C_1^2/4 + (A_{11}^2 + A_{12}^2 p_{1z}^2 + 2A_{11}A_{12}p_{1z})p_{ax}^2 + (A_{21}^2 + A_{22}^2 p_{1z}^2 + 2A_{21}A_{22}p_{1z})p_{ay}^2 + \\
p_{1z}^2 p_{az}^2 + 2(A_{11}A_{21} + A_{11}A_{22}p_{1z} + A_{12}A_{21}p_{1z} + A_{12}A_{22}p_{1z}^2)p_{ax}p_{ay} + \\
2(A_{11} + A_{12}p_{1z})p_{ax}p_{1z}p_{az} + 2(A_{21} + A_{22}p_{1z})p_{ay}p_{1z}p_{az} + \\
C_1\left[(A_{11} + A_{12}p_{1z})p_{ax} + (A_{21} + A_{22}p_{1z})p_{ay} + p_{1z}p_{az}\right] \\
= 0 \qquad (40)
\end{aligned}$$

After coefficient identification the final solution reads

$$p_{1z} = \frac{-B_1 \pm \sqrt{B_1^2 - 4B_0B_2}}{2B_2} \qquad (41)$$

where

$$\begin{aligned}
B_0 &= (-A_{11}^2 - A_{21}^2 - m_1^2)E_a^2 + C_1^2/4 + A_{11}^2 p_{ax}^2 + A_{21}^2 p_{ay}^2 + \\
&\quad 2A_{11}A_{21}p_{ax}p_{ay} + C_1 A_{11}p_{ax} + A_{21}p_{ay} \qquad (42)\\
B_1 &= 2(-A_{11}A_{12} - A_{21}A_{22})E_a^2 + 2A_{11}A_{12}p_{ax}^2 + \\
&\quad 2A_{21}A_{22}p_{ay}^2 + 2p_{ax}p_{ay}(A_{11}A_{22} + A_{12}A_{21}) + \\
&\quad 2A_{11}p_{ax}p_{az} + 2A_{21}p_{ay}p_{az} + C_1(A_{12}p_{ax} + A_{22}p_{ay} + p_{az}) \qquad (43)\\
B_2 &= (-A_{12}^2 - A_{22}^2 - 1)E_a^2 + A_{12}^2 p_{ax}^2 + A_{22}^2 p_{ay}^2 + \\
&\quad p_{az}^2 + 2A_{12}A_{22}p_{ax}p_{ay} + 2A_{12}p_{ax}p_{az} + 2A_{22}p_{ay}p_{az} \qquad (44)
\end{aligned}$$

References

[1] G.F. Giudice, R. Rattazzi, Theories with Gauge-Mediated Supersymmetry Breaking, hep-ph/9801271.

[2] I. Hinchliffe and F. Paige, Measurements in Gauge Mediated SUSY Breaking Models at LHC, ATL-PHYS-98-134 (1998).

[3] S. Ambrosanio, G. Blair, Precision GMSB at a Linear Collider, hep-ph/9907396.

[4] F. Paige, S. Protopopescu, ISAJET 7.44 A Monte Carlo Generator for pp, $\bar{p}p$ and e^+e^- Reactions. http://penguin.phy.bnl.gov/~paige/

[5] M. Krämer, Supersymmetric particle production at hadron colliders, hep-ph/9809259.

[6] W. Beenakker et. al., The production of charginos/neutralinos and sleptons at hadron colliders, hep-ph/9906298.

[7] T. Sjöstrand, PYTHIA 5.7 and JETSET 7.4, Computer Physics Common. **82**, 1994. Program version 6.136.

[8] R. Bonciani et al, NLL Resummation of the Heavy-Quark Hadroproduction Cross-Section, hep-ph/9801375.

[9] E. Richter-Was, D. Froidevaux, L. Poggioli, A Fast Simulation Package for ATLAS, ATL-COM-PHYS-98-011 (1998).

[10] D.Cavalli and S.Resconi, Tau-jet separation in ATLAS detector, ATL-PHYS-98-118.

[11] Y. Coadou et al, Identification of Hadronic Tau decays in ATLAS, ATL-PHYS-98-126.

[12] G. Polesello, A. Rimoldi, Reconstruction of quasi-stable charged sleptons in the ATLAS Muon Spectrometer, ATL-MUON-99-006 (1999).